Durham E-Theses

Investigating the Molecular basis of Cole Carpenter Syndrome

CLEWS, CHARLOTTE,ELIZABETH,CATHE

How to cite:

CLEWS, CHARLOTTE,ELIZABETH,CATHE (2022) *Investigating the Molecular basis of Cole Carpenter Syndrome*, Durham theses, Durham University. Available at Durham E-Theses Online: http://etheses.dur.ac.uk/14494/

INVESTIGATING THE MOLECULAR BASIS OF COLE CARPENTER SYNDROME

CHARLOTTE ELIZABETH CLEWS

This thesis is submitted as part of the requirements for the award of
Degree of Master of Research

School of Biosciences
Durham University
2021

Table of Contents

Abstract

Cole Carpenter syndrome (CCS) is a rare genetic syndrome affecting bone integrity and durability. It is believed to be related to osteogenesis imperfecta (OI), a group of genetic disorders commonly known as brittle bone disease. The molecular mechanism of the syndrome has yet to be discovered, however two distinct types have been identified: CCS1 and CCS2, linked to mutations in protein disulphide isomerase (PDI), and SEC24D (a component of the COPII vesicle export complex) respectively. This thesis will provide groundwork in investigating the molecular basis of CCS1. This variant is characterised by a single amino acid substitution mutation (Y393C) in PDI, an endoplasmic reticulum (ER) specific protein disulphide isomerase and molecular chaperone involved in collagen folding. Without this chaperone, collagen cannot fold into its triple helical tertiary structure, and this misfolded protein may accumulate in the ER, activating the unfolded protein response (UPR). It has been suggested that a failure to resolve this response may result in the brittle bone phenotype of Cole Carpenter syndrome. This thesis presents work in both primary cells and established cell lines to identify potential interacting partners of Y393C-PDI, hypothesising the potential downstream effects on collagen matrix production. Indirect immunofluorescent labelling of collagen I suggests that collagen production is impaired, and confocal microscopy revealed abnormal ER and lysosome organelle morphologies in Y393C-PDI expressing cells. Overall cell viability of affected cells appears significantly decreased, and they are less influenced by the action of small molecule inhibitors than wild-type cells. Altogether, these preliminary data shed light on the cause of the bone specific phenotype of Cole Carpenter Syndrome 1, and potentially help to understand other OI-related disorders.

Statement of Originality

I hereby certify that, to the best of my knowledge and belief, the intellectual content of this thesis is the product of the named author. The work presented was conducted in the Department of Biosciences at Durham University between September 2019 and March 2021. This thesis does not infringe upon copyright or proprietary rights and no material has been previously published or written, except where references are made. This thesis has not previously been submitted to any other university or institution for a higher qualification.

Statement of Copyright

The copyright of this thesis rests with the author. No quotation from it should be published without prior consent from the author, and information derived from it should be acknowledged.

Notes for thesis

All diagrams and schematics presented in this thesis were devised and generated by the named author, unless stated as reproduced from the relevant literature (Figure 1.2).

List of Figures

List of Tables

List of Abbreviations

APS	Ammonium persulfate
ATCC	American Type Culture Collection
ATCC	American Type Culture Collection
ATF6	Activating Transcription Factor 6
BSA	Bovine Serum Albumin
CCS(1)	Cole Carpenter syndrome 1
CL2	Category Level 2
DMEM	Dulbecco's Modified Eagle Medium
DMSO	Dimethyl sulfoxide
DTT	Dithiothreitol
ECM	Extra-cellular matrix
EGTA	(ethylene glycol-bis(β-aminoethyl ether)-N,N,N',N'-tetraacetic acid
ER	Endoplasmic reticulum
ERAD	Endoplasmic Reticulum Associated Protein Degradation
ERO1 α	ER oxidoreductin 1
FDR	False Discovery Rate
FIJI	Fiji Is Just ImageJ
HRP	Horseradish peroxidase
HSC	Heat shock cognate
HSP	Heat Shock Protein
LC-MS/MS	Liquid Chromatography Mass Spectrometry
MES	2-ethanesulfonic acid
NT	Non-transfected
OI	Osteogenesis imperfecta

P4H(A)(B)	Prolyl-4-hydroxylase complex (subunits A and B)
PAO	Phenylarsine oxide
PBS	Phosphate Buffered Saline
PDI	Protein Disulphide Isomerase
PERK	Protein Kinase-like ER kinase
PFA	Paraformaldehyde
PIPES	Piperazine-N,N'-bis(2-ethanesulfonic acid)
POI	Protein of Interest
PVDF	Polyvinylidene fluoride
FBS	Foetal Bovine Serum
qPCR	Quantitative Polymerase Chain Reaction
RB-11-ca	1,3,5-triazine
rER	Rough endoplasmic reticulum
RPMI	Roswell Park Memorial Institute
SDS	Sodium dodecyl sulphate
SMI	Small molecule inhibitor
TBS	Tris buffered saline
TBS-T	Tris buffered saline with Tween
TEMED	Tetramethylethylenediamine
WT	Wild-type
Xbp-1	Spliced X-box protein 1

List of Units

Å	Angstrom
˚C	degrees Celsius
g	gram
g	Gravitational force equivalent
kb	kilobases
kDa	kilodaltons
L	litre
µg	microgram
µL	microlitre
µM	micromole
mA	milliamps
mg	milligram
ml	millilitre
mM	millimole
M	molar
g/mol	molar mass
ng	nanogram
nm	nanometre
%	percent
V	volts
v/v	Volume for volume
w/v	Weight for volume

Acknowledgements

This thesis would not have been possible without the help and support of many people at Durham University and beyond. Firstly, I would like to thank my supervisor, Dr Adam Benham for his enthusiasm, knowledge and patience as I learned to navigate the unfamiliar waters of academia. I must also thank all of Laboratory 8 and 4 for their humour and friendship, and the rest of Benham lab for their eclectic use of group-chats. Also thanks to Dr Meena Balasubramanian for her knowledge and helpful discussions, providing valuable insights from a clinical aspect. All the above have made my master's research exciting, fulfilling and inspiring, and a fantastic first stage of my academic career.

I'd like to thank my wonderful family for their patience when I get excited about science (all the time) and for listening, despite having very little idea of what I'm talking about. It is through them I acquired my passion for accessible and unbiased scientific communication for all, regardless of education or background.

Lastly, I must thank those who contributed to my time in Durham outside of my research: to all those who smile and chat in the corridors, thank you. And to all those in DUCB, good luck, and thank you for making my Sunday(s).

xx

1 INTRODUCTION

1.1 Osteogenesis imperfecta and Cole Carpenter Syndrome

Bone is one of the most important physiological structures in the body, with integral roles in structural support and movement, organ protection and immune cell production (Weiner, 1998). It also is vital for the maintenance of Calcium (Ca^{2+}) and phosphate (PO^{3-}) in the body through the process of continuous production and resorption (Weiner, 1999). The composition of bone broadly consists of the following: inorganic materials which make up 65-70%, such as hydroxyapatite ensuring hardness and durability; organic mass (20-25%) which predominantly consists of collagen type I, providing the intrinsic elasticity necessary for movement. The remaining 10% consists of water associated with collagen. This is predominantly collagen type I, although type III and VI are known to associate to bone, the latter seemingly less prevalent in adult tissue (Hall, 2011; Keene, 1991).

Despite the inherent resilience and structural importance of bone integrity, around 500,000 fragility-related bone fractures occur every year in the UK alone (Richetta, 2019), due to both age-related diseases, and the impact of genetically derived disorders such as Osteogenesis Imperfecta (OI), also known as brittle bone syndrome.
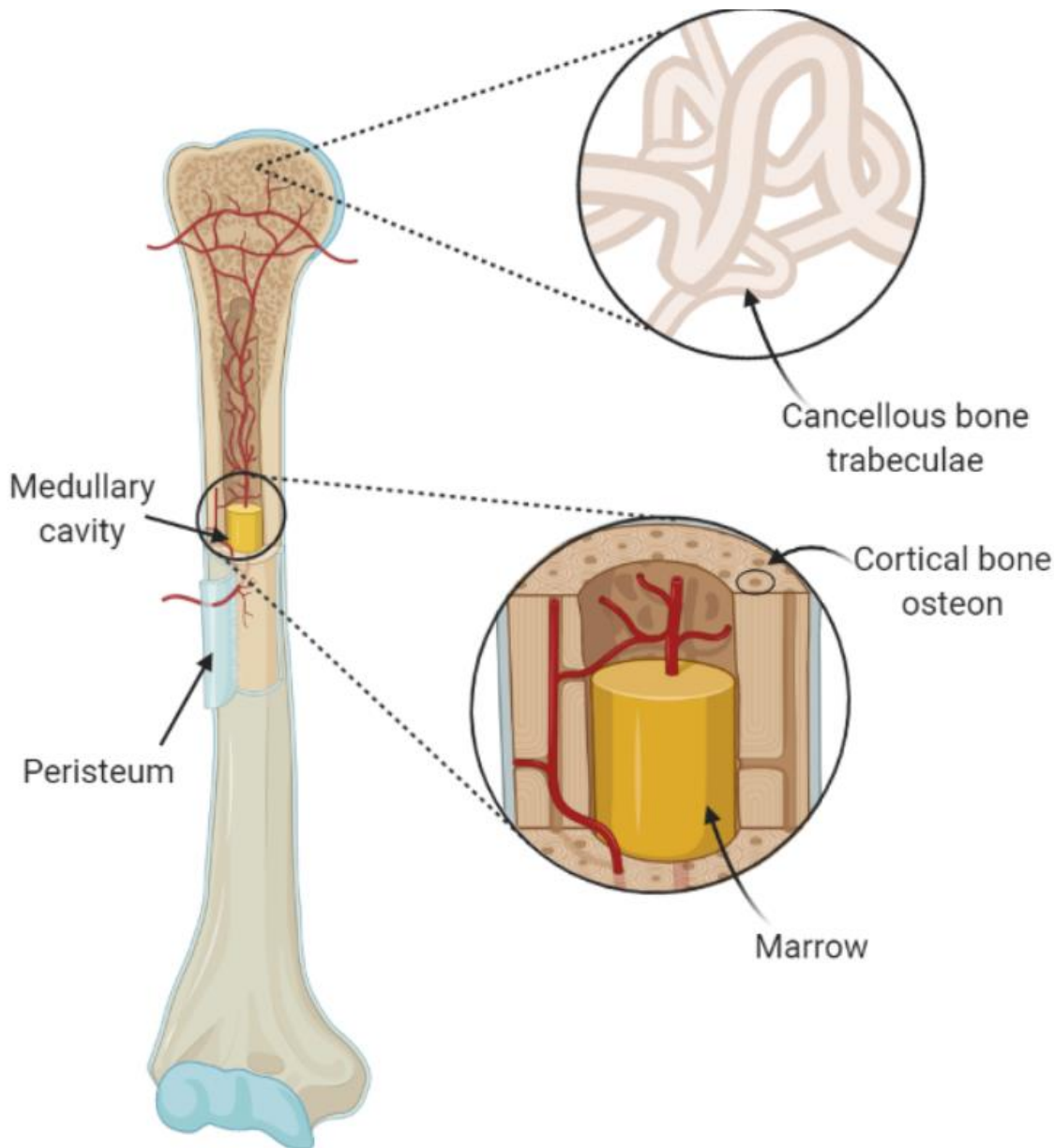
Figure 1.1. The inner ultrastructure of bone tissue. The inner cortical (compact) bone lies closest to the medullary cavity. The surrounding cancellous (spongy) bone is covered by the protective periosteum.

OI results from a disproportionately large amount of 'spongy bone' also known as cancellous or trabecular bone versus 'compact bone', or cortical bone, as shown in Figure 1.1. Cancellous bone is softer than cortical bone and is made up of 'trabeculae', a network of interlocking tubular structures containing bone cells and vasculature, as opposed to the parallel, tightly packed osteons of cortical bone. Cancellous bone surrounds the medullary cavity where yellow and red bone marrow is stored, the former essential for fat and cartilage production, and the latter producing red blood cells (Gurevich, 2007). Cancellous bone also dominates the joint-proximal extremities of the bone and, like cortical bone, is lost with age, leading to a general decrease in bone density (Parkinson, 2013).

Table 1.1. Characterisation of cell types found in cortical and cancellous bone tissue.

Bone cell	Role
Osteoblast	Responsible for the production and secretion of osteoid, the collagen I-based matrix, and non-collagenous osteonectin and osteocalcin to reform bone (Casella, 1994).
Osteocyte	Inactive osteoblasts responsible for cell-cell communication. Located in the lacunae between lamellae within the compact bone osteon.
Osteoclast	Large cells with up to 50 nuclei. Responsible for lysosomal-mediated breakdown of old bone by the process of resorption.
Osteoprogenitors	Mesenchymal stem cells which differentiate into osteoblasts, and are important in fracture repair (Long, 1995).

Compact bone accounts for approximately 80% of skeletal density and ensures rigidity and skeletal support. It comprises the outer layer of long bones and is made up of many repeating functional units known as osteons, labelled in Figure 1.1, which contain multiple types of bone cells (Rho, 1999). Each osteon is clustered amongst others, containing a central blood vessel canal known as a Haversian canal. This is surrounded by layers of compact matrix called lamellae and regions of cell-cell junctions called lacunae (Marotti, 1979). Each cell type outlined in Table 1.1. is integral to the continued remodelling of bone and the relevant proportions of cortical and cancellous tissue, and therefore overall bone density (Sims, 2014). Osteonectin, osteocalcin and non-collagenous ECM are mostly synthesised by metabolically active osteoblasts and are necessary for the continuous remodelling of bone (Ozdemir, 2016). Osteonectin represents the most abundant non-collagenous protein in mineralized bone matrix and is also referred to as the

3

secreted protein acidic and rich in cysteine (SPARC) or basement membrane protein 40 (BM-40) (Heinegård, 1989).

If the process of bone resorption by osteoclasts exceeds formation by osteoblasts, the bones become brittle and prone to mis-formation and multiple fractures (Ciarallo, 2006). It is hypothesised that slight differences in collagen production and trafficking may cause a cascade of events impacting the production or distribution of osteoid, resulting in significant changes to bone density. Owing to the important role of the collagen matrix in signalling between cells, this imbalance could therefore contribute to an OI phenotype.

Cole Carpenter syndrome (CCS) is an extremely rare form of OI, and one of the most severe, mostly affecting children a few months from birth. Patients with Cole Carpenter syndrome type 1 have a mutated version of the gene P4HB, which encodes Protein Disulphide Isomerase (PDI), an ER-localised oxidoreductase and molecular chaperone implicated in proper collagen folding (Rauch, 2015). Current research suggests the phenotypes associated with CCS1 arise through defects in collagen folding or trafficking in the osteoid producing osteoblasts.

1.1.1 Molecular chaperones are essential in maintaining cellular homeostasis

The maintenance of proper cellular function relies on the vast array of proteins that are constantly produced. The information required to ensure proper folding of primary protein structures into secondary, tertiary and potentially quaternary structures is mostly intrinsic, allowing the structure to 'collapse' into a thermodynamically stable state (Linquist, 2011). However, this process is not error-free, therefore an additional level of control is often needed, catalysed by the actions of molecular chaperones (Frydman, 2001). These proteins actively ensure the proper folding into higher order structures of complex proteins inside the cell, such as collagen I.

An endoplasmic reticulum (ER) chaperone, Protein Disulphide Isomerase, is a key protein enabling procollagen chains to fold properly into the characteristic triple helical form which is then secreted from the cell. In studied CCS1 patients, it is currently accepted that PDI has a heterozygous missense mutation at nucleotide 1178 from an adenine to guanine (A>G), resulting in a Tyr393Cys substitution in the protein (Rauch, 2015). This gain of cysteine mutation has been implicated in

4

incorrect collagen processing and transport in these cells, which may contribute to a reduction in osteoid formation and produce the brittle bone phenotype.

Collagen production and secretion by CCS patient fibroblasts has been reported to be normal, suggesting the quality - not quantity - of protein is affected (Cole and Carpenter, 1987). Rather than causing a 'loss of function', which would result in no collagen production or secretion, a 'gain of dysfunction' hypothesis has been proposed to explain the effects of this mutation, resulting in misfolded collagen aggregating in the ER (Balasubramanian, 2018). This is suggested to increase the demand for protein folding in the ER, exceeding the organelle's capacity to achieve this, eliciting ER stress. Alongside disrupting the delicate environment of the ER, aggregation of unfolded or misfolded protein activates the ER stress response pathways as seen in many other genetic conditions such as neurodegenerative syndromes (Winklhofer, 2008). This collection of cellular stress responses results in either: degradation of the misfolded protein by activated proteases; an increase in chaperone production to 'rescue' misfolded collagen; or apoptosis (Hetz, 2018). It has been suggested that failure to resolve ER stress responses in bone cells results in the brittle bone characteristic of Cole Carpenter syndrome.

1.1.2 *Historical diagnoses*

In 1987, Cole and Carpenter described a new, autosomal recessive form of OI, characterised by bone fragility and deformity, growth failure and distinctive facial features such as eyeball bulging (ocular proptosis) and an asymmetrical skull due to early suture closure (craniosynostosis). Their two unrelated patients developed fractures and growth deformities shortly after birth, however brain function and intellect were reported as normal, as was the quantity of collagen production (Cole and Carpenter, 1987).

Further cases of CCS1 have since been reported (Ouyang, 2017), (Balasubramanian, 2018), alongside (Amor, 2000), (Marwaha, 1993), (Stopfer, 1992), (MacDermot, 1995), however the latter three diagnoses report significantly varied phenotypes from the original, such as finger webbing and microcephaly suggesting they may not be genetically the same disorder. After further analysis of MacDermot's 1995 report, it has been suggested the correct diagnosis is Coffin-Lowry syndrome (Fryns, 1996), which causes many visual and cognitive defects, alongside impaired growth.

Similar conditions such as Bruck syndrome, another autosomal recessive disorder in which collagen crosslinks due to a deficiency of hydroxylation (MacPherson and Clemens, 1997), also results in fragile bones, fractures, and other skeletal deformities, and can be mistaken for CCS1. Due to these phenotypic similarities with other rare syndromes, it can be difficult to discern one case of true CCS1 from other closely related conditions.

1.1.3 Characterisation of Cole Carpenter syndrome

Currently there are two characterised types of Cole Carpenter syndrome, both linked to separate mutations involved in collagen packaging and transportation. This project will focus on CCS type 1, and the P4HB gene mutation linked to its cause. P4HB is the coding DNA for the beta subunit of the prolyl 4-hydroxylase complex (P4H), also known as PDI. The single nucleotide polymorphism results in the large amino acid tyrosine at position 393 to be substituted for a smaller, reactive cysteine. It is suggested that the usual hydroxylation of collagen I proline is impacted by this mutation, leading to the CCS1 phenotype shown in Figure 1.2. (Rauch, 2015).

Through collaboration with our clinical partner at Sheffield Children's hospital, we have been able to gain an insight into a CCS1 patient presenting the phenotypes associated with the original two cases of Cole and Carpenter. The individual had a normal birth, however soon presented with impaired growth and an extreme susceptibility to fractures, resulting in an OI diagnosis. Exome sequencing confirmed the patient carried the Y393C-PDI mutation (Balasubramanian, 2018).

The current prevailing method of treating bone degenerative syndromes is with bisphosphonates (Khosla, 2012). These block the resorption of bone, favouring the production of new osteons and thus restoring the balance between bone resorption and formation (Fleisch, 2002). They can be taken orally or administered via intravenous drip in severe cases. This individual was treated with intravenous bisphosphonate infusions from 7 months of age, which she continues to receive, alongside bone grafts and other operations (Balasubramanian, 2017).

Figure 1.2. Radiographic findings in Individual at 18 years of age affected by Cole Carpenter syndrome type 1. Reproduced from Rauch, et al. (2015). (A) Lateral skull radiograph showing severe midface hypoplasia. (B) The right arm is severely deformed. (C) In the legs, both femurs and tibias have undergone intramedullary rodding surgery. The right femur shows a large cystic area (asterisk) and no bone is visible in the mid-shaft area (arrow). (D) Wide epiphyses of the metacarpal and digital bones, thin cortices and a cystic appearance. Some of the end phalanges seem to be partially resorbed (arrows).

1.1.4 Underpinning the molecular basis of CCS1

The molecular basis of CCS1 is still under investigation: it is not yet known whether the phenotype arises from the single mutated gene or a combination of OI and other comorbidities. Whether the mutation is unique to CCS1 or is implicated in other collagen-associated disorders is another property which has also not yet been determined. These dilemmas are highlighted by premature skull suture closure (craniosynostosis) which results in multiple neurological defects and asymmetrical facial features (Timberlake, 2017). Craniosynostosis shares some characteristics with CCS1, however is caused by multiple genetic mutations which interact and cause the syndrome phenotype. It has been suggested that some reported cases

of CCS1 have been a combination of craniosynostosis and OI, as supported by Type III OI, another rare and severe form of these disorders (Eppley, 1994).

Whilst this 'combination' hypothesis is supported by the condition's rarity, there is strong evidence for the original two cases of Cole Carpenter and that of Amor and Balasubramanian being the same, independent disorder, owing to their extremely close similarity. In their reports, the quantity of collagen I production was reported to be normal (Amor, 2000), suggesting a different feature of cellular collagen is compromised. Using genome sequencing, this fault was later discovered to be with the molecular chaperone responsible for proper collagen folding, PDI.

The most recent study to date highlights a mutation in the prolyl-4-hydroxylase complex different to the one identified by Rauch (2015), yet still in the PDI domain. This is a heterozygous deletion of exons 5-8 (Ouyang, 2017) which also causes the same phenotypes as CCS1, suggesting the condition could be caused by other mutations in the P4HB gene, impacting the translated product in a similar way. This shows the importance of chaperone integrity for correct protein folding, whilst providing additional support for PDI's critical role in the syndrome.

1.2 PDI and the Prolyl-4-hydroxylase complex

1.2.1 The structure, activity and subcellular localisation of PDI

PDIA1, more commonly referred to as PDI, is the founding member of 21 other ER specific chaperones in this family of protein disulphide isomerase enzymes and, as a subunit of the prolyl-4-hydroxylase complex, an important enzyme in collagen folding (Benham, 2012; Kozlov, 2010). PDI is generally said to be endoplasmic reticulum localised, as shown in Table 1.2. More recent investigation into PDI and its substrate interactions have developed further insights into the roles of this protein in the ER (Diwaker, 2015).

To function as a disulphide oxidoreductase, PDI requires an electron donor to supply oxidising equivalents. Two ER localised proteins Ero1α and Ero1β selectively oxidise reduced PDI and therefore control its activity through a PDI-Ero1 redox cycle (Benham, 2000). This cycle fluctuates between reduced state PDI which binds proteins and performs its chaperone activity and oxidised state, which releases the folded protein (Moore, 2010).

Further research has revealed numerous members of the family localising to different areas of the cell, such as the membrane surface or lipid rafts, and displaying novel activities in these locations (Diwaker, 2015). Alongside the classical roles of disulphide bond formation and isomerisation in proteins synthesised in the rough endoplasmic reticulum, individual PDI family members have been implicated in breast cancer tumour suppression (Chen, 2005). This has also been observed in tau protein association in neurofibrillary tangles in Alzheimer disease neurones (Honjo, 2014).

Table 1.2. Common PDI family members and their intra- and extra-cellular localisation and functional roles.

PDI family protein	Role	Cellular location
Protein disulphide isomerase (PDI/PDIA1)	Molecular chaperone, hormone reservoir, thiol-disulphide oxidoreductase (Primm, 2001; Hosokawa, 2000)	ER, cell surface, nucleus, cytosol, secreted
PDIp/PDIA2	Pancreas specific molecular chaperone, oestrogen binding protein (Fujimoto, 2018)	ER

ERp57/PDIA3	Catalyses disulphide bond formation for MHC class I molecules, as part of calnexin-calreticulin cycle (Zhang, 2006)	Endoplasmic reticulum, nucleus, plasma membrane rafts, cell surface cytosol, secreted
ERp72/PDIA4	Molecular chaperone (Mazzarella, 1990)	Endoplasmic reticulum, cell surface, secreted
PDIR/PDIA5	Molecular chaperone for α1-antitrypsin and N-linked glycoprotein (Vinaik, 2013)	ER
PDILT	Testis specific molecular chaperone and oxidoreductase (van Lith, 2005)	ER
P5	Molecular chaperone, associated with Alzheimer's disease (Honjo, 2014)	Endoplasmic reticulum
ERp44/ TXNDC4	Molecular chaperone for IgM and adiponectin (Watanabe, 2019)	Endoplasmic reticulum, *cis*-golgi
ERp29	Protein secretion control and tumour suppressor (Chen, 2015)	Endoplasmic reticulum

In humans, the gene for PDIA1 (which will be subsequently referred to as PDI) is located on chromosome 17q25 (Galligan, 2012), with its translated product consisting of 508 amino acids. The protein was first identified in rat liver through its formation, isomerisation and reduction of disulphide bonds in ribonuclease A (Goldberger, 1963), which is a characteristic also found in the majority of other proteins in this family. All proteins in this family contain a thioredoxin-like structural fold consisting of both alpha helices and beta sheets in the following chain sequence: βαβαβαββα. This is a family-wide shared structural feature which contributes to both catalytic and non-catalytic activity (Darby, 1995). PDI itself contains four of these thioredoxin domains, with two outer catalytic domains (aa') containing the active motif Cys-x-x-Cys, as represented by the WCGHC motif as seen in Figure 1.3 panel A, and two non-catalytic inner domains (bb') which bind to substrate (Alanen, 2003). The catalytically active cysteines react with thiols of newly synthesised proteins to ensure the oxidoreduction of disulphide bonds, whilst the b and b' domains have no such active amino acids and are generally considered to be responsible for substrate recruitment (Klappa, 1998). Finally, the protein contains

a KDEL ER localisation sequence at the C terminus to retain it within the ER lumen, and a short interdomain sequence known as the X-linker region (Freedman 1998).

Oligomerization of PDI into its functional form involves the interaction of zinc ions (Zn^{2+}) with the catalytically active cysteines of the a and a' domains (Soloyov, 2004). This occurs by using the ion to bridge one of the catalytically active cysteines in a or a' between the cysteine present on the b' domain, as displayed on Figure 1.3. It has been proven that these active cysteines are critical, as replacement with serine removes PDI's catalytic activity, whereas the same replacement of cysteines present in the b' domain does not affect this process (Solovyov, 2004).

These catalytic domains are central to PDI's function, with both a and a' domains contributing to firstly its redox activity, allowing the introduction of new disulphide bonds via its oxidase activity, and the rearrangement of existing bonds via its isomerase activity. These are also vital for its separate chaperone activity: the
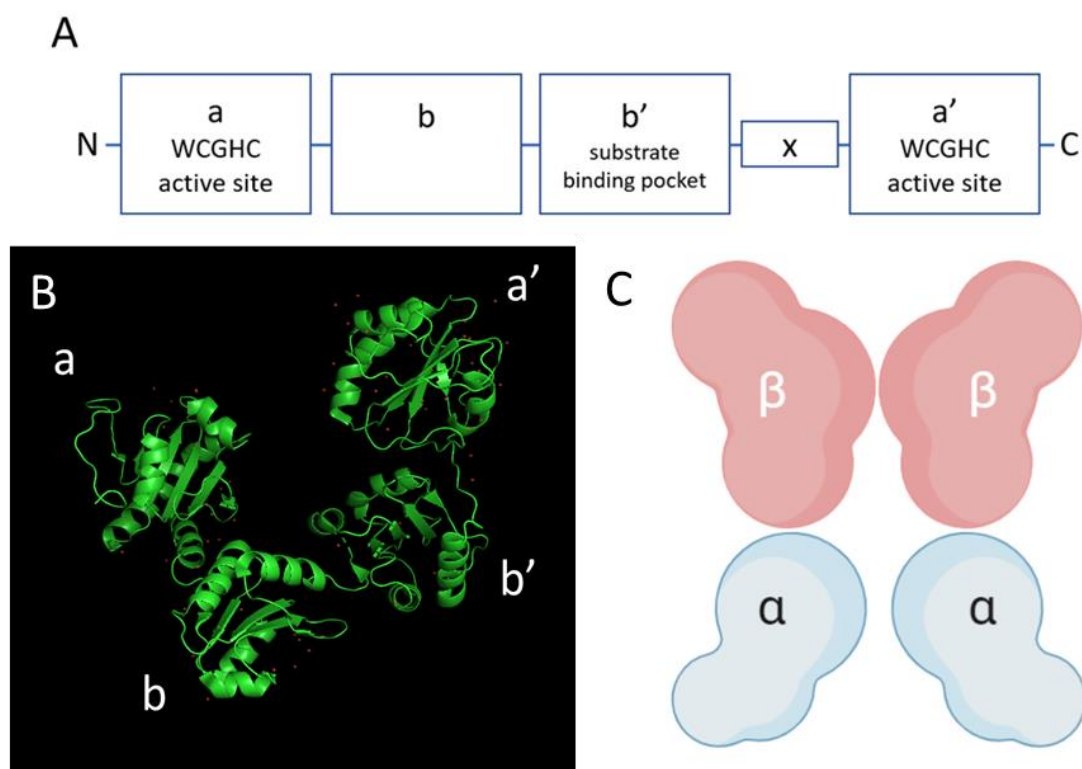
Figure 1.3. Structural overview of human PDIA1 (hPDI) and the collagen prolyl-4-hydroxylase complex. (A) Schematic diagram of PDI components with active site amino acid sequences. (B) Crystal structure of human PDI as determined by X-ray crystallography (PDB: 4EKZ). Catalytic domains (aa') and non-catalytic domains (bb') shown. (C) The prolyl-4-hydroxylase complex comprises two α subunits (P4HA) and two catalytic β subunits (P4HB/PDI).

introduction of disulphide bridges in the correct place on the target protein allows folding into the correct favourable tertiary structure arrangement. If these bonds are

11

incorrectly placed, it can introduce misfolding or unfolding of the target protein, activating the ER stress response pathways and leading to transient suppression of protein translation to allow cell recovery. The tyrosine residue at position 393 of the a' active site is replaced with a reactive cysteine in CCS1, in close in proximity to the other reactive cysteines C397 and C400 which catalyse PDI's activity.

PDI acts as a molecular chaperone for many proteins in the cell both *in vivo* and *in vitro* alongside collagen I (Moore, 2010). It also functions as a subunit of various enzyme complexes, including microsomal triglyceride transfer protein, and the prolyl-4-hydroxylase complex. To coordinate the folding of the collagen I triple helix, it forms half of the collagen prolyl-4-hydroxylase (C-P4H) complex shown in Figure 1.3C. This complex consists of P4HA and P4HB subunits, catalysing the formation of 4-hydroxyproline residues in collagen. The P4Hs involved in collagen biosynthesis recognize the characteristic X-pro-gly residue sequence in procollagen chains, catalyse the placement of disulphide bonds, and allow the proper folding into the triple helical tertiary structure (Gorres, 2011).

In vertebrates, this complex is believed to exist in two forms (I, II), as tetramers consisting of two alpha (P4HA1 or 2), and two beta (P4HB) subunits (Kivirikko, 1998). However, in recent literature, it has been suggested there are at least three P4HA isoforms contributing to the overall C-P4H complex (Gjaltema, 2017; Xiong, 2018). These may each have different affinities for P4HB and therefore influence the equilibrium between monomeric and heteromeric PDI in different cells and tissues. The type II P4HA gene product appears to be most common form in endothelial/epithelial cells, osteoblasts and chondrocytes, the latter two of which are essential for bone and osteoid formation and the secretion of cartilage (Myllyharju, 2003). Alongside P4HB, this may have implications in the onset of genetic disorders arising in these cell types, such as CCS1.

1.2.2 PDI in disease

Molecular chaperones must be able to properly bind to their target protein and perform their folding activity without error. Failure to do so may result in genetic diseases termed 'chaperonopathies' in which the target protein displays an unconventional phenotype, yet the chaperone is the protein at fault (Macario, 2007). Firstly, the chaperone must interact with other chaperones, cochaperones or cofactors via its oligomerisation domain to build a chaperoning complex. In the case

of PDI and collagen folding, this is the prolyl-4-hydroxylase complex which performs the folding and assembly of the polypeptides. This complex must then recognize and bind substrate. In this case, this is the two pro-α1(I) chains and one pro-α2(I) chain which make up collagen I. Finally, this complex must also interact with the protein degradation machinery of the cell to integrate protein-quality control networks, and ensure any misfolded proteins are destroyed (Macario, 2005). As previously discussed, PDI has additional roles as an oxidoreductase with co-factor and electron donor Ero1α, so mutations affecting this protein may have even more downstream effects than those of protein folding.

Mutated or modified PDI has been implicated in a variety of different disorders alongside CCS1, such as cancers, diabetes and pathogen entry in infectious syndromes (Xu, 2014; Grek, 2014; Stolf, 2011; Benham, 2012). Research into familial Amyotrophic lateral sclerosis (ALS) shows two P4HB gene mutations present via genotype association, resulting in raised expression levels in the spinal cord, alongside other endoplasmic reticulum stress markers (Atkin, 2008). Its upregulated presence has also been noted in infamous neurodegenerative conditions such as Parkinson's and Alzheimer's where it appears linked to tau protein in neurofibrillary tangles, and glioblastoma multiform brain tumours (Uehara, 2006; Xu, 2014).

The Cole Carpenter PDI mutation results in the gain of a reactive cysteine, which may result in the formation of unconventional inter and intra-molecular disulphide bonds between PDI and other proteins in the ER. This may cause large aberrant PDI complexes to form, resulting in the misfunction of PDI and its contribution to the CCS1 phenotype. ER stress has also been reported to be increased in CCS1 patients, supporting the above aggregation hypothesis (Rauch, 2015). Since the molecular mechanisms behind the PDI dysfunction in CCS1 are currently unknown, comparisons between CCS1 and other PDI-related syndromes may prove useful in distinguishing the cause and potential treatments for the syndrome. PDI inhibitor molecules such as PACMA 31 and 16F16 have been developed and have shown promise in multi-drug approaches to treat ovarian cancer, suggesting PDI has an important role in tumour growth and malignancy (Xu, 2012). In cancerous cells which upregulate PDI, reducing its expression may selectively cause cancer cell death through translation attenuation. This is instigated by the PERK arm of the ER stress response, a cascade of protein interactions triggered by aggregation of unfolded or misfolded protein in the ER (Limonata, 2019). With sufficient knowledge

13

of the molecular pathways undertaken by Y393C-PDI and the cellular phenotype displayed by Cole Carpenter cells, this modulation of PDI expression with drugs could potentially be applied as a therapy for Cole Carpenter syndrome.

1.3 Incorrect protein folding can elicit the ER stress response

1.3.1 The need for assisted protein folding

If proteins were left to spontaneously fold, this process would be significantly slower, or completely absent both *in vivo* and *in vitro*. Keeping the protein folding and packaging environment of the ER in the correct redox state alongside the actions of molecular chaperones, such as the PDI family, ensures that the formation and isomerisation of disulphide bonds occurs in the correct order. This enables the formation of proper protein higher-level structures, including the collagen triple helix a complex organisation of three pro-collagen chain (Fassio, 2002).
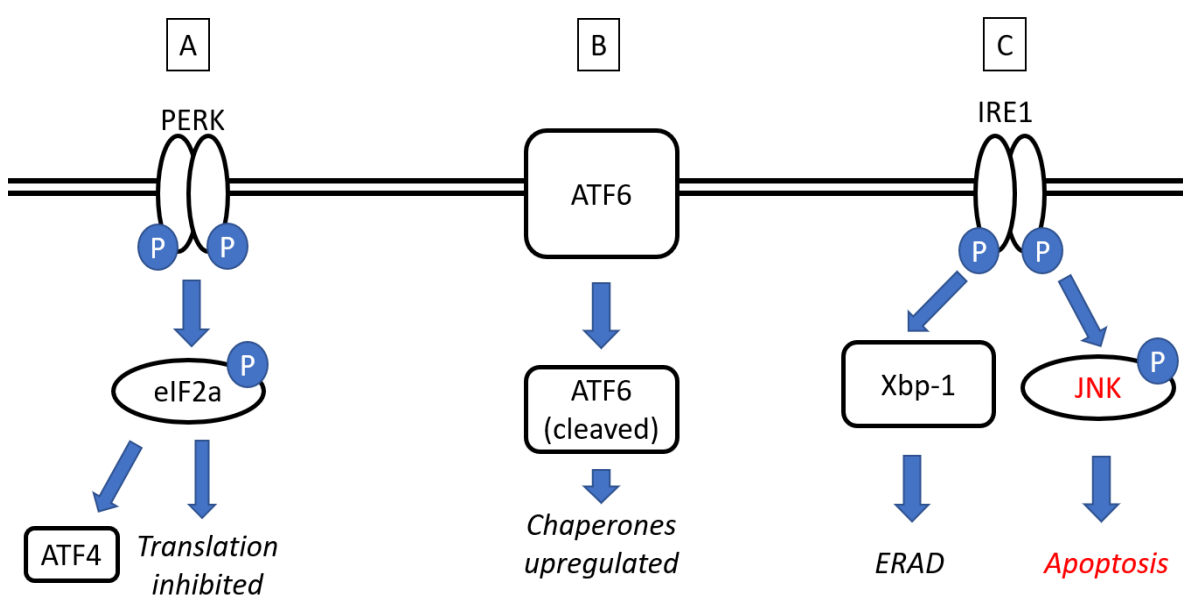
Figure 1.4. The three signalling arms of the ER stress response. (A) Phosphorylated PERK phosphorylates eIF2a, attenuating translation through ATF4. (B) ATF6 is activated when cleaved, translocates to the nucleus and binds to UPR-upregulated gene promotors. (C) IRE1 cleaves Xbp-1 leading to ER-associated protein degradation (ERAD). Chaperones EDEM, PDI and Grp78 guide misfolded proteins to the cytosol for ubiquitin-proteosomal degradation. If neither A, B or C can return cellular or ER homeostasis, the response aims towards JNK mediated apoptosis.

The Unfolded Protein Response (UPR), also known as the ER stress response, is activated when there is an accumulation of unfolded or misfolded proteins in ER lumen. It has three main functions, which are depicted in Figure 1.4. These are either restoring normal function of the cell by stopping mRNA translation (A); upregulating molecular chaperone function through protein kinase R (PKR)-like endoplasmic reticulum kinase (PERK) initiation (B); or to degrade misfolded or unfolded proteins through ER-associated protein degradation (ERAD) (C).

15

If these aims are not achieved and stress remains unresolved, programmed cell death via apoptosis prevails (Hetz, 2018). During pathway A, molecular chaperones are upregulated to 'rescue' the misfolded protein, meaning proteins involved in this pathway are sensitive to the activity of PDI. ER transmembrane kinase (PERK) is activated by oxidised PDI (Kranz, 2017), whereas PDI-like protein ERp57/PDIA4 keeps PDI in a reduced state in the absence of ER stress, as shown in Figure 1.5.
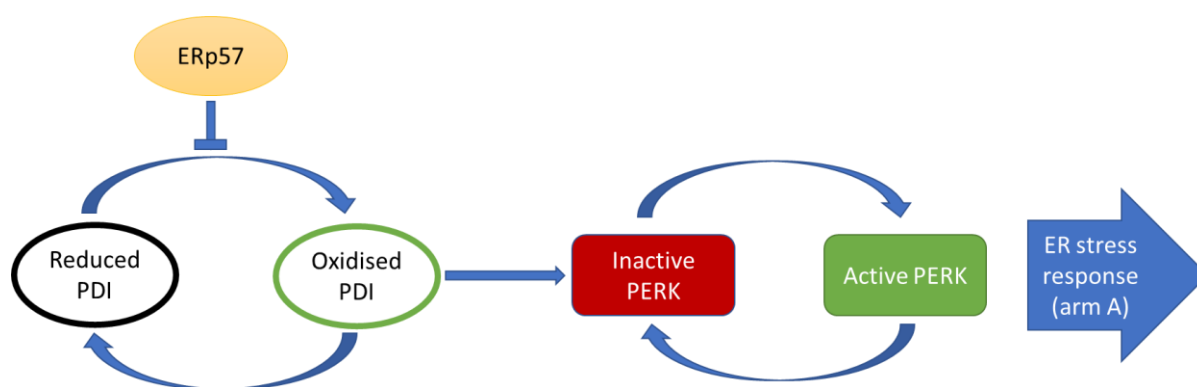
Figure 1.5. ERp57 acts as a PDI inhibitor, retaining a reduced state in the absence of ER stress. When the ER's capacity to fold proteins becomes impaired, or there is an aggregation of misfolded protein, as is hypothesised in Cole Carpenter syndrome, ERp57 inhibition of PDI is removed, allowing the activation of PERK and the progression of the translation-inhibiting arm of the ER stress response.

Some PDI-related chaperones are known to be able to compensate for PDI or another chaperone if a mutation renders them dysfunctional (Lee, 2006). ERp72 can help to fold specific proteins in the ER lumen when the function of ERp57, shown by the schematic in Figure 1.5, is compromised (Soldà, 2006). It is currently unknown if other chaperones are upregulated in Cole Carpenter syndrome to compensate for Y393C-PDI. However, PDI's multifunctional roles may pose an issue since the upregulated chaperones may not be able to compensate for all the protein's activity within the cell. Furthermore, sequence or structural homology to other proteins does not necessarily lead to effective compensation of function (Mirny, 1999). For example, the redox potential of ERp57 means it can form complexes with other ER associated proteins which enable glycoprotein folding within the ER lumen (Koivunen, 1996). It also shares sequence similarity in essential b and b' domains, alongside shared a and a' catalytic sites with PDI. Despite this homology, ERp57 cannot substitute PDI in the C-P4H complex, therefore cannot

compensate for its protein folding or oxidoreductase roles if PDI itself is compromised (Koivunen, 1996).

Functional studies in yeast have shown that ERp46 can substitute PDI's disulphide bond formation *in vivo*, and this has been confirmed in human embryonic stem cell lines (Knoblach, 2003; Araki, 3013). However, PDI's role in oxidative protein folding is key, and no other member of this protein family can fully contribute for its loss (Rutkevich, 2010). This infers complete compensation in Cole Carpenter syndrome is unlikely, therefore suggesting an explanation for the severity of the phenotype.

1.3.2 *Lysosome-mediated waste disposal functions alongside ER-associated protein degradation*

It has been proposed that ERAD-independent mechanisms of misfolded protein clearance exist in the ER (De Leonibus, 2019). These processes utilise the well characterised lysosomal waste disposal system, which directs the effective removal of misfolded proteins both inside and outside the ER (Zhao, 2019). This process of *autophagy* is characterised by vesicular engulfment, digestion by lytic enzymes, and subsequent destruction of the misfolded protein. These intracellular organelles typically measure 0.5 - 1.5 μm in diameter and contain acid hydrolase digestive enzymes to digest any misfolded or unfolded proteins aggregating in the cytoplasm (Araujo, 2020). They have also been implicated in cancer metastasis and development, upon location to the plasma membrane (Sarafian, 1998).

Lysosome associated membrane glycoprotein (LAMP2) is a commonly used marker for lysosomes in cells, potentially contributing to the regulation of pH and vesicle integrity, although these functions are yet to be confirmed. In theory, these organelles should work alongside ERAD to maintain ER homeostasis by destroying improperly folded proteins, however it is hypothesised that this system may be affected in CCS1. Due to the ER stress resulting from potential misfolded collagen aggregation, there are possible downstream effects on other intracellular protein packaging and transport systems, such as that of the lysosomes. Certainly, it is already known that the second variant of Cole Carpenter syndrome (CCS2) results from a mutation in SEC24D, a gene encoding a transport protein enabling ER to Golgi vesicle budding via the COPII anterograde transport system. This therefore impacts the effective transport and distribution of collagen from its vesicular to

deposited forms, as opposed to the chaperone mediated folding occurring prior to this.

1.3.3 Proline hydroxylation keeps collagen stable
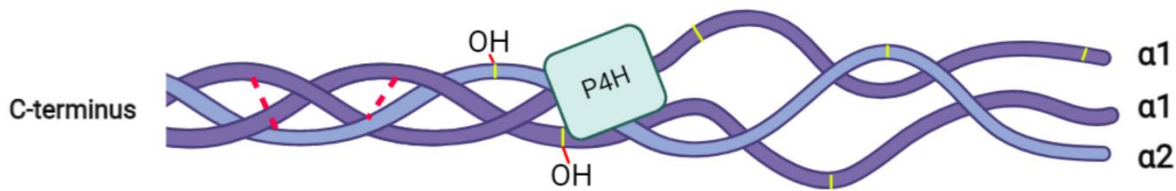
Figure 1.6. The Collagen I triple helix consists of two pro-α1(I) chains and one pro-α2(I) chain. Folding into the right-handed triple helix is assisted by P4H, with other enzymes involved not shown. Each chain consists of 1050 amino acids. Proline residues (yellow) in X-Pro-Gly sequences are hydroxylated by P4HA. P4HB assembles the disulphide bridges allowing the three chains to align. The triple helix then 'zips' up into the rigid, properly folded structure.

Triple helix formation as shown in Figure 1.6. is essential for the proper function of collagen produced in the cell. It enables the transportation of type I procollagen chains pro-α1(I) and pro-α2(I) from the ER to the Golgi apparatus, which facilitates secretion from the cell to form the extracellular fibrils that will support mineral deposition in bone (Malhotra, 2015). As previously mentioned, the C-P4H complex is essential for this folding. This protein complex comprises the P4HA and P4HB gene products and catalyses the hydroxylation of proline in collagens and collagen-like proteins, as shown in Figure 1.6. The resultant 4-hydroxyproline residues ensure increased stability of collagens under physiological conditions, enabling extracellular matrix growth and bone formation. Subsequently, collagen chains that do not contain 4-hydroxyproline residues cannot fold into the essential triple helices and are very unstable at physiological temperature. These unstable chains are either degraded by the cell after causing ER stress, as shown in the response pathways highlighted in Figure 1.4, or slowly secreted as non-functional proteins (Pihlajaniemi, 1991). The levels of these 4-hydroxyproline residues indicates the quality of collagen production by the cell, and if decreased in CCS1 positive cells, could provide a potential explanation to the basis of CCS1 phenotypes. Endoplasmic reticulum Associated protein Degradation (ERAD) relies on PDI to chaperone aggregated protein to the cytosol for degradation (Cox, 1993). However, if PDI is mutated and cannot perform this function, this slowly secreted protein may lead to the unresolved ER stress hypothesised to cause the Cole Carpenter

18

phenotype. As described in Section 1.3.1, this may lead to the onset of apoptosis, owing to both the toxic effects of aggregation and a lack of useable collagen in the affected cells.

1.4　Project overview

1.4.1　Cole Carpenter syndrome is related to PDI structural integrity

Expressing properly functioning PDI is integral to cell survival and the maintenance of ER homeostasis, however its molecular role in CCS1 has yet to be elucidated (Freedman, 1994). This mutation occurs close to the collagen binding site and appears to result in a 'gain of dysfunction' for the affected PDI. This may result in misfolded collagen as opposed to a 'loss of function' resulting in an unfolded protein. The consequential ER stress may lead to downstream effects on other systems in the cell, eventually compromising cell viability and/or collagen deposition. This may affect the amount of functional collagen present in osteoid and the formation of new bone, providing a molecular basis to the brittle bone OI phenotype consistent with clinical observations.

This project aimed to visualise and quantify the difference between both CCS1 cells and Y393C-PDI mutant cells compared to control normal cells. Due to variability in collagen I secretion and composition, a range of cell types has been used including osteoblast, fibroblast, and epithelial cell lines, alongside patient derived primary fibroblasts and control cells. Observing differences between multiple cell types helped to begin determining why the phenotype is so severe in bone, despite collagen I being expressed abundantly in all connective tissues, alongside Collagen II and III. Key experiments include assessing the localisation of wild-type PDI and Y393C-PDI using immunofluorescence, using an alkylation trapping approach to identify interacting proteins by co-immunoprecipitation, and investigating the potential downstream effects of Y393C PDI on lysosome mediated autophagy. We expect that PDI interactions with the C-P4H complex, or its electron donor Ero1 α may be affected by this mutation, due to their important roles in the regulation of PDI activity. Live and fixed cell imaging of lysosomes in CCS1 cells provided a deeper understanding of the spatial cellular effects of the syndrome on subcellular organisation, and potential impacts on other protein degradation and waste disposal systems, other than those of the ER. These experiments will help the understanding of the molecular basis of Cole Carpenter syndrome and provide mechanistic clues for other types of osteogenesis imperfecta. The information in this thesis may also be used in future to develop novel therapies for CCS1 and related bone fragility disorders.

2 MATERIALS AND METHODS

2.1 Materials

The following section lists all materials used for experiments in this thesis. Solutions were prepared in type I laboratory H_2O.

Table 2.1. List of Antibodies used for Western Blotting

	Antibody	Dilution	Species raised in	Supplier	Product code
Primary antibodies	α-P4HB (RL90)	1:1000	Mouse	Abcam	Ab2792
	α-PDI	1:1000	Rabbit	Benham lab	N/A
	Myc-tag (9B11)	1:1000	Mouse	Cell Signalling	2276S
	Collagen I	1:1000	Goat	Southern Biotech	AB_2753206
	Ero1 α	1:1000	Rabbit	Cell Signalling	3264T
Secondary antibodies	GAMPO	1:3000	Goat α-mouse	DAKO	PO447
	SARPO	1:3000	Swine α-rabbit	DAKO	P0217

Table 2.2. List of Antibodies used for Immunofluorescence

	Antibody	Dilution	Species raised in	Supplier	Product code
Primary antibodies	Anti-P4HB (RL90)	1:200	Mouse	Abcam	Ab2792
	Anti-PDI	1:100	Rabbit	Benham lab	N/A
	Myc-tag (9B11)	1:200	Mouse	Cell signalling	2276S
	Tubulin	1:100	Rabbit	Abcam	ab4074
	Lamp2b	1:100	Rabbit	Abcam	Ab118959
	Collagen I	1:1000	Goat	Southern Biotech	AB-_2753206
Secondary antibodies	AlexaFluor488 α-mouse	1:1000	Donkey	Invitrogen	A-21202
	AlexaFluor488 α-rabbit	1:1000	Donkey	Invitrogen	A-21206
	AlexaFluor594 α-mouse	1:1000	Donkey	Invitrogen	A32744
	AlexaFluor594 α-rabbit	1:1000	Donkey	Invitrogen	A32740

Table 2.3. List of Fluorescent dyes used in live cell imaging

Fluorescent dye	Dilution	Incubation time (min)	Product code
ER-Tracker™ Blue/White DPX	1:1000	20	E12353
Lyso-Tracker™ Red	1:1000	20	L7528

2.2 Methods

2.2.1 Cell culture

2.2.1.1 *Retrieval of cryopreserved cells*

Frozen vials of human BJ fibroblast (ATCC, CRL-2522), human fibrosarcoma HT1080 cells (ATCC, CCL-121), or human osteoblast-like Saos-2 (ECACC 89050205) cell lines, suspended in 90% FBS with 10% dimethyl sulfoxide freezing medium (DMSO) in 1 ml cryotubes, were retrieved from short term -80 $^{\circ}$C storage, or long term LN2 at -140 $^{\circ}$C. Cells were thawed, centrifuged at 300 g for 1 minute to remove freezing medium, then resuspended in 10 ml of Minimal Essential Medium (MEM, ThermoFisher Scientific, 15188319) Dulbecco's Modified Eagle Medium (DMEM, ThermoFisher Scientific, 31095029) for HT1080 cells, or McCoy's 5a medium (ThermoFisher Scientific, 22330021) for Saos-2, in a T75 (TPP, 90076) or T25 flask (TPP, 90026). DMEM and MEM were supplemented with 8% Foetal Bovine Serum (FBS, Invitrogen, F7524), 10 µg ml^{-1} penicillin, 100 µg ml^{-1} streptomycin (ThermoFisher Scientific, 15410) and 2 mM Glutamax (Gibco, 35050-038). McCoy's 5a was supplemented with 10% FBS 10 µg ml^{-1} penicillin, 100 µg ml^{-1} streptomycin (Gibco, 15410) and 2 mM Glutamax (Gibco, 35050-038). Cells were added to the flask, resuspended, and allowed to settle in a humidified incubator at 37 $^{\circ}$C and 5% CO_2.

2.2.1.2 *Maintaining cell lines in culture*

Cells were passaged at 80% confluency as follows: spent media was removed from the flask, and cells were washed twice in 5 ml or 10 ml (T25 or T75 respectively) room temperature sterile Phosphate Buffered Saline (PBS - Gibco, 100100023) comprising of 1.05 mM KH_2PO_4, 155.2 mM NaCl, 3 mM Na_2HPO_4-$7H_2O$, pH 7.4. Following this, 1 ml of trypsin (ThermoFisher Scientific, 15400054) was added for 1 minute to dissociate the cells, then either split into new flasks at 1:10 dilution in complete medium, or seeded into 6 cm sterile dishes (TPP, 93060) for transfection. Patient and control cells were media changed every 24 hours, and grown in both T25 flasks or 6 well plates.

2.2.1.3 Thawing and maintaining primary cells in culture

Primary fibroblasts derived from both CCS1 patient and a control were thawed, centrifuged at 300 g for 1 minutes to remove freezing medium, then resuspended in 10 ml of Roswell Park Memorial Institute (RPMI) medium supplemented with 10% Foetal Bovine Serum (FBS, Invitrogen, F7524), 10 µg ml^{-1} penicillin, 100 µg ml^{-1} streptomycin (Gibco, 15410) and 2 mM Glutamax (Gibco, 35050-038), in a T25 flask (TPP, 90026). Cells were grown in a Category level 2 (CL2) flow hood, and stored in a CL2 humidified incubator, and media changed every 24 - 26 hours.

2.2.1.4 Plasmid generation and transient transfection

Plasmids for wild-type PDI-myc with Neomycin mammalian resistance and Y393C-PDI-myc were designed on Snapgene Viewer 5.1.2 and ordered through Vectorbuilder (en.vectorbuilder.com). This consisted of purified plasmid and a cryopreserved transformed E coli stock for future amplification.

HT1080 or Saos-2 cells in 6 cm sterile dishes or 6 well sterile plate were grown at 37 °C, 5% CO_2 in a humidified incubator. If performing immunofluorescence, cells were plated onto 10 mm sterile coverslips (VWR, 631-0148P). For each experiment, a negative control with no plasmid and a positive control was used. This consisted of either Ero1α-myc construct to ensure transfection efficiency or WT-PDI-myc construct to compare mutated alongside wild-type PDI. Transfection was carried out at 70 - 90 % cell confluency using Polyplus Transfection JetPEI® DNA transfection reagent (VWR, 101-10N) for HT1080 cells, and Lipofectamine 3000 (Invitrogen, L3000015) for both Saos-2 and HT1080. JetPEI transfection complexes for each well of a 6 well plate contained 100 µL NaCl, 6 µL JetPEI transfection reagent and 3 µg plasmid. For each 6 cm dish, these were raised to 250 µL, 10 µL and 5 µg respectively. Lipofectamine complexes contained 375 µL Gibco Opti-MEM™ Reduced Serum Medium (11058021, ThermoFisher), 7 µL Lipofectamine 3000 reagent, 10 µL P3000 reagent, and 5 µg plasmid. Negative controls included the addition of all transfection reagent components without the plasmid, to control for any effects on cell viability.

2.2.1.4.1 JetPEI transfection

In a sterile flow hood, JetPEI reagent and plasmid were prepared in separate Eppendorf tubes with NaCl, before mixing as per the manufacturer's instructions.

The solution was vortexed for 5 sec and centrifuged at 16,000 g for 5 minutes, then incubated at room temperature for 30 minutes. After incubation, the solution was added dropwise to the dishes.

2.2.1.4.2 Lipofectamine transfection

In a sterile flow hood, Lipofectamine 3000 reagent and P3000 reagent were prepared in 125 µL of Opti-MEM™, and the plasmid was prepared in a separate Eppendorf containing 250 µL Opti-MEM™. These solutions were gently vortexed, then the plasmid containing tube was mixed into the reagent containing tube, and vortexed for 1 minutes and left to incubate at room temperature for 5 minutes. During this time the cells were retrieved from the incubator and gently washed twice in PBS. After incubation, the mixture of Opti-MEM™, plasmid and reagent were gently added dropwise to cells and left for an hour in a humidified incubator at 37 °C, 5% CO_2. After an hour, 1 ml normal media (McCoy's 5a or DMEM) was added to the dishes which were then left overnight in the incubator for plasmid uptake.

2.2.1.4.3 Plasmid DNA amplification

A Qiagen Plasmid Maxi Kit with transformed *E. Coli* cultures was prepared according to the manufacturer's instructions. To obtain DNA, *E. coli* cells were lysed and pelleted by centrifugation to obtain soluble elements which were then filtered to isolate DNA. DNA was dissolved in 1x TE buffer; pH 8, 10mM Tris (Sigma Aldrich, T1503), 1 mM EDTA (ThermoScientific, AM9260G). The concentration of the DNA was determined using a NanoDrop 1000 Spectrophotometer (ThermoScientific). Extracted plasmid DNA in 0.5 ml TE buffer was stored at -20 °C prior to use.

2.2.1.4.4 Cryopreservation of cells

After standard cell culture using protocol 2.2.1.2 (cell lines) and 2.2.1.3 (primary cells), cell suspensions were aseptically transferred to a 50 ml falcon tube and centrifuged at 200 g for 5 minutes. The supernatant was carefully removed and the pellet resuspended in DMSO freezing medium (10% DMSO with 90% FBS), before being aliquoted into cryogenic storage tubes while mixing to maintain equal cell distribution in suspension. These were placed in an isopropanol chamber (Mr Frosty) and stored at –80°C overnight, before being transferred to long term LN2 storage the following day.

2.2.2 Preparation for western blot

2.2.2.1 *Cell lysis*

In sterile conditions, cells grown in 6 cm dishes to 90% confluency were washed twice with 2 ml cold PBS and lysed in 1x MNT ice cold lysis buffer consisting of 20 mM MES (Sigma Aldrich, M8250), 30 mM Tris-HCl (Sigma Aldrich, T3253), 100 mM NaCl (Sigma Aldrich, S7653), pH 7.4. This was supplemented with 1% v/v Triton X-100 (Sigma Aldrich, X100) and 10 µg ml^{-1} protease inhibitor cocktail consisting of 104 mM AEBSF, 80 µM Aprotinin, 4 mM Bestatin, 1.4 mM E-64, 2mM Leupeptin, 1.5 mM Pepstatin A (Sigma Aldrich, P8340). Cells were lysed for 10 minutes on ice. The lysates were scraped from the dish using a Corning Cell Lifter (CLS3008) and transferred to separate 1.5 mL Eppendorf tubes (Starlab, S1615-5550). Lysates were centrifuged at 16,000 g for 10 minutes at 4 °C to pellet the nuclei. The nuclear pellet was discarded, and lysates transferred to a new 1.5 ml Eppendorf. These were either snap frozen in liquid nitrogen for storage at -20 °C, or their protein content quantified for western blotting.

2.2.2.2 *Protein quantification by Bicinchoninic acid (BCA) assay*

A BCA assay was performed on all cell lysates using a QuantiProTM BCA Assay Kit to calculate protein concentration (ThermoFisher Scientific, 10678484) in a 96 well plate (ThermoFisher Scientific, 10656853), after the removal of the nuclear pellet. A 2 mg mL^{-1} BSA (Sigma Aldrich, A7517) stock was used to prepare standards of the following concentrations: 0, 25, 125, 250, 500, 750, 1000, 1500, 2000 µL ml^{-1} in distilled water. 10 µL aliquots of each standard and each cell lysate were added to individual wells in duplicate. 200 µL of working reagent was then added to each well and the plate was incubated at 37 °C for 30 minutes. The absorbance of each well at 562 nm was subsequently measured on a standard plate reader. The standards were used to plot a standard curve of concentration to absorbance, which was used to determine the concentration of the cell lysates.

2.2.2.3 *Protein sample preparation*

Samples containing a maximum volume of 20 µL consisted of cell lysate mixed with at 1:1 ratio with 2x Laemmli loading buffer (65.8 mM Tris-HCl, pH 6.8, 26.3% (w/v) glycerol, 2.1% SDS and 0.01% bromophenol blue) (Bio-Rad, 161-0737). For standard reducing SDS-PAGE, this was supplemented with 100 mM Dithiothreitol

27

(DTT) (Sigma Aldrich, 04689721) reducing agent. For graded reduction of resistant disulphide dependant protein complexes, 50 mM, 100 mM and 150 mM concentrations of DTT were used. Under non-reducing SDS-PAGE, this was replaced with the same volume of MNT lysis buffer. These samples were boiled for 5 minutes at 95 °C on a heating block and centrifuged for 5 minutes at 16000 g.

2.2.2.4 *Protein separation by SDS-PAGE*

1 mm thick SDS-PAGE gels (10%) were cast using the Hoefer Dual Gel Caster (Hoefer, SE245). The resolving gel comprised of 4.8 ml dH2O, 2.5 ml 40% acrylamide (Severn Biotech Ltd, 20-2400-10), 2.5 ml 1.5M Tris, pH 8.8, 0.1 ml 10% SDS (Severn Biotech Ltd, 20-4000-10), 0.1 ml 10% APS (Sigma Aldrich, A3678) and 4 µl TEMED (ThermoFisher Scientific, 10689543). The stacking gel was cast above the resolving gel with a 10 well comb and comprised of 1.5 ml dH$_2$O, 0.25 ml 40% acrylamide, 0.25 ml 1 M Tris pH 6.8, 20 µl 10% SDS, 15 µl 10% APS, 2 µl TEMED. Samples were loaded onto the SDS-PAGE gel alongside a pre-stained protein ladder (Bio-Rad, 1610374). The gel was run in a tank containing 1x Tris-Glycine running buffer (25 mM Tris, 192 mM glycine, 0.1% SDS, pH 8.3) diluted from a 10x stock (Bio-Rad, 1610772) at 50 mA for 30 minutes.

2.2.2.5 *Membrane transfer*

For protein transfer, the SDS-PAGE gel was placed against a methanol primed polyvinylidene fluoride (PVDF) membrane (Merek Millipore, T831.1) between four pieces of filter paper cut to size and transferred in ice cold 1x transfer buffer (25 mM Tris, 1.5 M glycine and 20% methanol) at 4°C for 2.5 hours at 150 mA using a Bio-Rad Mini Trans-Blot Cell kit (Bio-Rad, 1703930).

2.2.2.6 *Blocking and primary antibody incubation*

The membrane was blocked in 5% milk with Tris buffered saline with Tween (TBS-T; 10 mM Tris, 150 mM NaCl, pH 8, supplemented with 0.1% Tween20 (VWR, 663684BP) for 1 hr at room temperature. The membrane was washed in 5ml TBS-T five times, then incubated overnight at 4 °C with the relevant primary antibody (Table 2.1.) in 5% (w/v) milk in TBS-T or 4% (w/v) BSA in TBS-T.

2.2.2.7 Secondary antibody incubation

After primary antibody incubation, the membranes were washed in 5 ml TBS-T five times for 5 minutes each. Membranes were then incubated with the relevant horseradish peroxidase (HRP) conjugated secondary antibodies shown in Table 2.1 for 1 hr at room temperature (Goat Anti-Mouse Immunoglobulins/HRP (DAKO, P0447); Swine Anti-Rabbit Immunoglobulins/HRP (DAKO, P0217)). All secondary antibodies were diluted 1:3000 in 5% milk TBS-T.

2.2.2.8 Signal detection

Membranes underwent 5-minute washes in TBS-T four times, then were briefly dipped in TBS before incubating the membranes with ECL (Amersham, RPN2209) and visualizing on light sensitive film with an x-ray developer (XOMAT) (ThermoFisher Scientific, PI34090). Post development, some membranes were stripped of primary and secondary antibodies by washing twice in 5 ml stripping buffer (0.15% glycine, 0.01% SDS, 1% Tween 20) for 10 min, then washed twice in PBS for 10 min, then washed twice in TBS-T for 5 minutes. The membranes were then blocked overnight at 4 °C ready for antibody reprobe with a β-actin loading control.

2.2.3 Immunoprecipitation

2.2.3.1 Cell lysis and Bead preparation

HT1080 or Saos-2 cells were lysed as in 2.2.1, and 100 µl of Protein A Sepharose beads were prepared by washing twice in MNT buffer (pH 7.4, 20 mM MES, 30 mM tris-HCl, 100 mM NaCl) and resuspending in 900 µl of MNT lysis buffer (MNT buffer, with Protease Inhibitor). The beads were centrifuged at 4000 g at 4 °C, for 1 minute. The supernatant was removed and discarded, and the wash repeated.

2.2.3.2 Immunoprecipitation of desired protein

Immunoprecipitations (IP) were carried out using polyclonal anti-PDI diluted 1:1000 immobilised on 50 µl of a 20% suspension of Protein A Sepharose beads (Sigma, P9424-1ML). The suspension was incubated while mixing for either an hour at 4°C anti-PDI and followed by three washes with 1x MNT lysis buffer.

Supernatant was removed and 200 µl of cell lysate added and incubated for the 3 hours at room temperature. The beads were spun at 4000 g for 1 minutes at 4 °C, and supernatant removed and snap frozen in liquid nitrogen. The beads were resuspended in 500 µl MNT lysis buffer, and washed 2 - 4 times, depending on the volume of beads remaining. If preparing for western blot, the supernatant was discarded, and beads resuspended in 50 µl 2x Laemmli sample buffer. This was boiled at 95 °C, for 5 minutes then spun at 16,000 g for 5 minutes at 4 °C. The 50 µl sample buffer was removed and prepared for analysis by western blot described in protocol 2.2.2. If preparing for mass spectrometry, beads were resuspended in 50 µl elution buffer (100 mM Tris-HCl, pH 7.6, 4% SDS, 0.1 M DDT) and boiled at 95 °C for 5 minutes then spun at 16,000 g for 5 minutes at 4 °C. This was then prepared for Quantitative Evaluation of Filter Aided Sample Preparation (FASP) digest.

2.2.3.3 FASP digest

Cell lysates prepared for LC-MS were digested using Filter Aided Sample Preparation (FASP) using the Expedeon FASP kit (Expedeon Ltd, 44255) as per manufacturer's instructions. The VWR microstar 17R microcentrifuge was operated at 10, 000 G. 1 ml eppendorfs containing 200 µg of total protein were mixed with 200 µL of 8 M urea in 0.1 M Tris/HCl, pH 8.5. in the ultrafiltration unit and then centrifuged at 20 °C, for 15 min.

100 µL of the urea/protein mix was pipetted into the filtration unit, and the units were centrifuged again. To alkylate reduced disulphide bonds, 50 µL of 0.05 M iodoacetamide in urea was added to the filters, and samples were incubated in darkness for 20 min. Filters were washed three times with 100 µL of urea followed by three washes with 40 µL 50mM ammonium bicarbonate solution. The samples were digested in 40 µL mass spectrometry grade trypsin gold (Promega, V528A) at 37 °C for 18 hours, at an enzyme to protein ratio of 1:100. Spin filters with digested peptides bound were transferred to a fresh tube and collected by two sequential washes with 40 µL 50 mM ammonium bicarbonate and one with 50 µL 0.5 M NaCl. Samples were acidified in 1 µL 1% TFA and freeze dried to reduce volume. They were resuspended in 3% acetonitrile, 0.1% formic acid for LC-MS/MS analysis.

2.2.3.4 Analysis by LC-MS/MS

Digested samples were prepared for Liquid Chromatography-Mass spectrometry (LC-MS). Protein minimum score was set to 20, and successful hits searched against a human reference proteome, alongside known Proteomic experiment contaminants using PEAKS X+. Post-search, the peptide False Discovery Rate (FDR) was set at 1% and a filter of 2 unique peptides applied.

2.2.4 Immunofluorescence

2.2.4.1 Preparation and fixation of cells

Cells were plated onto 16 mm round coverslips (ThermoFisher Scientific, 12313138) and, if necessary, transfected as described in protocol 2.2.1.4. Once cells reached 70 - 80% confluence, they were subjected to immunofluorescence. Spent media was carefully removed and cells were washed in 2 ml PBS supplemented with 100 mg L^{-1} $CaCl_2$ and 100 mg L^{-1} $MgCl_2$ (PBS++) (ThermoFisher Scientific, 14040091) 3 times for 5 minutes. Cells were fixed using 1 ml 4% paraformaldehyde (PFA) (Fixative A) from a 16% w/v stock (Agar Scientific, AGR1026) in a fume hood or Fixative B for 10 minutes to preserve the cytoskeleton (where stated). Fixative B consists of 3.7% paraformaldehyde, 0.02% glutaraldehyde, 50 mM PIPES (piperazine-N,N'-bis(2-ethanesulfonic acid)), 5 mM EGTA (ethylene glycol-bis(β-aminoethyl ether)-N,N,N',N'-tetraacetic acid, 2 mM Magnesium sulphate, pH 6.8. The fixative was then removed and cells washed twice in PBS++ for 5 minutes each. To permeabilise cells, 0.1% Triton X-100 was added for 10 minutes at room temperature.

2.2.4.2 Blocking and Primary antibody incubation

In a humidity chamber, each slide was blocked in 50 µL filtered 2% w/v BSA in PBS for 30 minutes at room temperature. After blocking, excess block was removed. Slides were incubated in a humidity chamber with primary antibody diluted in 2% BSA in dilutions as shown in Table 2.2. Coverslips were incubated either overnight at 4 °C, or at room temperature for 2 hours depending on antibody sensitivity.

2.2.4.3 Secondary antibody incubation and slide mounting

After primary antibody incubation, the slides were washed in a 6-well plate with PBS++ for 5 minutes three times each, gently rocking. Washed coverslips were incubated with secondary antibodies diluted in BSA at 1:1000 shown in Table 2.2. The Alexa Fluor 594/488 secondary antibodies were added to the slides on parafilm in a dark chamber, then coverslips were covered with a humidity chamber for 1 hr at room temperature. After five PBS++ washes for 5 minutes, coverslips were incubated with 50 µL of 4% DAPI in the dark for 10 minutes. Coverslips were briefly placed in PBS++ to wash, and placed face down onto clean glass slides with 5 µL soft set Vectashield (Vector, H-1000). Excess mountant was removed with tissue
32

and the slides were sealed with nail varnish and kept in the dark at 4°C before imaging with a laser scanning confocal microscope (Zeiss 800 with airyscan).

33

2.2.5 Cell viability with PDI inhibitor assay

2.2.5.1 Equipment and treatment setup

Saos-2 cells were seeded at 67,000 cells per well into a 96 well microplate (ThermoFisher Scientific, 167008) and left overnight in a humidified incubator to equilibrate until 70% confluent. The plate was split into 3x15 well sections, and each section transiently transfected with the appropriate PDI-myc construct or media changed with no plasmid. Surrounding wells were filled with a sterile liquid (PBS) to minimise evaporation edge effects, and 100 µl of McCoy's 5a media as an assay control was set up in triplicate. The cells were left overnight for plasmid uptake. For PDI inhibition experiments, the following day each horizontal row was treated with set concentrations (0, 4 µM, 6 µM, 8 µM and 10 µM) of either PACMA 31 (Merck Life Sciences, SML0838), or 16F16 (Merck Life Sciences, SML0021) PDI inhibitors were diluted in 20 µl McCoy's 5a media. The plate was incubated for 1 hr at 37°C, 5% CO_2, then assessed for viability.

2.2.5.2 Orangu^{TM} assay for cytotoxicity

After transfection, or incubation with the relevant PDI inhibitor, 10 µl of Orangu^{TM} solution was added to each well, including McCoy's 5a media controls but apart from PBS evaporation controls. The plate was re-incubated for 3 hours in a humidified incubator, then the absorbance read at 450 nm on a Biotek microplate reader using Gen5 data analysis software.

2.2.6 Live cell imaging

2.2.6.1 Culture preparation and fluorescent staining

Saos-2 and HT1080 cells were grown in 35 mm glass bottom dishes (Ibidi, 81218-200) in 2 ml of the appropriate media, until 70% confluent in a humidified incubator. 24 hours prior to imaging these were transfected with the appropriate PDI-myc construct or left non-transfected. Thirty minutes before imaging, cells were washed twice in PBS warmed to 37°C, then incubated with 0.1% fluorescent dye (5 µg, supplied at 5 mg/mL in DMSO) diluted in the McCoy's 5a or DMEM respectively. The dyes were well mixed into media and incubated for the appropriate time period described in Table 2.5, in a humidified incubator.

2.2.6.2 Preparation of live cells for imaging

The dye-media solution was carefully removed, and the cells washed twice in PBS warmed to 37 °C. FluoroBrite media (2ml; ThermoFisher Scientific, A1896701) was supplemented with 10% FBS, 10 µg ml^{-1} penicillin, 100 µg ml^{-1} streptomycin (ThermoFisher Scientific, 15410) and 2 mM Glutamax (Gibco, 35050-038). Cells were imaged using a Zeiss LSM 880 Inverted Live-cell Laser Scanning Confocal Microscope. Time-lapse images were taken using 50 cycles, and the images processed using an airyscan detector.

2.2.7 Image analysis

2.2.7.1 *Object Measurements*

Object diameter was measured in ImageJ by drawing a line across the widest section of the object and using the measure tool to obtain a calibrated measurement in microns. To obtain an average object diameter for a cell, a minimum of 10 examples of the objects were randomly selected and measured and a geometric mean obtained to represent the cell.

2.2.7.2 *Colocalisation Analysis*

Prior to colocalisation analysis, RGB images were converted to 8-bit, and split into component channels. Regions of interest (ROIs) were identified by drawing a line around the stained cell. The Fiji plugin Coloc 2 was used to perform Coste's regression to generate a 2D intensity histogram, calculate a Person's coefficient and Mander's coefficient, and perform Coste's significance test between the red and green channels of interest.

2.2.7.3 *Lysosomal movement analysis and counting*

2.2.7.3.1 TrackMate

Prior to measuring lysosomal velocity on time-lapse images, thresholding in ImageJ was performed to obtain a black/white image with little background signal. From thresholded images, a maximum intensity projection was generated using the ImageJ hyper stacks plugin to show range of lysosome movement. The plugin TrackMate was used to provide quantitative data for mean speed, displacement and location in X and Y of lysosomes (Tinevez et al., 2017). TrackMate software was calibrated using Zeiss image metadata. Lysosomes were detected using the LoG detector: a blob diameter of 0.2 μm was chosen based on an average measurement of lysosomes across a number of images. The number of total tracks followed is dependent on how many lysosomes were detected in each image and was used as an estimation of lysosome number. A simple LAP detector was used to track the lysosome movement. Maximum linking distance and gap linking distance were set to 1 micron based on the frame rate of the image, as was frame closing distance. From the associated analysis data and the number of frames a lysosome was in,

the average velocity of the track and the track displacement could be calculated. From this the average for the cell could then be derived.

2.2.7.3.2 3D Object mapping

Prior to 3D object mapping, RGB images were converted to 8-bit, thresholded, and split into component channels. The channel of interest was kept, and all others closed. Regions of interest (ROIs) were selected around cells of interest. Under the analyse tab, '3D Object Counter' was selected and the thresholding checked to make sure objects of interest were coloured red, therefore included in the analysis. Minimum size was set to 0.2 µm to remove background. Maximum size was set to 10 µm to include any abnormally large objects located within the channel. Exclude objects on edges was ticked, and maps for centre of mass (location) and surfaces were selected and then generated.

2.2.8 Statistical Analysis

All error bars show standard deviation around the mean unless stated otherwise. All data was checked to be normally distributed before statistical analysis carried out, and the tests chosen as appropriate. Student's t-test was carried out on averaged data where specified, using GraphPad Prism. Number of tails and paired/non-paired tests were selected as applicable. When data was not normally distributed, a Kruskal-Wallis non-parametric test was performed. Two-way ANOVA with GraphPad Prism was conducted on cell viability data, with a subsequent Bonferroni post-hoc test used to test statistical significance between conditions.

3 CHARACTERISING THE ENDOGENOUS EXPRESSION AND LOCATION OF PDI AND COLLAGEN IN EPITHELIAL AND OSTEOBLAST CELL LINES.

Introduction:

Initially it was important to validate and confirm the expression of endogenous PDI and collagen in BJ fibroblast, HT1080 and Saos-2 cell lines, alongside patient derived fibroblasts, as presented later. Since the majority of Cole Carpenter syndrome literature is clinical reports, the cell morphology and molecular basis of Cole Carpenter syndrome has not fully been investigated. This therefore required further research to characterise the biochemical and cell biological basis of the disease.

3.1. Endogenous PDI is expressed in the endoplasmic reticulum of the relevant cell lines.

PDI is an approximately 57 kDa protein ubiquitously expressed in all cell types of the body and localised to the ER. To be able to contextualise changes in PDI localisation in Cole Carpenter syndrome, the expression and localisation of endogenous wild-type PDI was confirmed in BJ fibroblast, HT1080 and Saos-2 cells, as displayed in Figure 3.1.

Figure 3.1A shows lysates of BJ fibroblast, HT1080s, Saos-2 analysed by SDS-PAGE and western blotted for PDI and its substrate collagen I. The relevant bands produced show PDI is expressed in the three cell lines at its expected 57 kDa molecular weight. Collagen I is expressed in BJ fibroblasts and Saos-2, appearing as a double band of the two α1(I) and one α2(I) chains which make up the collagen I triple helix, as previously described Section 1.2.2 and 1.3.3 (Makareeva, 2008). Since HT1080s are not professional collagen producing cells, collagen I expression in this work is limited to BJ fibroblasts and Saos-2 osteoblasts. However, the ER morphology and protein folding environment in HT1080s has been well characterised in the literature, hence their use as a model cell line for ER protein folding in both the literature and work in this thesis (Lobito, 2006; Chiu, 2015).
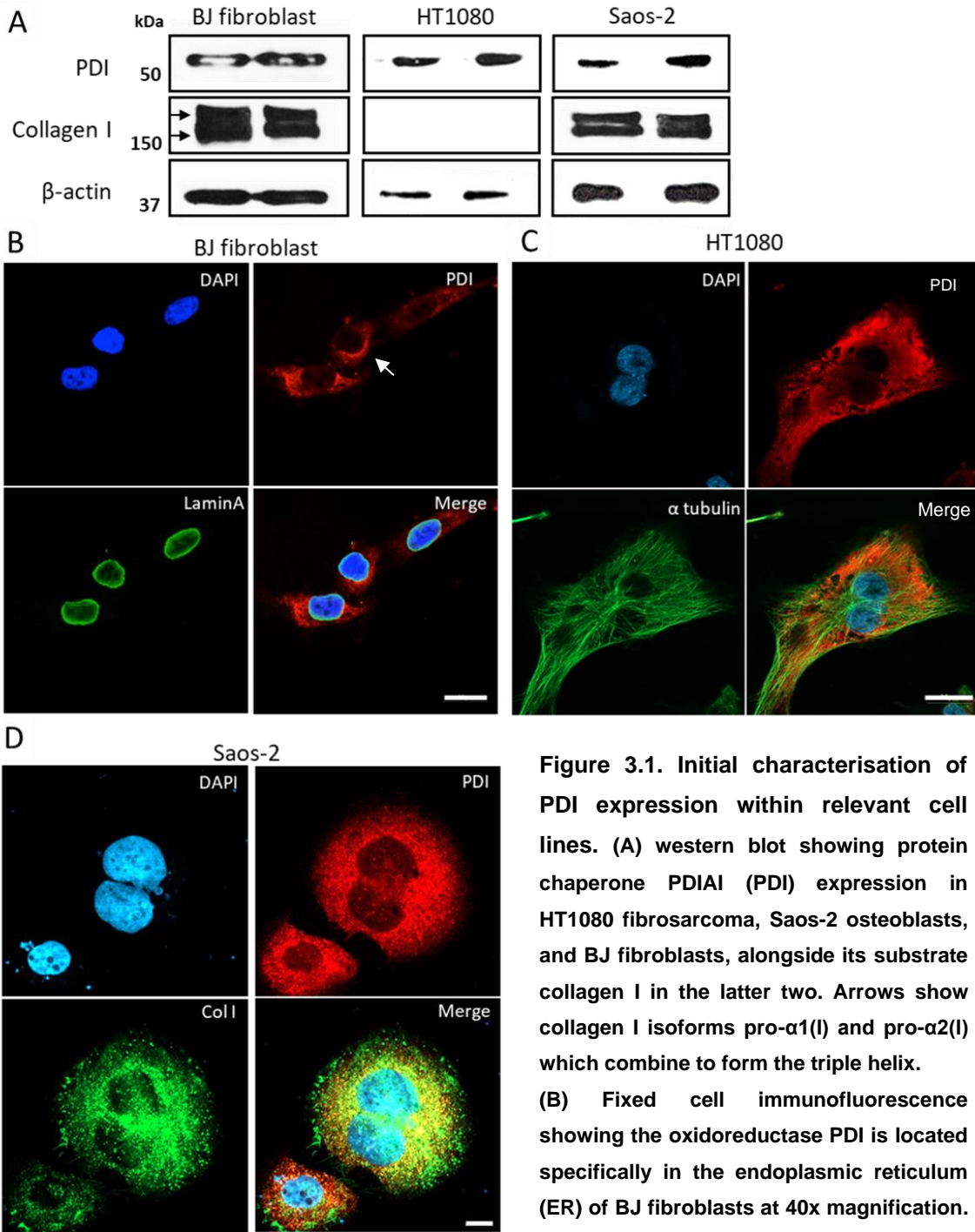
Figure 3.1. Initial characterisation of PDI expression within relevant cell lines. (A) western blot showing protein chaperone PDIAI (PDI) expression in HT1080 fibrosarcoma, Saos-2 osteoblasts, and BJ fibroblasts, alongside its substrate collagen I in the latter two. Arrows show collagen I isoforms pro-α1(I) and pro-α2(I) which combine to form the triple helix.

(B) Fixed cell immunofluorescence showing the oxidoreductase PDI is located specifically in the endoplasmic reticulum (ER) of BJ fibroblasts at 40x magnification. **(C)** HT1080 fibrosarcoma and **(D)** Saos-2 osteoblasts at 63x times magnification. PDI costained alongside Lamin A, α tubulin, and collagen respectively for context. Scale bars = 20μm.

40

To examine the intracellular localisation of PDI in the chosen cell lines, cells were fixed, permeabilised and prepared for immunofluorescence. Figure 3.1B shows PDI localisation in BJ fibroblasts, which appears conducive with the relevant literature. It is well established that PDI is localised to the rough endoplasmic reticulum (rER) (Ko, Kay, 2001; Bottomley, 2001). It is also widely used alongside its electron donor Ero1 α as a general ER marker in a wide variety of cell types (Nguyen, 2011; Baumann, 2016). This is reflected in Figure 3.1B revealing a characteristic ER shape and morphology across multiple cells when co-stained alongside lamin A, a nuclear envelope protein. The nuclear membrane is known to be continuous with the ER, a characteristic which appears reflected by the uninterrupted green (488) and red (594) signal arrowed (Mattaj, 2004).

To examine the relationship between PDI in the ER and the microtubule cytoskeleton, HT1080 cells were fixed and co-stained with PDI and α tubulin. These cells were inspected at 63x magnification, showing a mixture of sheet and tubular ER morphology. Generally, the sheet-like ER is known to be found towards the perinuclear region, and the tubular structures towards the periphery of the cell (Blackstone, 2016) which is reflected in Figure 3.1C and Figure 3.2. These ER tubules appear separate to the microtubule cytoskeleton.

Saos-2 cells were fixed and stained for PDI and collagen I to assess the location of these proteins in a bone-forming cell line. PDI is also ER localised in these osteoblasts as expected alongside collagen I. However, these osteoblasts show a somewhat different PDI distribution than HT1080 cells. PDI appears to be more punctate and disperse, without the tubule structures seen in the HT1080 cells (Figure 3.1D).

3.2. The ER can have disperse and tubular networks.

As observed in Figure 3.1, the morphology of the ER may vary between cell types. It can take on at least two different morphologies which depend on the redox environment of its lumen, and the wider cell homeostasis (Lee, 2020). These can consist of a dense 'sheet-like' layer, usually in the perinuclear region, and a highly developed tubular network, which usually predominates the periphery of the organelle, closer to the Golgi apparatus and the cell membrane (Blackstone, 2016). This is shown in Figure 3.2A in the magnified panels (i) and (ii) which display the tubular and sheet-like ER respectively.

41
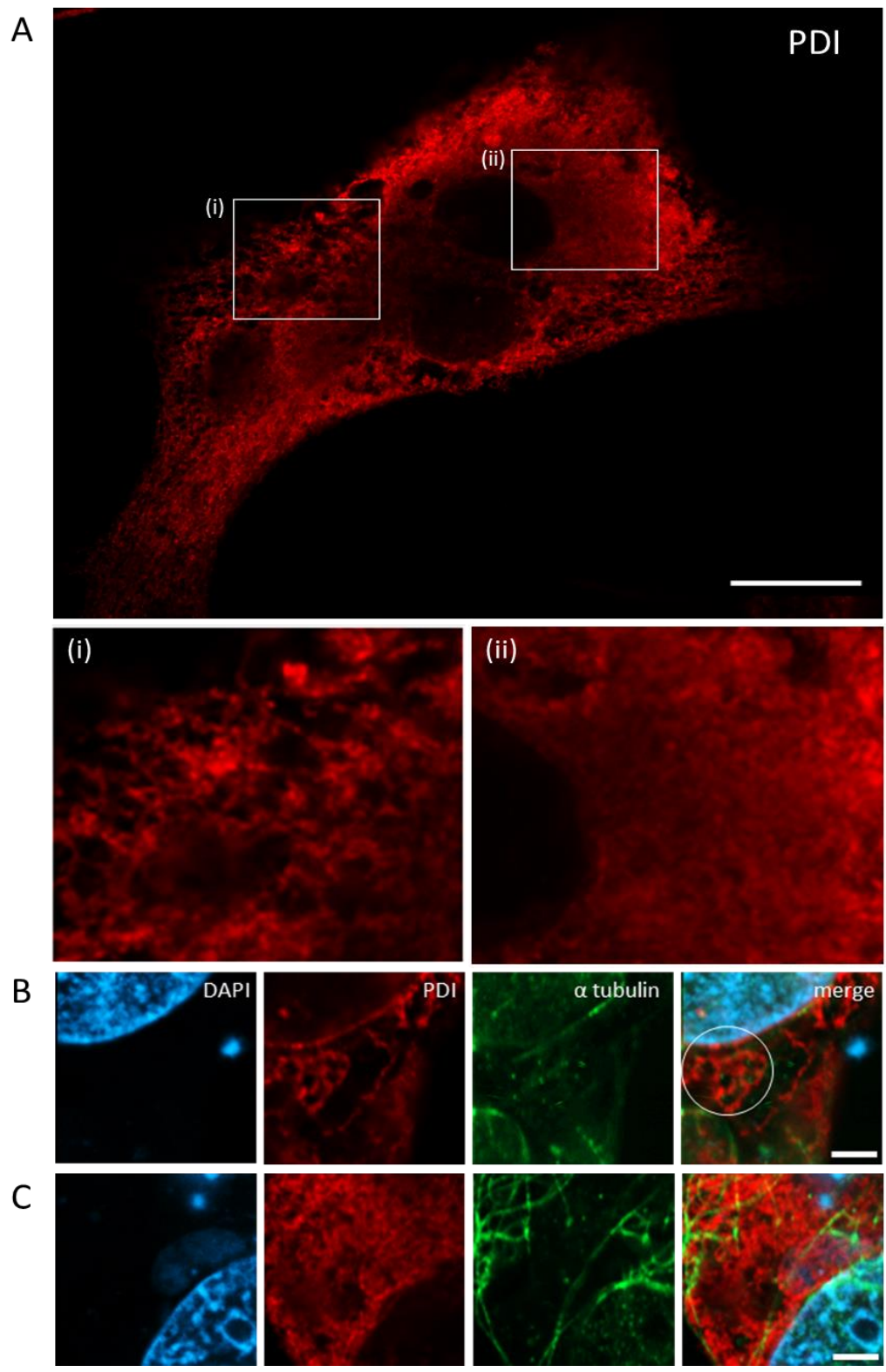
Figure 3.2. The tubule and 'sheet-like' ER morphologies as observed in HT1080 cells.
(A) The perinuclear ER 'sheet' (i) and the peripheral tubular network (ii) from HT1080
red (594) channel in Figure 3.1B. Scale bar = 20 μm. (B) ER tubules in the perinuclear
region form a dense tubule network (circled). (C) The disperse 'sheet-like' ER with
fewer evidence of ultrastructure. The microtubule cytoskeleton does not colocalise
with these tubules. Scale bar = 5 μm.

42

HT1080 cells were fixed and prepared for immunofluorescence by co-staining PDI with α tubulin, as shown in Figure 3.2B and 3.2C. This was to establish if these ER structures are dependent on other tubule structures of the cell such as the microtubule cytoskeleton, since this network is known to interact with the ER on many interdependent levels, including the extension of ER tubules along microtubule filaments (Terasaki, 1986; Waterman-Storer, 1998; Brandizzi, 2003). Both Figure 3.2B and 3.2C show that these ER tubules are distinct ER morphologies and unaffected by the microtubule cytoskeleton of the cell.

Interestingly, Figure 3.2B also illustrates that the perinuclear region containing the rER has also developed these tubules, which is generally thought to be sheet-like, as shown in the same cell in 3.2C. This data illustrates the general morphology of the ER at high magnification, illustrating the variety of forms observed within and between these cells.

3.3. Conclusion

The experiments in this section have characterised the existence and subcellular location of key proteins in the cell lines chosen for this work, and demonstrated that the ER is a highly dynamic organelle. The chaperone activity of PDI and the folding of the collagen I triple helix occurs in the ER lumen, and the conditions at which this occurs are likely to be vastly dependant on the morphologies of the ER and other ultra-structures of the cell, hence this relevance to CCS. The tubular and sheet conformations of the ER observed in this chapter broadly relate to the roles of the ribosome associated rER, which is traditionally more sheet-like (Shibata, 2006). However, as observed in this chapter, the PDI associated rER can also demonstrate a tubular conformation, which is shown to be distinct from the microtubule cytoskeleton. Due to the importance of the microtubule network in vesicle trafficking from the ER and post-golgi apparatus (Fourriere, 2020), this was deemed necessary to characterise in cells expressing PDI with the Cole Carpenter mutation. Furthermore, a microtubule dependant region of the ER has proven important in ER protein folding quality control (Smith, 2011). Since Cole Carpenter syndrome has been hypothesised to be a result of dysfunctional ER quality control, this branch of the cytoskeleton was considered an area of interest for this project.

Lee (2020) recently been noted that a tubular ER is found in areas of the cell where the production and fission of ribonucleoprotein granules and stress granules occurs

43

which indicate the attenuation of translation and therefore cell stress responses. Therefore, the proportions of these ER morphologies in the cell, notably an increase in a tubular ER, may indicate the presence and progression of one or more pathways of the ER stress response, an identifying factor of CCS1.

4. ASSESSING THE EFFECTS OF CYS393 ON THE POSSIBLE INTERACTING PARTNERS OF Y393C-PDI.

Introduction:

It has been hypothesised that the molecular cause of CCS1 relates to the formation of unconventional intermolecular disulphide bonds by Y393C-PDI. These could impact binding of PDI to the pro-alpha1(I) and pro-alpha2(I) chains which make up Collagen I, alongside a failure to interact with P4HA to form the prolyl-4-hydroxylase complex (P4H). Y393C could also interfere with PDI's disulphide isomerase activity, resulting in mis-oxidation of its relevant substrate, therefore influencing PDI interacting partners (Balasubramanian, 2016). Determining which roles of PDI are compromised by this mutation is vital and could shed light on the complexity of both PDI as a multifunctional protein, alongside the downstream effects on cellular homeostasis.

4.1. Designing and generating wild-type and Y393C-PDI plasmid constructs

To replicate the cellular Cole Carpenter phenotype and provide the necessary controls, two plasmid constructs shown in Figure 4.1, were designed to be transiently transfected into established cell lines. These contain open reading frames (ORFs) for Y393C-PDI and wild-type PDI both tagged with a short -myc sequence (N-EQKLISEEDL-C) before the ER localisation sequence (KDEL) to enable the protein to be retained in the ER. Both ORFs are driven by a constitutively active human cytomegalovirus (CMV) promoter to induce stable and high expression levels of the relevant PDI. This allows the transfected protein to be detected by antibodies raised against -myc tag and therefore differentiated from endogenously expressed PDI. Both constructs contain ampicillin resistance for bacterial selection and the isolation of new DNA. The WT-PDI-myc construct contains Neomycin resistance for mammalian selection to allow future stable transfection of cell lines.
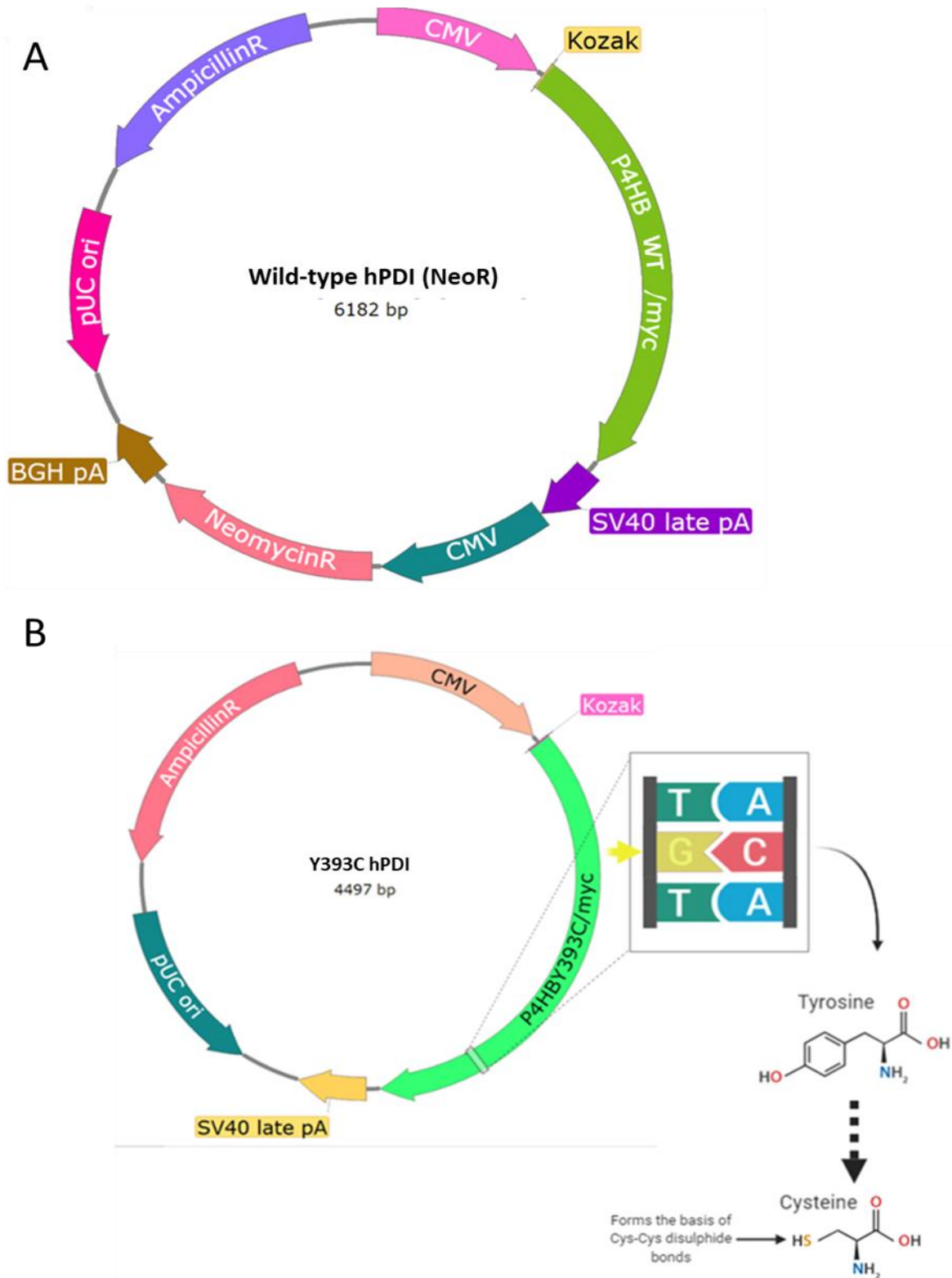
Figure 4.1. Plasmid maps for DNA constructs as used in this thesis. Both plasmid ORFs are driven under a constitutive Human cytomegalovirus (CMV) immediate early enhancer/promoter. Both have *E. Coli* bacterial resistance for plasmid amplification. (A) WT-PDI-myc construct is used as a positive control, and also contains Neomycin resistance (NeomycinR) as mammalian selection resistance. (B) Y393C-PDI-myc replicates the CCS1 mutation (1178A>G), replacing the conventional Tyr393 with the smaller, reactive cysteine residue in the a' domain of PDI.

4.2. The 3D crystallographic structure of Y393C-PDI shows the location of Cys393 close to the active site.

To determine the effects of the Y393C mutation on the binding capacity of PDI, the mutation and catalytically active site was mapped onto the known X-ray crystallographic structure of the protein. The schematic shown in Figure 4.2A shows human PDI has four subdomains each containing thioredoxin folds, contributing to both its activation and roles as a subunit of higher, quaternary structure complexes. The two catalytically active outer a and a' subdomains are shown in red, and the two inner, and non-catalytically active subdomains (b and b') are shown in blue. It has been suggested that the gain of cysteine mutation in Y393C-PDI may impact the catalytic domains of PDI, and formation of these higher order protein complexes.

The tertiary structure of the complete abb'a' subdomains of human PDI has been solved at a resolution of 2.51 Å (Wang, 2013). This is reproduced in Figure 4.2B showing the individual subdomains of the protein, and the location of the catalytically active site within the a' subdomain. This site resides between reactive residues Cys397 and Cys400, and is further magnified in C to show the proximal location of the Y393C mutation to this catalytically active region. It has been hypothesised that this gain of a reactive cysteine (Cys393) results in displacement of this active site, or an interruption of its function. Figure 4.1C suggests this is likely, as the gained cysteine residue at 393 appears solvent exposed, shown by marked water molecules, and therefore available for disulphide bond interactions. This may result

in abnormal activity of PDI, and perhaps incorrect binding of PDI to other proteins within the cell, alongside the C-P4H complex and its substrate collagen.

Figure 4.2. The catalytic a' subdomain is affected by the Tyr393Cys mutation of CCS1 PDI. (A) subdomains of human PDI including their catalytic status (active, red; inactive, blue). **(B)** X-ray crystallographic structure of human PDI showing each domain as an alpha helix and beta sheet model. Catalytic active site of C397 and C400 (red) is shown alongside Y393C mutation as a ball and stick residue (blue). **(C)** The active site and mutation region are further magnified. Water molecules shown as red specks show solvent accessibility.

4.3. Unconventional Y393C-PDI complexes are retained on non-reducing SDS-PAGE, and further trapped by N-Ethylmaleimide in HT1080 cells.

To investigate whether Y393C-PDI does interact with unconventional binding partners, HT1080 lysates were transfected with either wild-type (WT) Ero1α-myc as a positive control or the Y393C-PDI-myc plasmid construct shown in Figure 4.1. Non-nuclear proteins in each lysate were separated using reducing and non-reducing SDS-PAGE then transferred to a PVDF membrane and western blotted for α-myc. The results of this are shown in Figure 4.3, showing a wide range of protein complexes retained in Y393C-PDI transfected lysates. This provides the experimental basis to further identify any Y393C-PDI interactions with unknown or unconventional proteins in the cell compared to the well characterised complexes formed by Ero1 α.
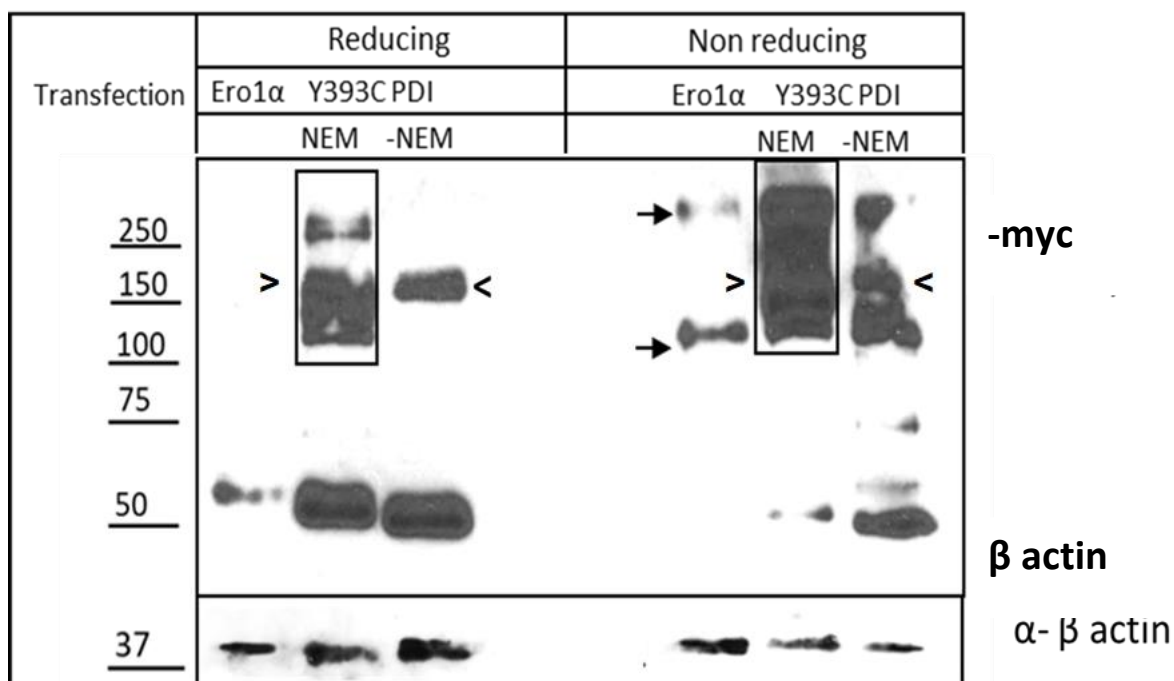
Figure 4.3. Unconventionally stable, high molecular weight complexes are retained in lysates of HT1080 cells transfected with Y393C-PDI-myc and treated +/- NEM before lysis. Ero1α-myc transfected lysate is included as a positive control. All lysates were subjected to separation by reducing and non-reducing SDS-PAGE and probed for α-myc. 10 µg of total protein was added to each well, as shown by loading control (β-actin).

As some PDI interactions are disulphide dependant, intermolecular disulphides were first trapped by N-ethylmaleimide (NEM), an alkylating agent modifying cellular free thiols. Separation by SDS-PAGE was carried out under reducing and non-reducing conditions for both sets of lysates, with the latter condition used to preserve disulphide bonds. The addition or omission of the reducing agent Dithiothreitol (DDT) was used to achieve this, and to establish whether Y393C-PDI could be found in higher order structures or protein complexes. The successful reduction of Ero1 α into its 60 kDa monomeric form proves DTT is functioning as expected, therefore the variety of complexes shown are likely not a result of oxidised, and thus non-functional DTT.

Some unconventional PDI complexes of Y393C-PDI appear to be NEM dependant, depicted in Figure 4.3, boxed. NEM treated lysates separated under non-reducing conditions result in the largest number of complexes retained between 120 kDa and > 250 kDa, as expected from the disulphide bond protective measures taken. A comparison between Y393C-PDI transfected lysates shows a band of the same size (150 kDa) retained seemingly in all conditions (< and >) although this is inconclusive in unreduced and NEM treated lysates due to the large numbers of retained complexes. Nonetheless, the consistent retention of this complex suggests this is both NEM independent, and unable to be reduced by normal concentrations (100 mM) of reducing agent. This infers unconventional stability and provides initial evidence that Y393C-PDI may form abnormal higher order complexes in the cell.

4.4. Western blot analysis of PDI complexes in Saos-2 osteoblast-like cells.

To further examine the nature of these retained Y393C-PDI complexes, and whether they are replicated in osteoblasts, lysates of Saos-2 cells were prepared using the same experimental procedure as shown previously in Figure 4.3. This experiment revealed less retention of PDI complexes overall, however the approximately 150 kDa stable Y393C-PDI complex is also found in these osteoblast lysates, mirroring that observed in HT1080s. There also appears to be similar NEM and DTT dependant retention patterns as those in Figure 4.3, with the most complexes retained in the samples treated with the crosslinker NEM, and without DDT reduction retaining the most complexes (boxed). Lysates ran under non-reducing conditions display the characteristic 'blurry' bands, as expected from the literature (Marangon, 2014).
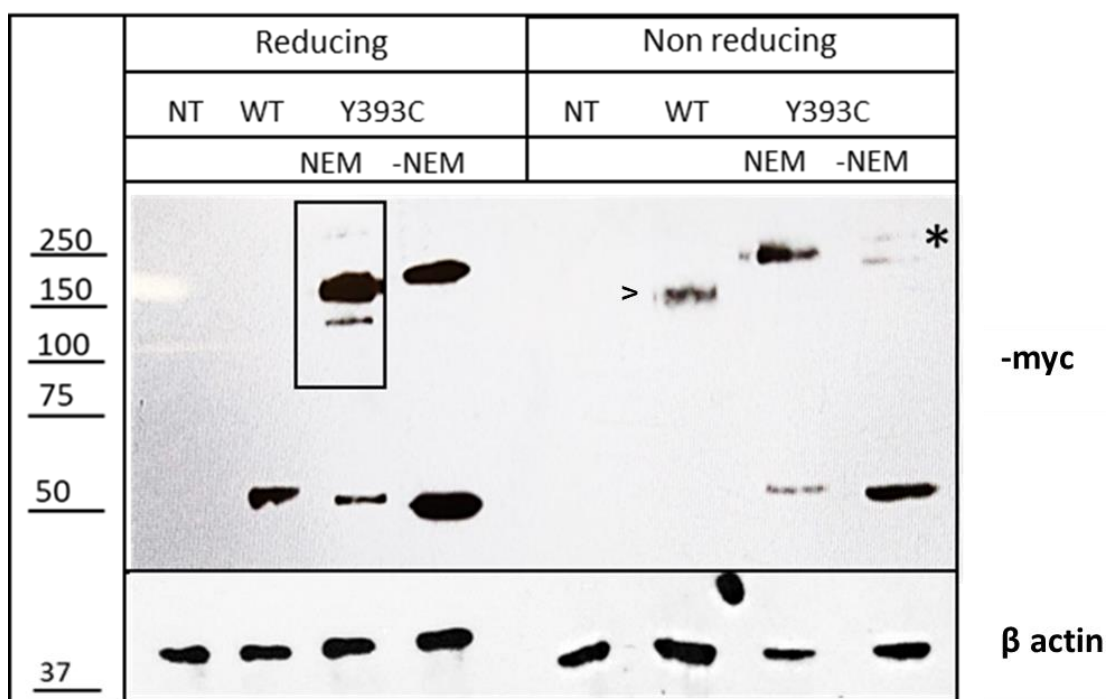
Figure 4.4. 150 kDa Y393C-PDI complex found in Y393C-PDI-myc transfected HT1080 fibrosarcoma is observed in Saos-2 osteoblasts. Non-transfected (NT), WT-PDI-myc (positive control) and Y393C-PDI-myc transfected lysates were subjected to SDS-PAGE under reducing and non-reducing conditions. 10 μg of total protein was added to each well, and a separate Y393C-PDI sample was prepared with lysate treated with N-Ethylmaleimide (NEM), as previously. These were probed with α-myc, and β-actin as a loading control.

The right-hand lane marked (*) highlights that the two high molecular weight bands observed in Y393C-PDI lysates are affected by the addition of the NEM crosslinker, as they are not replicated in the corresponding condition. Instead, are replaced by a single complex at 150 kDa. Furthermore, the existence of this large complex in both reducing and non-reducing conditions infers it is 'reduction resistant'. The Y393C PDI band observed under reducing conditions is also retained at a slightly higher molecular weight without NEM treatment, as shown by +/- NEM comparison. These observations are generally concurrent with those of the Y393C-PDI-myc transfected fibroblast cell line in the previous figure.

Figure 4.4 also shows that these high molecular weight interactions retained in Y393C transfected cells are not present in cells transfected with a WT-PDI-myc construct. Lysates transfected with wild-type PDI and analysed under reducing conditions produced a single band of the monomeric form (57 kDa) of PDI. When under non-reducing conditions, a single band of wild-type PDI at approximately 150 kDa is observed (>). This is reflective of that observed in Y393C-PDI lysates, however crucially in wild-type PDI transfected cells, this complex is successfully reduced by DTT. This is shown by its absence from the corresponding WT reducing lane, a characteristic is not observed by the Y393C-PDI complex. This suggests its resistance to reduction by DTT is unique to Y393C-PDI, not its molecular weight of the complex. Therefore, it is likely this interaction reflects a conventional binding partner for PDI, which is acting unconventionally. This high molecular weight complex is seen previously in HT1080 lysates, again showing this complex is present in both osteoblast and fibroblast cell lines.

This experiment confirms no α-myc signal in the non-transfected cells (NT), showing antibody specificity to transfected protein only. This further affirms that the bands shown above are true interactions of Y393C-PDI with other proteins or complexes, as a result of the CCS1 mutation as opposed to the impact of transfection and antibody variability.

4.5. Dithiothreitol titration shows the presence of stable, DDT dependant Y393C-PDI complexes in HT1080 and Saos-2 cells

The previous two experiments in HT1080 and Saos-2 transfected lysates suggested unconventional, high molecular weight complexes containing Y393C-PDI may show increased resistance to reducing agents. An experiment was devised to establish whether complex retention can be prevented with increased concentrations of reducing agent, and at what level the disulphide bonds within these complexes are broken down. The results of this are shown in Figure 4.5. The cells were not treated with NEM before lysis to prevent additional disulphide crosslinking, and DTT concentrations of 50 mM, 100 mM and 150 mM were added to samples before loading, to cause proportionally increasing reduction of disulphide bonds.
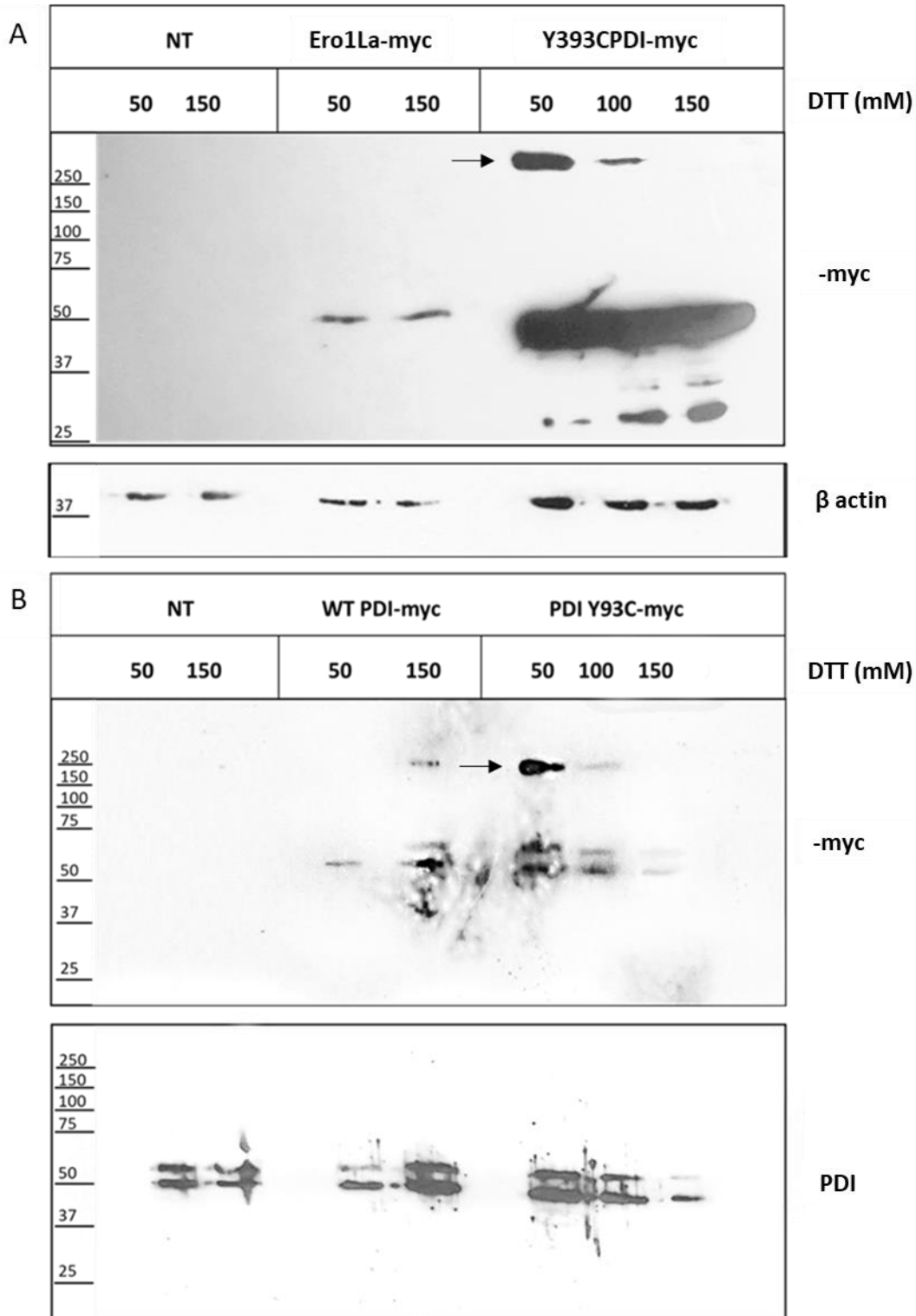
Figure 4.5. Proportionally increasing DTT concentrations eventually disrupt the Y393C-PDI complex. Western blotting for (A) HT1080 lysates and (B) Saos-2 lysates transfected as previously described, all without NEM treatment, and subjected to separation by SDS-PAGE. DTT concentrations of 50 – 150 mM were added to each condition before gel electrophoresis; negative and positive control wild-type PDI lysates prepared with 50 and 150 mM, and Y393C-PDI with 50, 100, 150mM. β actin loading controls included.

Consistent with previous findings, Y393C-PDI complexes retained in HT1080 cells appear larger than those in Saos-2, appearing at > 250 kDa and approximately 200 – 250 kDa respectively. In both cell types, when lysates are treated with 50 mM concentrations of DTT, the disulphide bonds of the large Y393C-PDI complex are not reduced, as expected by this lower concentration (arrowed). This complex also remains intact under 100 mM of DTT, despite this being the standard molar usage of this reducing agent to fully reduce disulphide bonds. Under 150 mM of DTT there is sufficient disulphide bond reduction, with no large molecular weight band appearing. This therefore shows breakdown of these complexes is achievable at a much higher concentration of DTT than is conventional. No such interactions are seen when the membrane was re-probed for α -PDI.

4.6. Immunoprecipitation pulldown of endogenous and transfected PDI shows atypical, high molecular weight interactions of Y393C-PDI in both HT1080 and Saos-2 cells.

To further elucidate Y393C-PDI's potential interacting partners, immunoprecipitation pulldowns of α-PDI on non-transfected, WT-PDI-myc and Y393C-PDI-myc Saos-2 lysates were prepared for western blotting. Y393C-PDI-myc transfected cells were treated with and without NEM during lysis, to replicate the increased complex retention as previously observed. Figure 4.6A (left) shows HT1080 lysates without immunoprecipitation western blotted for α-PDI. The right-hand lanes show WT-PDI-myc and Y393C-PDI-myc immunoprecipitated with polyclonal α-PDI and western blotted for α-myc to identify transfected PDI interactions only. Multiple interactions are seen in both conditions, including high molecular weight complexes, particularly at 150 - 250 kDa, as alluded to in the previous figures. The lower band observed at 35 – 40 kDa in the immunoprecipitation pulldowns blotted for -myc may be a result of non-specific binding, or a cleaved breakdown product of the construct including the -myc tag. This band does not appear in the following Saos-2 lysates suggesting this interaction is irrelevant to the basis of Cole Carpenter syndrome.
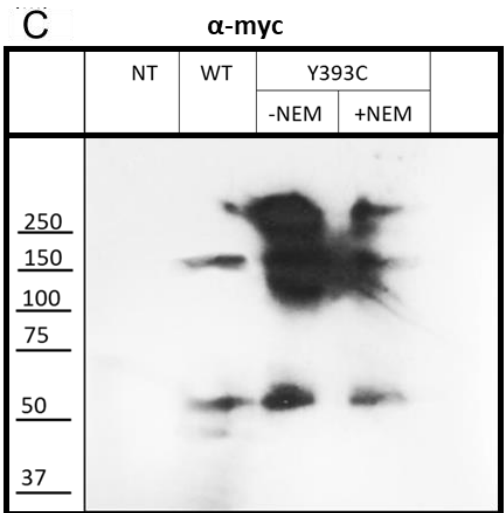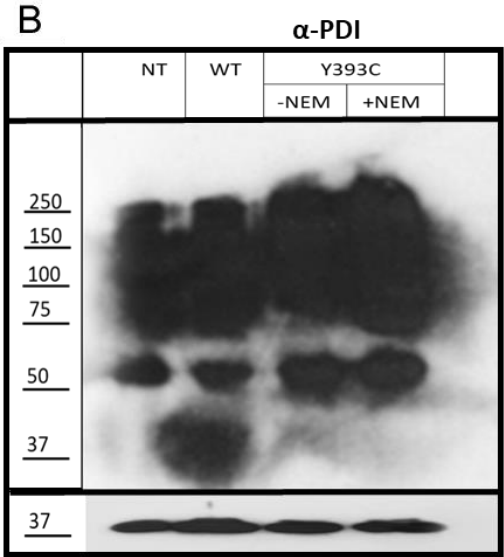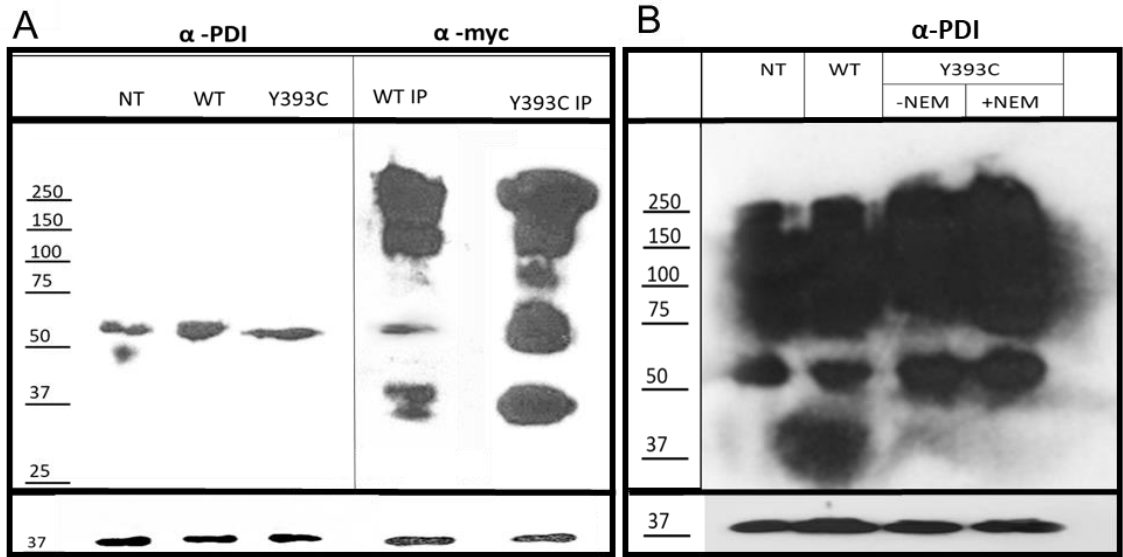
Figure 4.6. Immunoprecipitation (IP) pulldowns of α-PDI show increased complex retention when blotted for both α-PDI and α-myc. (A) WT-PDI-myc and Y393C-PDI-myc transfected HT1080 lysates were separated by SDS-PAGE. Non immunoprecipitated lysates are shown on left. These were blotted for using α-PDI and immunoprecipitated lysates for α-myc (right). β actin loading controls shown below. (B, C) Immunoprecipitations were repeated in Saos-2 transfected lysates. Y393C-PDI transfected cells were treated +/- NEM before lysis. The membrane was probed for α-PDI (B), and re-probed for α-myc (C). β actin loading controls shown below panel B. Exposure time: 2 seconds.

57

These high molecular weight complexes are further observed in the same experiment repeated in Saos-2 non-transfected and WT-PDI-myc, Y393C-PDI-myc transfected cells, as shown in the right-hand panels. Figure 4.6B shows all PDI pulldown interactions across all conditions with no discernible bands, despite a short film exposure time of 2 seconds. It appears that treatment with NEM retains marginally more complexes due to more signal detection in the latter two lanes. This is verified by β actin loading controls confirming no differences in loaded protein for each condition. When these samples were probed for α-myc, thus removing endogenous PDI interactions, bands containing Y393C-PDI interactions became more discernible. Panel C shows Y393C-PDI appearing to interact uniquely with other proteins, forming the previously established high molecular weight complexes at 250 kDa. The other band at 150 kDa is also seen in WT-PDI-myc transfected condition may be that of PDI and its electron donor Ero1 α, which is well established as a conventional binding partner for PDI.

To elucidate the components of these PDI complexes, co-immunoprecipitation experiments for PDI were repeated with non-transfected, WT-PDI-myc and +/- NEM Y393C-PDI-myc transfected Saos-2 lysates. These were prepared for Liquid Chromatography-Mass spectrometry (LC-MS) using a trypsin digestion protocol. The digested peptides retained by co-immunoprecipitation were searched for against a human reference proteome. Known proteomic experiment contaminants were also searched for using PEAKS X+, and a filter of 2 unique peptides was added to the samples. After known and possible contaminant exclusion, a total of 4, 3 and 8 heat shock proteins were pulled down in the co-immunoprecipitation for non-transfected, WT-PDI-myc and Y393C-PDI-myc transfected lysates respectively. These are included in Table 4.1.

Table 4.1. List of proteins of interest (POIs) pulled down in LC-MS analysis of non-transfected (NT), WT-PDI-myc transfected and Y393C-PDI-myc transfected Saos-2 containing average recorded mass, and number of peptide hits for each protein. N/A = protein undetected in relevant sample.

Protein of Interest (POI)	Average mass (kDa)	Number of peptides		
		NT	WT-PDI-myc	Y393C-PDI-myc
HSP90AA2 (*)	39365	3	2	12
HSP90AA1 (*)	84660	3	2	12
HSP90AB1 (*)	83264	3	2	17
HSP90AB2P	44349	3	N/A	N/A

HSPA4	94331	N/A	N/A	*2*
HSPH1	96865	N/A	N/A	*2*
HSPB1	22783	N/A	N/A	*5*
HSPA1A	70052	N/A	N/A	*11*
HSPA1B	70052	N/A	N/A	*11*
HSPA8 (**)	70898	N/A	N/A	*16*

In general, there are more proteins of interest pulled down by anti-PDI in Y393C-PDI-myc transfected cells than their wildtype transfected and non-transfected counterparts. When non-human protein contaminants were removed, these appear to be heat shock proteins (HSPs) which are well known to be upregulated during cellular and ER stress responses (Samali, 1998; Liu, 2008). The top three proteins shown in Table 4.1 (*) are members of the cytoplasmic HSP90 family and peptides corresponding to these proteins are found in each sample, suggesting their presence is not Y393C-PDI dependant.

There is Y393C-PDI specific retention of cytoplasmic HSP70 family proteins which are known protein chaperones and apoptosis mediators, shown in the right-hand column. These are HSPA1A and HSPA1B which are retained in Y393C-PDI cells only, with relatively high peptide counts of 11. HSPH1 and HSPA4 which act as nucleotide exchange factors (NEFs) for HSP70 family members (Rauch, 2014) are also pulled down alongside them, alongside small heat shock protein 1 (HSPB1). These have much lower peptide counts of 2, 2 and 5 respectively.

There also appears to be a relatively high retention of HSPA8/heat shock cognate protein 70 (Hsc70) complexed with PDI in Y393C-PDI expressing cells. A total of 16 peptides was detected, which is the second highest recorded in the sample after HSP90AB1, and no retention of these complexes in the wildtype PDI expressing cells.

4.7. Conclusion

Since bone biopsies by Cole and Carpenter concluded the quantity of collagen produced in patient cells is unaffected (1987), it is assumed that any collagen quality control issue in CCS lies with the post translational modification of the collagen triple helix, in part coordinated by PDI. If PDI is performing or interacting unconventionally in the cell, this may result in the improper folding of collagen, resulting in the CCS1 phenotype.

59

Figure 4.2. displays the C terminal active site and its placement between Cys397 and Cys400 on the known 3D crystal structure of PDI, as expected from the literature (Bekendam, 2016; Santos, 2017). It also highlights the significance of this gain of reactive cysteine residue in its proximity to this active site, meaning the intracellular effects of this are open to speculation. One possibility is that this gain of a reactive cysteine results in different internal disulphide bond formation between the residues of PDI's active site, for example between Cys393 and Cys397. This may displace the bond between the conventional active site residues, and thus impair redox activity. Another possibility is that this Cys393 is solvent exposed, which may result in off-target interactions between PDI and other proteins. This is a likely possibility, as suggested by the proximal placement of water molecules on Figure 4.2B. These unconventional, disulphide dependant interactions could therefore contribute to an abnormally functioning or mislocalised Y393C-PDI.

Western blotting data shown in Figure 4.3 and 4.4 highlights the atypical high molecular weight complexes retained under reducing conditions. This supports the 'unconventional interactions' hypothesis of Y393C-PDI activity, as has been suggested by our clinical partner (Balasubramanian, 2018). The interactions hypothesised by Balasubramanian may be the 200 - 250 kDa complexes observed in the disulphide crosslinking and immunoprecipitation experiments in this thesis, which show Y393C-PDI complexes which appear to be unconventionally stable, with increased resistance to reduction. The usage of reducing agent DDT and alkylating agent NEM are suitable experimental conditions to assess the retention of disulphide dependant complexes, as the gain of a reactive cysteine near the enzyme's active site is hypothesised to contribute to the unconventional placement of disulphide bonds. Hence these complexes, if present, would be retained under DTT and NEM conditions.

These Y393C-PDI complexes appear to be partly resistant to reduction by DTT, shown by consistent high molecular weight bands in the experiments shown in this chapter. This is despite the effective reduction of both transfected Ero1 α and wild-type PDI complexes as positive controls, in HT1080s and Saos-2 cells respectively. This is also highlighted by the presence of a band at 150 kDa observed in Y393C-PDI-myc transfected lysates under reducing conditions, irrespective of NEM addition. This interaction was observed in both HT1080 and Saos-2 lysates and could pertain to PDI's known interactions with its electron donor Ero1 α at 150 kDa

60

(Appenzeller-Herzog, 2010). Conversely, this could potentially form part of the 228 kDa of the C-P4H complex, which is established to be the direct chaperone complex ensuring proper collagen folding (Gorres, 2011), and may explain some of the other bands observed. Whilst reducing conditions employed here effectively break up this complex in wild-type PDI expressing cells, these have little effect in Y393C conditions. The complexes formed by Y393C-PDI only slightly reduce to approximately 170 – 200 kDa in size, as observed in Figure 4.4. Therefore, the resilience of these complexes in the presence of reducing conditions could suggest abnormal behaviour of PDI in the context of the C-P4H complex or Ero1 α. These behaviours are likely a result of this Y393C-PDI mutation, due to no such retention observed in control lysates.

This result could be confirmed by performing the same experiment but replacing DTT with other reducing agents such as beta mercaptoethanol (BME) or tris(2-carboxyethyl)phosphine (TCEP) to establish if complex breakdown can be achieved by other reducing agents. TCEP is known to be a more powerful reducing agent than DTT, and can act over a range of pH, therefore may give a clearer indication of the disulphide stability of these complexes (Burns, 1991).

Since DDT can oxidise quickly at room temperature, positive control transfected lysates (WT-PDI-myc or wild-type Ero1α-myc) were also used to ensure successful reduction of the protein lysate. In Figure 4.3, the Ero1 α positive control lysates under reducing conditions show monomeric Ero1 α at 60 kDa, which is slightly larger than its endogenous 54 kDa size (Araki, 2013). This is not unexpected, as alongside the addition of -myc tag in this case, endogenous Ero1 α can be found at 60 – 62 kDa under reducing conditions (Kukita, 2015). However, in non-reducing conditions this is split into two larger fragments measuring approximately 120 kDa, and > 250 kDa respectively). This infers substrate/dimer complexes have been successfully retained; the 120 kDa band could pertain to a dimer of the two 60 kDa Ero1 α monomers and shows the successful reduction of disulphide bonds in DDT conditions.

This data suggests that Y393C-PDI interacts unconventionally to form large, high molecular weight complexes which are unconventionally stable and resistant to reduction by DDT. These are further trapped via crosslinking mediated by the alkylating agent NEM, and eventually broken down with 150 mM of DTT. Co-

immunoprecipitation experiments shown in Figure 4.6 are consistent with these findings. It is perhaps important to note that the endogenous PDI pulldowns and subsequent blotting were performed with a polyclonal PDI antibody, as shown in Table 2.1, which may have led to the high cross reactivity observed in Figure 4.5B. There does appear to be more complexes retained at higher molecular weights in the Y393C-PDI transfected lysates, despite individual complexes indistinguishable. When the membrane is probed for anti-myc, these appear to be reproduced, showing the same > 250 kDa interactions in the Y393C-PDI lysates.

To determine the nature of protein components in these interactions, LC-MS was performed on the co-immunoprecipitation experiments shown in Figure 4.6. Due to the co-immunoprecipitation antibody pulldown method used, many of the proteins retained were deemed contaminants and omitted. Those that appeared to show relevant and significant interactions were displayed in Table 4.1. There appeared a marked increase in heat shock protein (HSP) retention from both HSP70 and HSP90 protein families, both of which are localised to the cytoplasm but can be found in the ER (Mayer, 2005). Many of these proteins have essential functions in proteostasis and apoptosis, one of which is HSPA1A/HSP72 (Rauch, 2014). 11 individual peptides of HSP72 were retained in complex with PDI in Y393C-PDI expressing cells, alongside none in both wildtype PDI controls. Like PDI, this 70 kDa protein acts as a molecular chaperone, and facilitates the proper folding of newly translated and misfolded proteins, as well as stabilising or degrading mutant proteins. If the Y393C-PDI previously observed complexes contains trapped HSP72, this may cause the onset of proteotoxicity and ER stress, possibly as a result of misfolded protein aggregation hypothesised in this thesis.

Interestingly, HSPA8/heat shock cognate protein 70 (Hsc70) is a molecular chaperone known to interact with cytosolic proteins destined for lysosomal degradation via chaperone-mediated autophagy. It was retained with a high proportion of peptides in Y393C-PDI cells (16), however not in wildtype PDI expressing cells. When functioning properly, a protein complex of Hsc70 and misfolded/unfolded proteins is recognized by lysosomal-associated membrane protein 2 (LAMP2), which results in the translocation of the unfolded protein into the lysosome for degradation (Cacciottolo, 2013; Kabuta, 2008). However, the trapping of Hsc70 in complex with Y393C-PDI may prevent this activity, therefore have

downstream effects on lysosome mediated autophagy and the wider proteostasis of the cell.

On the other hand, there is an absence of known PDI interacting proteins in all samples, such as Ero1α and the rest of the C-P4H complex. These may not have been retained with a peptide False Discovery rate (FDR) of 1%, which was deemed necessary to remove cytoskeletal contamination in the sample. Furthermore, cytosolic HSPs are known to be inherently sticky, therefore there is a possibility the peptides were retained as non-specific pulldowns, rather than PDI specific complexes formed. Further repeats of this experiment to minimise contamination are suggested to confirm these results. Despite this, the large increases in peptide retention of proteostasis-regulating HSPs in Y393C-PDI expressing cells may infer there is general upregulation of these proteins in Cole Carpenter cells. This may suggest the onset of ER stress or attempts to activate the UPR to rescue the misfolded protein, or direct it for lysosome mediated autophagy (Dice, 2007).

5. CHARACTERISING THE INTRACELLULAR LOCALISATION AND EFFECTS OF Y393C-PDI

Introduction:

After identifying possible interacting partners for Y393C-PDI, it was important to characterise the subcellular location and the potential impacts of Y393C-PDI on the ER and other organelles. This could shed light on the causes of the CCS phenotype, especially due to the variety of symptoms displayed by the patients, which may pertain to PDI's multifunctional roles in the ER. If misfolded collagen aggregates are retained within the ER, it may result in excess pressure on ER associated proteolysis or lysosome-mediated autophagy within the cell. As previously mentioned, the microtubule network is essential for vesicular collagen transport and exocytosis (Marchi, 1984; Canty, 2005). It also plays vital roles in lysosomal motility, ER morphology and quality control, alongside cellular structural integrity (Matteoni, 1987; Waterman-Storer, 1998). Downstream effects on both lysosomal and cytoskeletal systems due to improper activity of PDI may again contribute to the phenotypes observed in CCS1.

5.1. Y393C and WT PDI generally colocalise in the ER in HT1080 and Saos-2 cells

Alongside producing transfected PDI-myc, cells will continue to synthesise endogenous PDI. Therefore, it was important to characterise the relative localisation of transfected wild-type and Y393C-PDI in regard to the endogenous PDI. Figure 5.1 shows HT1080 fibroblasts and Saos-2 osteoblasts transfected with Y393C-PDI-myc and stained for -myc and PDI. Y393C-PDI-myc generally colocalises with endogenous PDI in the ER. Coloc 2, a widely used colocalisation analysis plugin run by FIJI, was used to quantitatively assess the colocalisation of Y393C-PDI and its endogenous counterpart. Both proteins colocalise almost completely, as shown by the signal intensity scatter plots generated by the plugin. A strong positive correlation and a Y-intercept at zero depicts strong colocalisation between -myc and PDI signals (Spearman's rank correlation: 0.94; Pearson's R value (no threshold): 0.95).
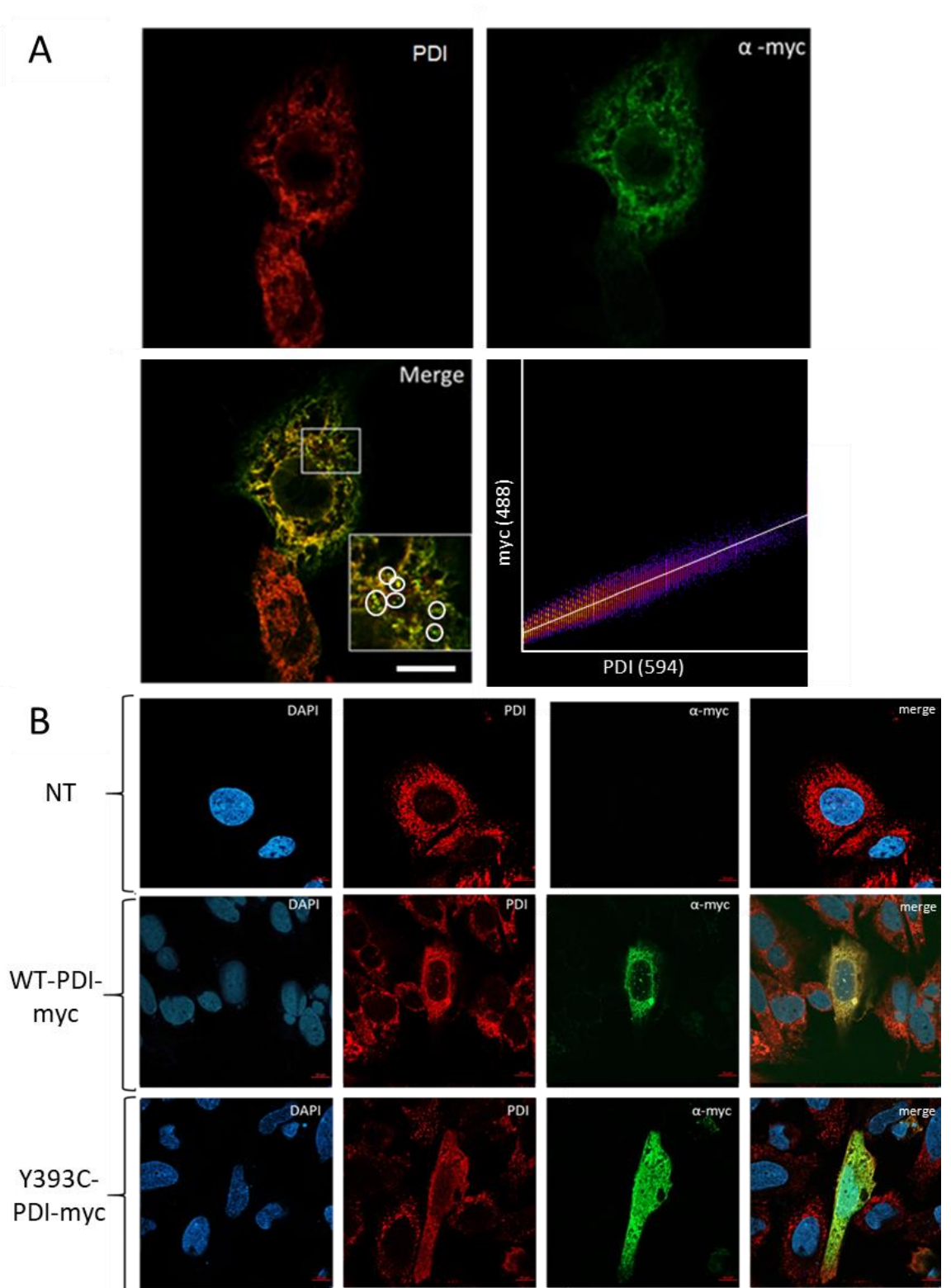
Figure 5.1. Y393C-PDI colocalises with endogenous PDI in HT1080 cells. (A) Individual channel and merged images of Y393C-PDI transfected and non-transfected HT1080 cells. The Y393C-PDI transfected cell shows clear tubular ER morphology. Some vesicular objects are boxed and magnified in the merged image. Colocalisation between 488 and 594 channels is confirmed by adjacent 2D colocalisation histogram generated by Coloc2. (B) Individual channel and merged images of non-transfected, WT-PDI-myc and Y393C-PDI-myc Saos-2 stained for PDI and -myc. Scale bars = 10 nm.

Warmer colours depict higher intensity pixels, and true immunofluorescent signal, rather than background noise. A Coste's P-Value of 1 (standard deviation: 0.04) shows this colocalisation is very unlikely to have occurred by chance, thus supporting the results shown in Figure 5.1A.

As previously stated, the tubular ER has been suggested to be a sign of ER stress (Lee, 2020), as evident in the transfected cell. The merged panel of Figure 5.1A allows for comparison between a transfected cell (top) and non-transfected cell (below), which is useful for observing the ER morphology. A magnified section of the merged panel shows this in greater detail (boxed), with clear overlap of the red (594) and green (488) channels towards the perinuclear region of the cell. This colocalisation seems to be lost at the periphery of the ER, where the -myc (488) signal does not colocalise to a wild-type PDI (594) signal, producing a green fringe around the edges of the ER. Furthermore, small vesicle-sized objects less than 1 μm in size appear in this boxed region, which are circled. These could be products of the ER-Golgi COPII transport system, or PDI associated lysosomes. To determine if this is the case, co-staining with Lamp2A or Lamp2B or the relevant COPII markers would confirm if these were lysosomal, or ER-Golgi vesicles respectively. The majority of these objects appear in only the Y393C-PDI (488) channel (green), or in both (yellow), but not in the red only channel. This suggests they contain predominantly mutant PDI over wild-type PDI.

Figure 5.1B shows both WT-PDI-myc and Y393C-PDI-myc transfected Saos-2 osteoblasts co-stained for α -PDI and α -myc. Y393C-PDI and WT PDI co-localise to the ER, as in HT1080 cells. The cell transfected with Y393C-PDI-myc appears to show potential characteristics of stress. These include a long and extended ER, evidence of ER tubule formation and distinct unstained zones. The WT-PDI-myc transfected cell does not show these characteristics and appears more analogous to the non-transfected cells around it.

The endogenous PDI signal appears stronger in both WT PDI and Y393C-PDI transfected cells when compared to the surrounding non-transfected cells, as displayed in Figure 5.1B. This may be a result of the transcription and translation of the additional transfected DNA, thus resulting in overexpression of PDI. This is further highlighted in Figure 5.2, which shows the relative proportions of each signal as mean pixel intensity for each cell shown in Figure 5.1. Figure 5.2A shows each
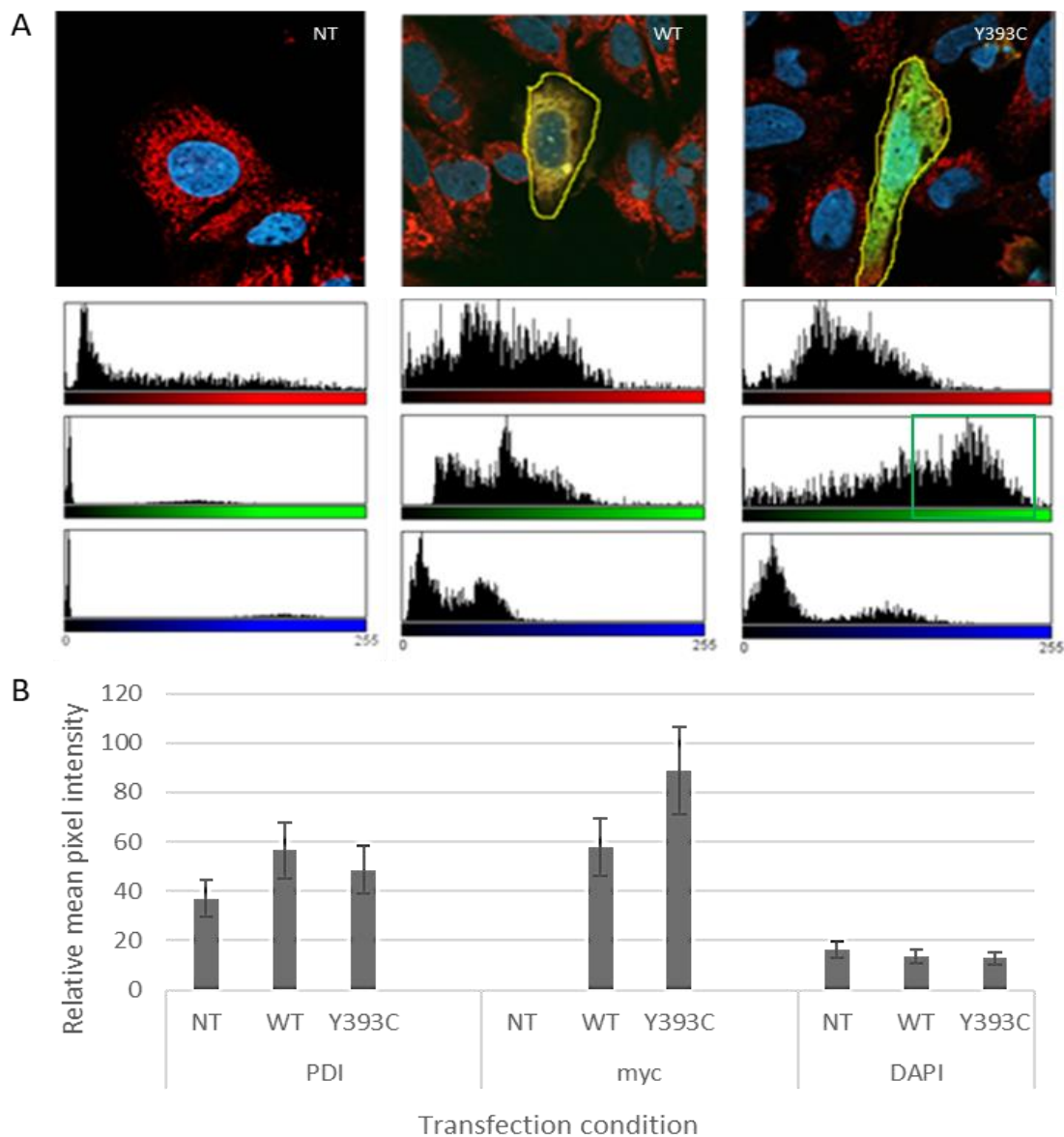
Figure 5.2. Signal intensity for transfected PDI appears higher in Y393C-PDI-myc cells than WT-PDI-myc. (A) Channel intensity histograms for the highlighted cells from Figure 5.1. These show variation in PDI (594; red), -myc (488; green) and DAPI (405; blue), signal between non transfected, WT-PDI-myc transfected and Y393C-PDI-myc cells highlighted above (yellow). (B) relative mean pixel intensity for the above cells including non-transfected (NT) as a negative -myc control. Images corrected for background calculated by ImageJ. Error bars show standard deviation for each signal.

channel histogram for the highlighted cell, showing higher green (488) signal in the Y393C transfected cell, despite similar levels of endogenous PDI expressed (boxed). The WT-PDI-myc expressing cell displays a higher intensity signal for its endogenous PDI, but this is not reflected to this extent in Y393C-PDI-myc cells. Laser power, gain and intensity were kept controlled during image capture to avoid technical variation.

Furthermore, Figure 5.2B shows the relative mean pixel intensity as a bar chart for each highlighted cell as automatically calculated by FIJI following thresholding of each selected area of the image. The first two bars depict an increase in endogenous PDI expression between non-transfected and WT-PDI-myc/Y393C-PDI-myc transfected conditions. This again suggests there may be some effects of plasmid uptake on the ER morphology due to stress, as seen in Figure 5.1A. The signal intensity bars of -myc depict the proportion of transfected PDI in each transfection condition. As expected, the non-transfected cells have no -myc signal, however, a greater increase is seen in Y393C-PDI-myc expression when compared to that of WT-PDI-myc, as was observed in Panel A. Standard deviation for green (488) signal of transfected Y393C PDI and WT PDI do not overlap, suggesting this increase is of interest.

5.2. The quantity of collagen I production is highly variable between Saos-2 osteoblasts, and does not appear to be affected by Y393C-PDI-myc transfection.

Due to PDI's key role in collagen processing, it was important to discern if the Y393C mutation has an impact on collagen distribution in vesicles and the deposited collagenous extracellular matrix (ECM). Figure 5.3A shows an example of collagen within intra-cellular vesicles, highlighted in Panel A (Box 1), preceding the deposition into the triple helix fibres of the collagen-ECM matrix (Box 2).
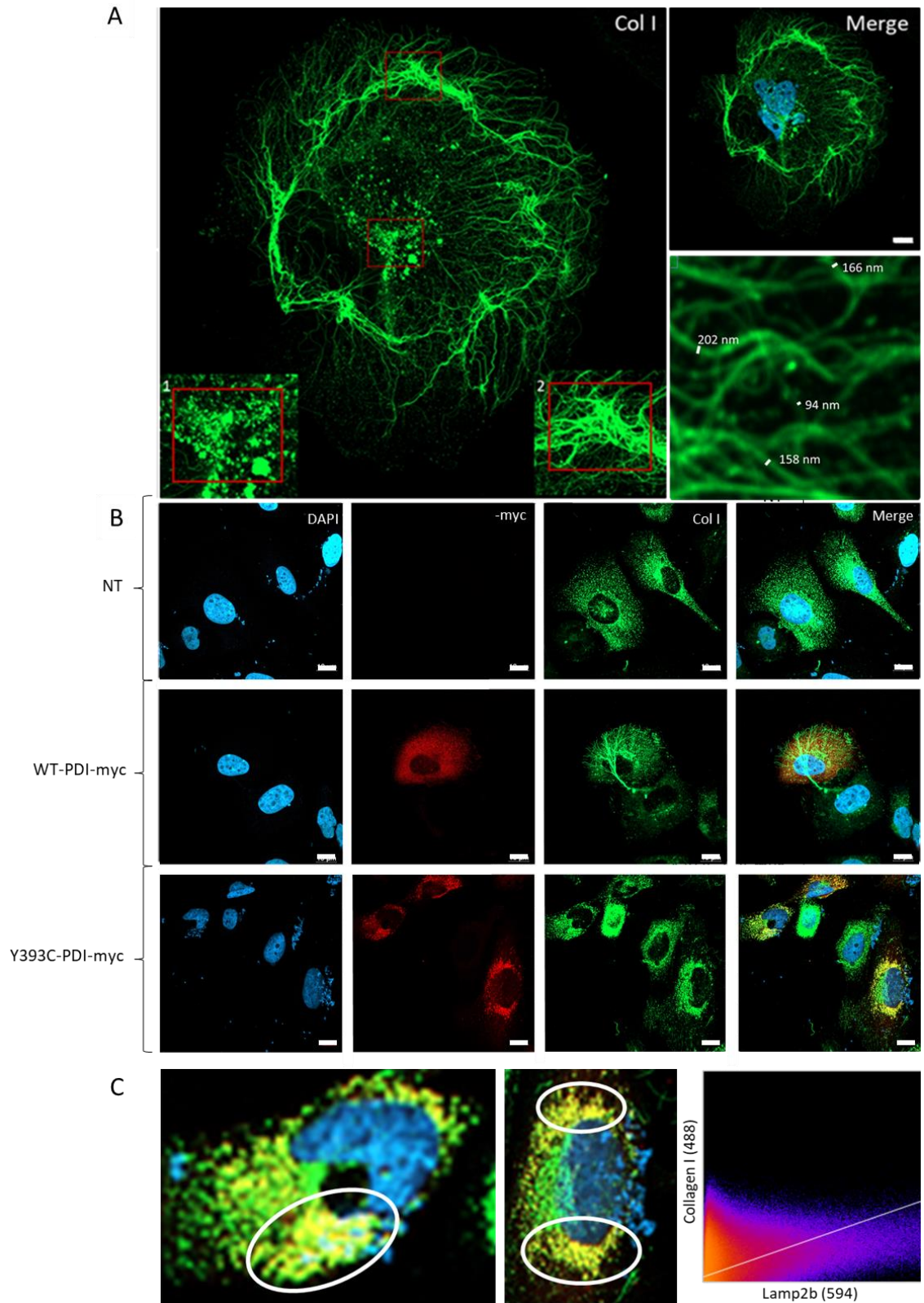
Figure 5.3. Characterising Collagen I production in Saos-2. (A) Non-transfected Saos-2 stained for Collagen I (488) showing both vesicular (1) and deposited collagen states (2). Merge shows location of nuclei. High magnification image (right) shows diameters of four deposited collagen fibrils. (B) Non-transfected, WT-PDI-myc transfected and Y393C-PDI-myc transfected Saos-2 osteoblasts stained for -myc (594) and Collagen I (488) at 63x magnification. Scale bar = 10 µm. (C) magnified sections of bottom right panel of (B) showing colocalisation of Collagen I to Y393C-PDI. Colocalisation histogram generated by Coloc2 for cell shown in middle panel.

Measurements confirming this structure as deposited collagen ECM are shown in the bottom right panel of Figure 3.5A; four randomly chosen fibrils measure 166 nm, 202 nm, 94 nm and 158 nm respectively. This is consistent with the known size of deposited fibrils measuring anywhere between 20 – 300 nm (Silver, 1992; Bancelin, 2014). This deposited collagen can form large matrices around multiple cells, as shown by the 122.6 µm wide structure formed.

Figure 5.3B shows non-transfected, WT-PDI-myc transfected and Y393C-PDI-myc transfected Saos-2 osteoblasts stained for α -myc and collagen I. Again, there is a mixture of vesicular and deposited collagen between all conditions apart from Y393C-PDI-myc transfected cells, of which no cells were observed to successfully deposit collagen I. Across all transfected cells there is no immediate difference in the quantity of vesicular collagen production between wild-type and Y393C-PDI states. However, some colocalisation of Y393C-PDI and collagen vesicles is apparent, as seen in Figure 5.3B and magnified in part C. In these merged images there appears more colocalization (yellow) than distinct -myc signal (red). This suggests more transfected Y393C-PDI is colocalising with collagen than not (circled), however, there are clearly areas in which collagen is distinct from Y393C-PDI, shown by the rest of the green signal.

To establish if this finding is statistically significant, colocalisation was further investigated using coloc2. This produced a channel intensity histogram for the cells shown in C, alongside statistical correlation analyses. These returned Pearson's R and Spearman's rank correlation values as 0.68 and 0.65 respectively, showing a semi-strong colocalisation as reflected in the merged channel panel.

5.3. Lysosomal marker Lamp2b distribution changes in Y393C-PDI expressing HT1080s

Owing to the relationship between misfolded proteins, ER stress and the lysosomal degradation system, it was important to characterise lysosomal behaviour in Y393C-PDI-myc transfected cells. Figure 5.4. shows non-transfected and Y393C-PDI-myc transfected HT1080 cells fixed and stained for α -PDI or α -myc, alongside Lamp2b, a lysosome membrane-associated glycoprotein used extensively as a lysosomal marker.
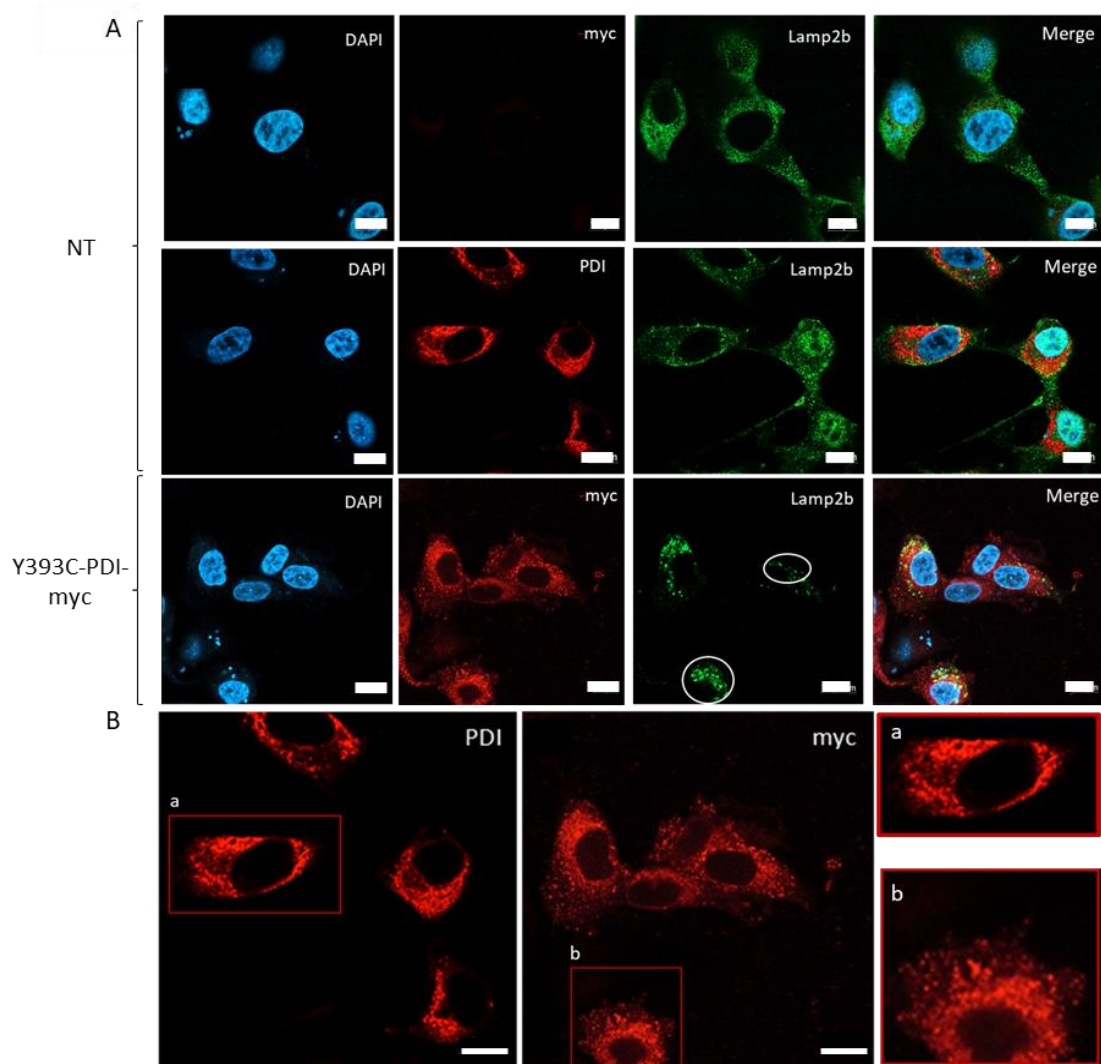
Figure 5.4. Lysosomal distribution and morphology appears abnormal in Y393C-PDI-myc transfected HT1080s. (A) Immunofluorescence of Lamp2b and Y393C-PDI transiently transfected into HT1080 cells. Negative controls show normally expressed Lamp2b throughout the cytoplasm in punctate lysosomes. Y393C-PDI-myc transfection shows a general decrease in lysosomal number and an increase in size in those transfected with Y393C-PDI-myc. (B) Further magnified sections of non-transfected and Y393C-PDI transfected cells from (A) showing variation in ER staining from endogenous PDI and Y393C-PDI. Scale bar = 10 μm.

As seen previously, Figure 5.4A shows Y393C-PDI transfected cells display more irregular ER stains, as shown in the relevant 594 nm channels of A portraying PDI and -myc signal. This may infer they are less healthy than their non-transfected counterparts. In Y393C-PDI-myc transfected cells, the -myc signal appears more concentrated towards the nuclear periphery, when compared to the non-transfected condition. This is further highlighted by the magnified images in Figure 5.3B showing a magnified section of the boxed cells, which were chosen for similar size and shape. The cell in the left-hand panel marked by (a) stained for PDI displays the typical ER stain previously seen, however the cell in the right-hand panel (b) shows a more broken stain, which may consist of ER tubule cross-sections.

Comparison between NT and Y393C-PDI transfected cells highlights differences in the morphology and distribution of lysosomes as shown in green (488) panels in Figure 5.4A. To assess the size and distribution of lysosomes, 3D location maps for objects above 0.2 μm were produced in cells shown in Figure 5.4A and displayed in Figure 5.5A. This minimum threshold enables the removal of background noise, and no maximum threshold allows for the known variation in lysosome size (de Araujio, 2020). Non-transfected cells, as displayed in the first two rows of Figure 5.4A, appear to have similarly high numbers of lysosomes. This is confirmed by 3D object location maps as shown in Figure 5.5A, counting 66 and 50 respectively. After Y393C-PDI transfection, there appears a lower Lamp2b positive object count than seen previously, shown in both the circled cells in 5.4A. This is reiterated by the rightmost 3D object location map in Figure 5.5A, where only 22 objects above 0.2 μm were detected in the non-circled cell.
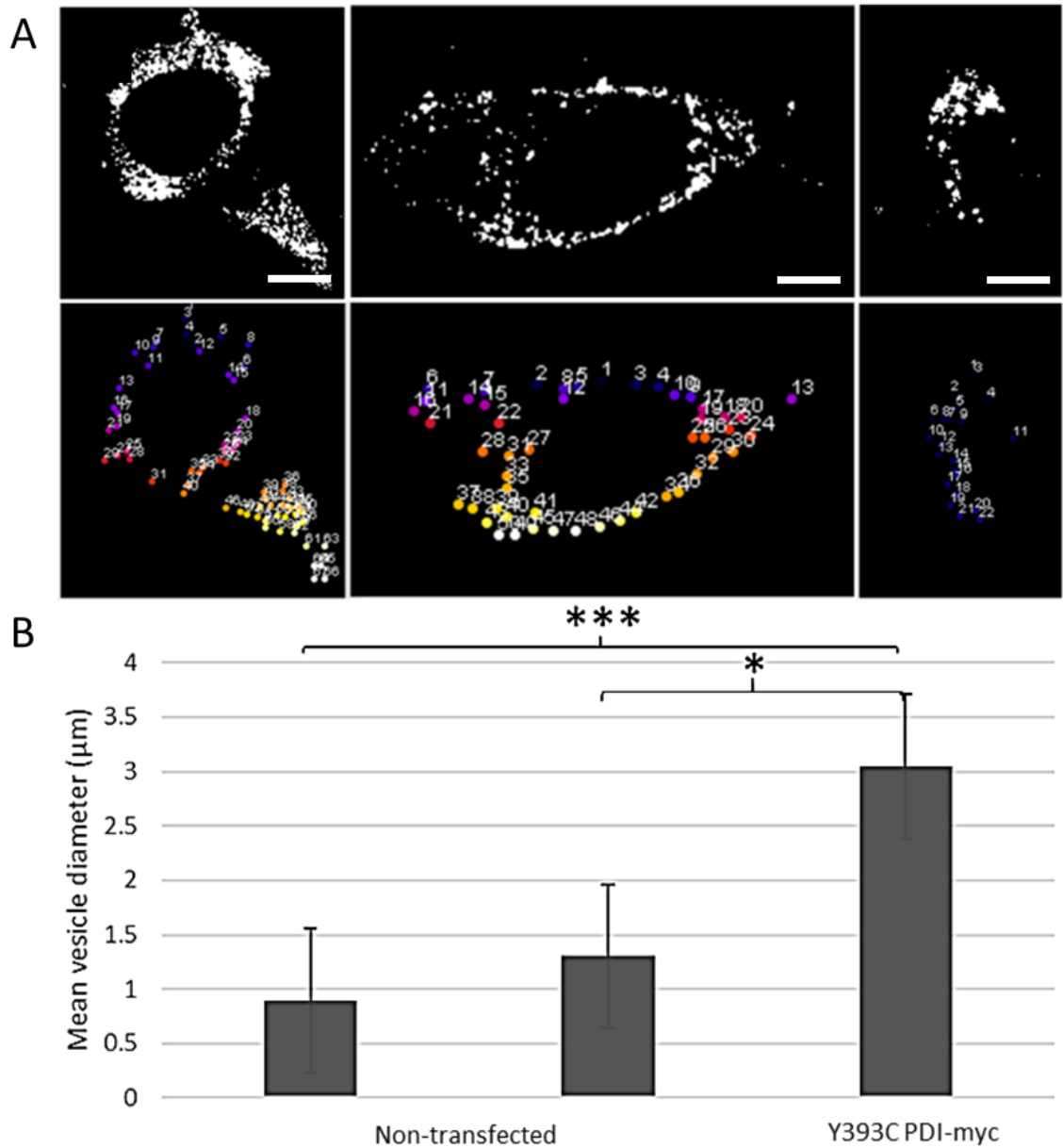
Figure 5.5. Y393C-PDI expressing HT1080 cells have significantly larger lysosomes than wild-type PDI controls. (A) Thresholded images and location maps of Lamp2b marked objects (lysosomes) above 0.2 µm in diameter counted in cells shown in Figure 5.4A. Left and middle panels show non-transfected cells, Y393C-PDI transfected cell shown in right. Scale bar = 10 µm. (B) Bar chart showing average vesicle diameter as calculated by ImageJ for each transfection condition in all green (488) channels in Figure 5.4A. Error bars represent standard deviation around the mean. T-tests show *** significance (p = 0.00145); * (p = 0.03365).

Furthermore, the lysosomes detected in Y393C-PDI-myc cells appear significantly larger than those of their non-transfected counterparts, as highlighted in Figure 5.5B. When a T-test was applied to the raw data there was deemed to be no significance between non-transfected cells (p > 0.05). However, there is significance between lysosome size for both non-transfected conditions compared to Y393C-

73

PDI-myc (p ≤ 0.001; p ≤ 0.05 respectively). These organelles are larger than expected from the literature; HT1080 lysosomes are usually 400 nm (0.4 µm) or above in diameter (Yordanov, 2019). Therefore, those observed here with a mean diameter of approximately 3 µm represent an almost 10-fold increase in typical size.

5.4. The morphology and distribution of lysosomes in Saos-2 cells

Having observed possible effects of Y393C-PDI on the lysosomal trafficking system in HT1080 cells, the characterisation of lysosomes in the osteoblast-like Saos-2 was performed. This would enable comparison between NT, WT-PDI-myc and Y393C-PDI-myc transfected osteoblasts, allowing us to discern if the effects observed in HT1080 cells are also true for the Saos-2 osteoblasts, with the removal of any transfection effects.

As expected, Figure 5.6. shows that the size and distribution of lysosomes in NT Saos-2 osteoblasts are similar to NT HT1080 cells. Lysosome size in osteoblasts is also highly variable, reported to be between 0.2 – 1 µm in diameter which is concurrent with Lamp2b staining in Figure 5.4A (Iwayama, 2019; Nabavi, 2008). However, there is a greater variation in individual lysosome diameter between cells shown in Figure 5.6A and Figure 5.6B, with a higher average vesicle count also seen clearly compared to HT1080. This is further highlighted by location and surface maps of Lamp2b positive objects shown in Figure 5.6C. These object maps were generated from thresholded images of cells shown in part A, in the rightmost panels. The plugin detected 66 objects in the cell shown in Figure 5.6A, and 118 in the group of three cells in part B, averaging 39 lysosomes per cell. This is again concurrent with osteoblasts characterised in the literature, showing these characteristics of the osteoblast-like Saos-2 are typically replicated in primary cells (Nabavi, 2008).
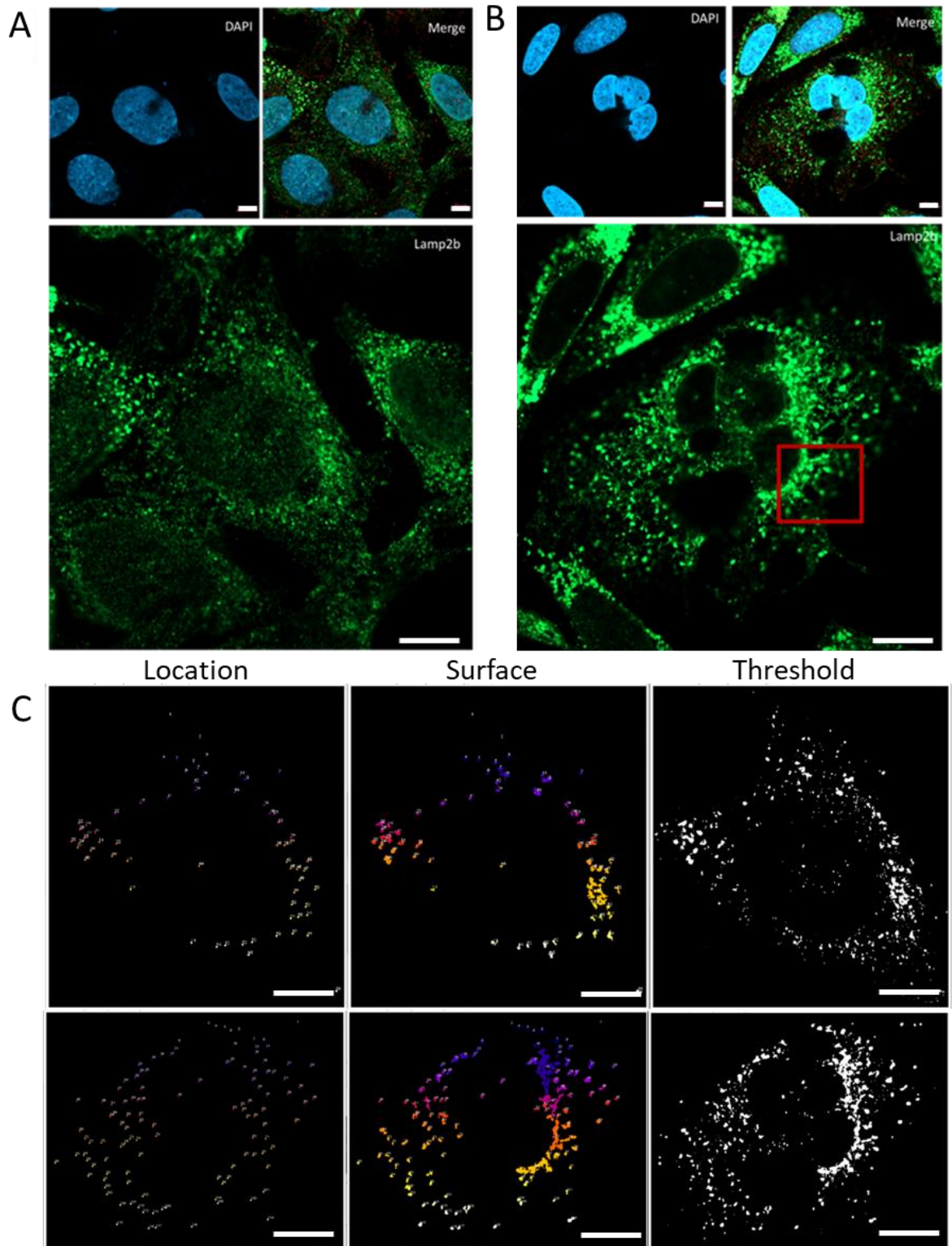
Figure 5.6. Characterisation of lysosome size and distribution in Saos-2. Immunofluorescence of Lamp2b in non-transfected Saos-2 at 63x magnification. (A) Normal distribution of Lamp2b stained lysosomes. (B) Unusual Lamp2b positive staining, appearing to adhere to a tubular network underneath the vesicular lysosomes. (C) Objects identified as Lamp2b positive are shown as location maps (left-hand panels), surface maps (middle) and the original thresholded images (right-hand panels). Scale bar = 10 μm.

The surface maps in Figure 5.6C show a similar standard size of lysosome between both parts A and B, which is typical of osteoblasts. However, this also highlights some unusual association to a tubule-like ultrastructure shown in the boxed region of B, potentially pertaining to the ER or a cytoskeleton network. In summary, this data shows NT Saos-2 cells display normal lysosome size and shape, as expected from the literature.

5.5. The microtubule cytoskeleton appears largely unaffected in Y393C-PDI expressing Saos-2

As seen in Figure 5.6, there appears some association of the lysosomal organelles to a tubular network of the cell. It is accepted in the literature that lysosomes can be trafficked to target areas of the cell along the microtubule cytoskeleton (Matteoni, 1987; Collot, 1984). This is further confirmed to be the case in osteoblasts (Fujiwara, 2016). Microtubules are also known to facilitate the extension of ER tubules via a number of mechanisms, a role potentially relevant to CCS1 (Waterman-Storer, 1998). Therefore, it seemed necessary to characterise the appearance of this cellular ultrastructure in cells expressing wild-type PDI and the Y393C mutated protein.

Figure 5.6. shows WT-PDI-myc and Y393C-PDI-myc transfected Saos-2 co-stained for -myc and α tubulin, alongside non-transfected cells co-stained for PDI and α tubulin. After possible preliminary evidence suggesting the organisation and formation of α tubulin into microtubules in HT1080s was compromised, the experiment was repeated in Saos-2, and with a different fixative known to better preserve the cytoskeleton (Fixative B). There appears no discernible difference in microtubule polymerisation between endogenous and WT-PDI-myc transfected cells, however the Y393C-PDI-myc cells do appear to display slightly lower levels of microtubule preservation. As depicted in panels (a) and (b) of Figure 5.6B, cells successfully transfected with Y393C-PDI appear to display less definition of fully formed tubules than their non-transfected counterparts, highlighted in these magnified panels.
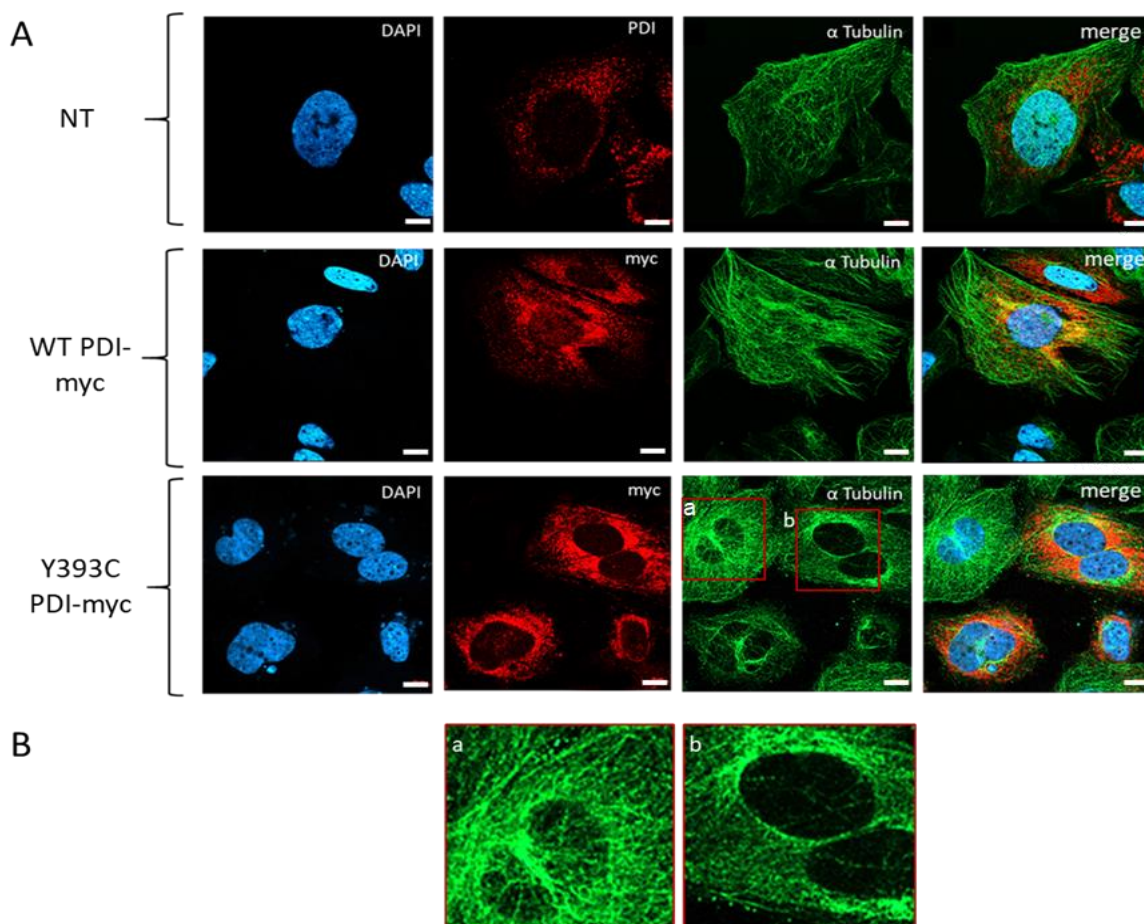
Figure 5.7. The microtubule cytoskeleton appears generally unaffected between wild-type and Y393C-PDI expressing cells. (A) Immunofluorescence of Saos-2 osteoblasts co-stained for wild-type PDI, -myc and α tubulin. Non-transfected cells stained for PDI and α tubulin are shown in top row panels, and transfected cells stained for -myc and α tubulin. -myc signal in middle panels shows WT-PDI-myc; bottom panels show Y393C-PDI-myc. (B) magnified sections of Y393C transfected cells showing tubulin stains between non-transfected (a) and Y393C-PDI transfected (b) cells. Scale bar = 10 μm.

However, the unsuccessfully transfected cell in Figure 5.7B also shows less well-preserved microtubules, so these differences are likely to not be biologically significant, and a result of fixation variability. Better preservation of this cytoskeleton may be a result of the non-transfected cell undergoing mitosis, which is highly dependent on polymerised microtubules (Sharp, 2000; Sawin, 1992). Further experimentation would confirm if these differences can be replicated. Treating Y393C-PDI-myc cells with colchicine which is known to inhibit microtubule polymerisation (Skoufias, 1992) would act as a positive control for the de-polymerisation of this cytoskeleton in wild-type PDI expressing cells. This would allow a better comparison Y393C-PDI effects in osteoblasts and determine whether increased susceptibility for microtubule depolymerisation results from the cellular stress caused by this mutation.

5.6. Lysosomal marker Lamp2b staining in Y393C-PDI-myc expressing Saos-2 cells

The HT1080 immunofluorescence shown in Figure 5.4 was replicated in Saos-2, including a visual comparison of both ER and lysosome morphologies. The results of this are shown in Figure 5.8. Non-transfected, WT-PDI-myc transfected Saos-2 and Y393C-PDI-myc transfected Saos-2 are shown in top, middle and bottom panels respectively. These are stained for -myc and Lamp2b, with no -myc signal present in non-transfected cells as expected. Part B shows -myc signal for both WT-PDI-myc and Y393C-PDI-myc cells A (boxed), to compare ER morphology and PDI distribution, as was done in Figure 5.4B showing HT1080 cells. A larger, more tubular ER stain is observed alongside a reduction in lysosomal number in Y393C-PDI-myc Saos-2, mirroring that seen in Y393C-PDI-myc HT1080s.
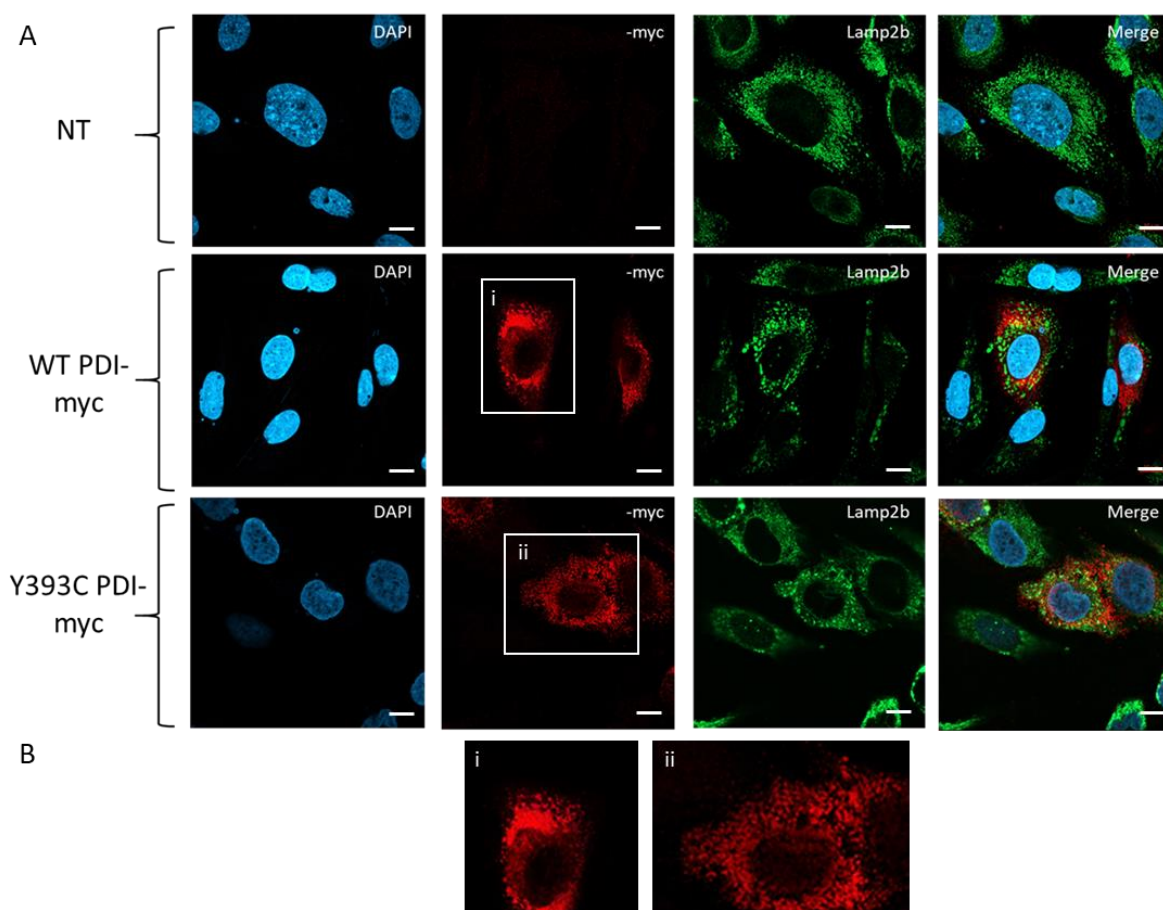
Figure 5.8. Lysosome size and distribution observed in Saos-2 appears to reflect that of HT1080 cells. (A) Fluorescence microscopy of Lamp2b and -myc tagged Y393C-PDI in Saos-2 osteoblasts at 63x magnification, in NT, WT-PDI-myc transfected and Y393C-PDI-myc transfected cells. (B) magnified sections of -myc panels showing WT-PDI-myc, and Y3993-PDI-myc respectively. Scale bar = 10 µm.

79
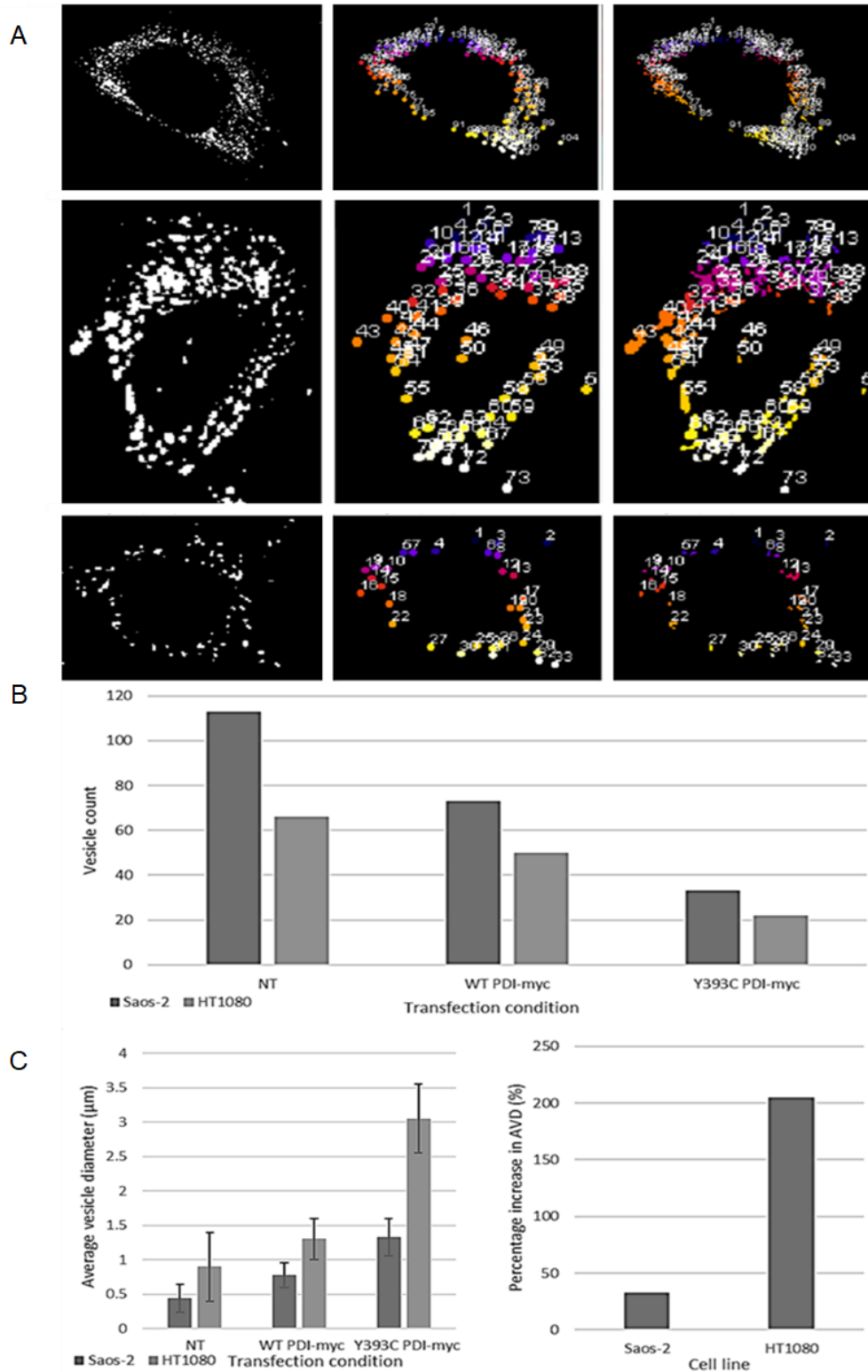
Figure 5.9. Post-acquisition analysis of lysosome size and distribution as observed in Figure 5.8. (A) Thresholded images (left-hand panels), location maps (middle panels), and surface maps (right-hand panels), of lysosomes identified in cells shown in Figure 5.8. (B) Average lysosome count detected by ImageJ for cells shown in Figure 5.4A (HT1080) and Figure 5.8A (Saos-2). (C) Comparison between average lysosome diameter (AVD) for randomly selected HT1080 and Saos-2 cells for each transfection condition (left). Standard deviation shown by error bars. Percentage increase in AVD between WT-PDI-myc and Y393C-PDI-myc transfected Saos-2 and HT1080 cells (right).

Figure 5.9A shows 3D location and surface maps of lysosomes in randomly selected cells from Figure 5.8A. 113, 73 and 33 objects were identified as lysosome

80

organelles in non-transfected, WT-PDI-myc and Y393C-PDI-myc transfected cells respectively. These data reflect lysosome numbers observed in HT1080 cells, as shown in the quantitative analysis in Figure 5.9B.

As seen previously, characterisation of the NT Saos-2 lysosomes showed smaller but higher frequency of these organelles compared to NT HT1080 cells. This is reiterated in bar graphs in Figure 5.9C showing higher average vesicle diameter percentage increase in NT HT1080s than NT Saos-2. Osteoblasts and fibroblasts may potentially respond differently to Y393C-PDI, indirectly impacting the lysosomal system. Therefore, this comparison both within and between cell lines provides cell-specific context for these organelles, as well as investigating the CCS1 mutant.

Interestingly, despite HT1080 lysosome size increasing drastically in Y393C-PDI-myc conditions compared to wild-type in Figure 5.5, this not observed in Saos-2 cells, as displayed in Figure 5.9C. However, standard deviation bars in Panel C (left) do show non-overlapping variation between wild-type and Y393C-PDI conditions, suggesting this increase is still of interest.

The average lysosome diameter (AVD) for HT1080 NT, WT-PDI-myc and Y393C-PDI-myc cells are 0.894 µm, 1.302 µm, 3.051 µm respectively, shown in Panel C, left graph. This shows an increase of more than 200% between the latter two transfected conditions (right graph). As stated, this scale of increase is not reflected in the equivalent Saos-2 conditions; AVD measurements for the three conditions are 0.438 µm, 0.777 µm and 1.328 µm respectively. This is a much less substantial increase (~32%) when compared to HT1080 cells, as displayed in Figure 5.9C, right graph. This suggests a lesser biological relevance of this change in osteoblast-like cells than the fibrosarcoma HT1080s, possibly resulting from the different tissue types the cells represent.

5.7. Using live cell imaging to further characterise lysosomal trafficking in non-transfected, wild-type transfected and Y393C-PDI-myc transfected Saos-2

To further investigate the abnormal lysosomes portrayed in the previous figures, live cell time-lapse imaging was undertaken to discern if the movement or directionality of lysosomes was affected alongside distribution and morphology. ER-Tracker™ Blue-White DPX and Lyso-Tracker™ Red were added to NT, WT-PDI-myc and Y393C-PDI-myc transfected cells in glass bottomed dishes 20 minutes prior to imaging. Figure 5.10 shows cells from each transfected condition at timepoints 0, 25 and 50 seconds. This reiterates the observation of a lower lysosome count in Y393C-PDI cells, as total objects defined as 'lysosomes' detected by TrackMate in cells shown in Figure 5.10 time-lapses were recorded as follows: 888 in non-transfected cells, 975 in WT-PDI-myc transfected cells, and 403 and 568 in Y393C-PDI transfected cells respectively.
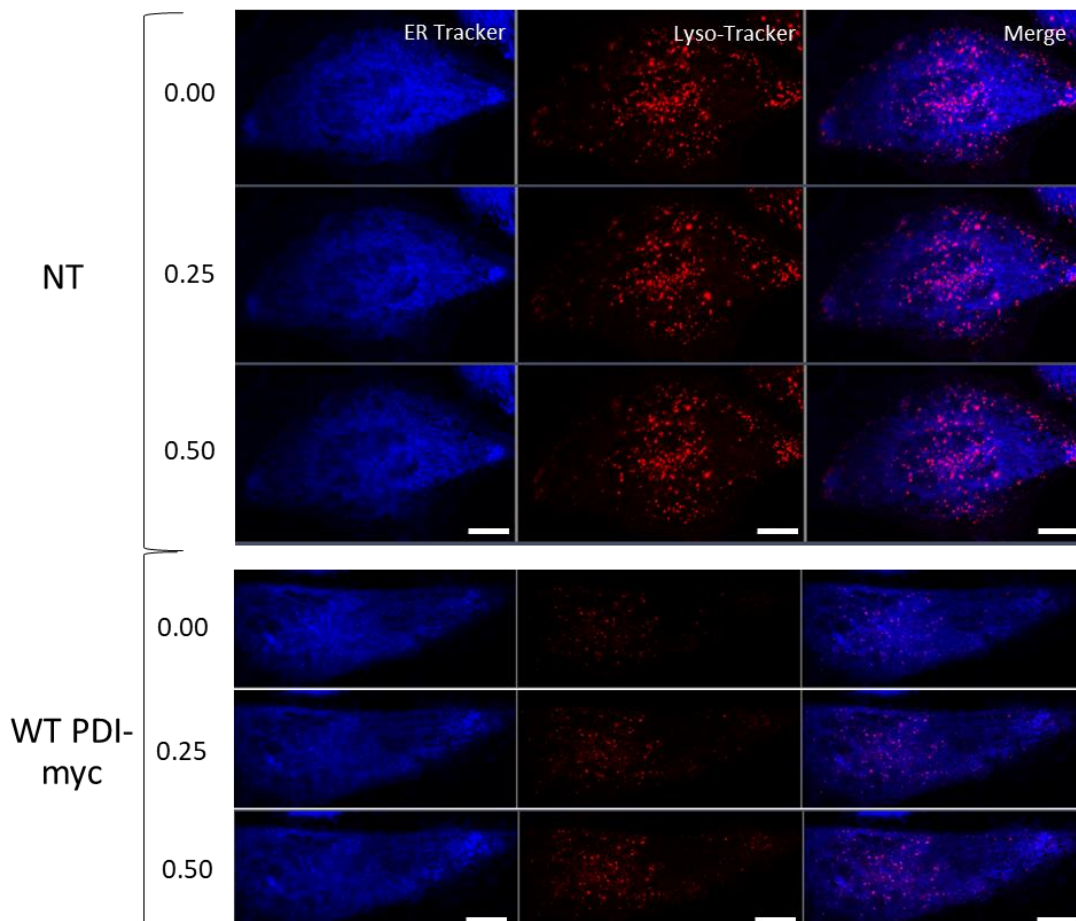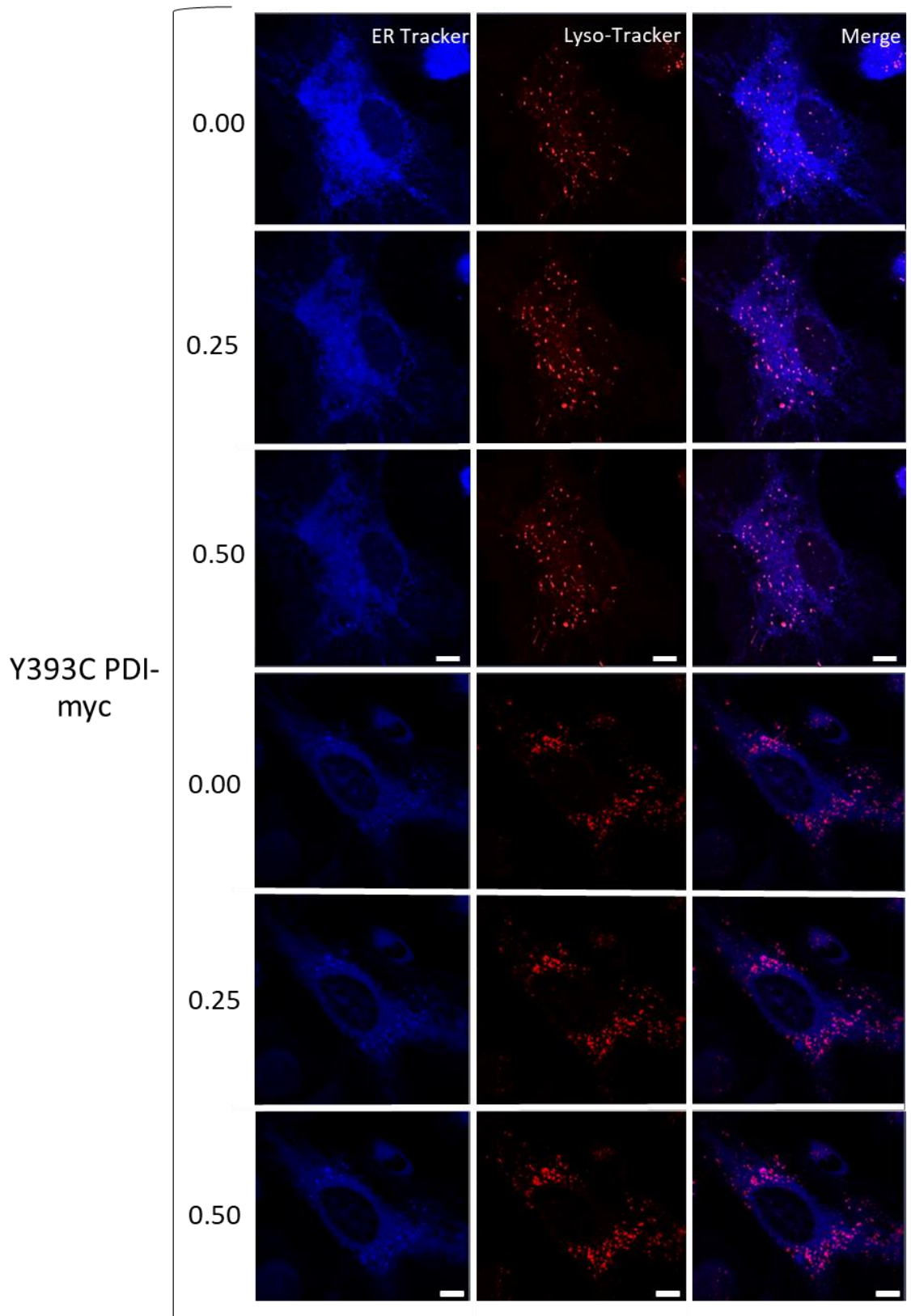
Figure 5.10. Time-lapse imaging of Saos-2 stained using ER-Tracker™ Blue-White DPX and Lyso-Tracker™ Red. Images captured at time frames 0, 25, 50 seconds for each NT and WT-PDI-myc transfected and Y393C-PDI-myc transfected. Scale bar = 10 μm.

As seen previously in fixed cells, there appears a negative correlation between lysosome size and lysosome count inside the cell, with Y393C-PDI cells containing fewer but larger lysosomes than WT-PDI-myc transfected and non-transfected cells. The cells shown in Figure 5.10 are displayed as temporal colour coded hyper-stacks in Figure 5.11 to highlight lysosomal movement changes between Y393C-PDI cells and control cells. These show that larger organelles tend to be more stationary than their smaller counterparts. Blue represents a vesicle's starting position at image frame 001 (1 second), and white represents the objects finishing position at frame 050 (50 seconds). The spectrum of colour between these depicts the vesicle movement across frames, as presented by the coloured bar in Panel A.
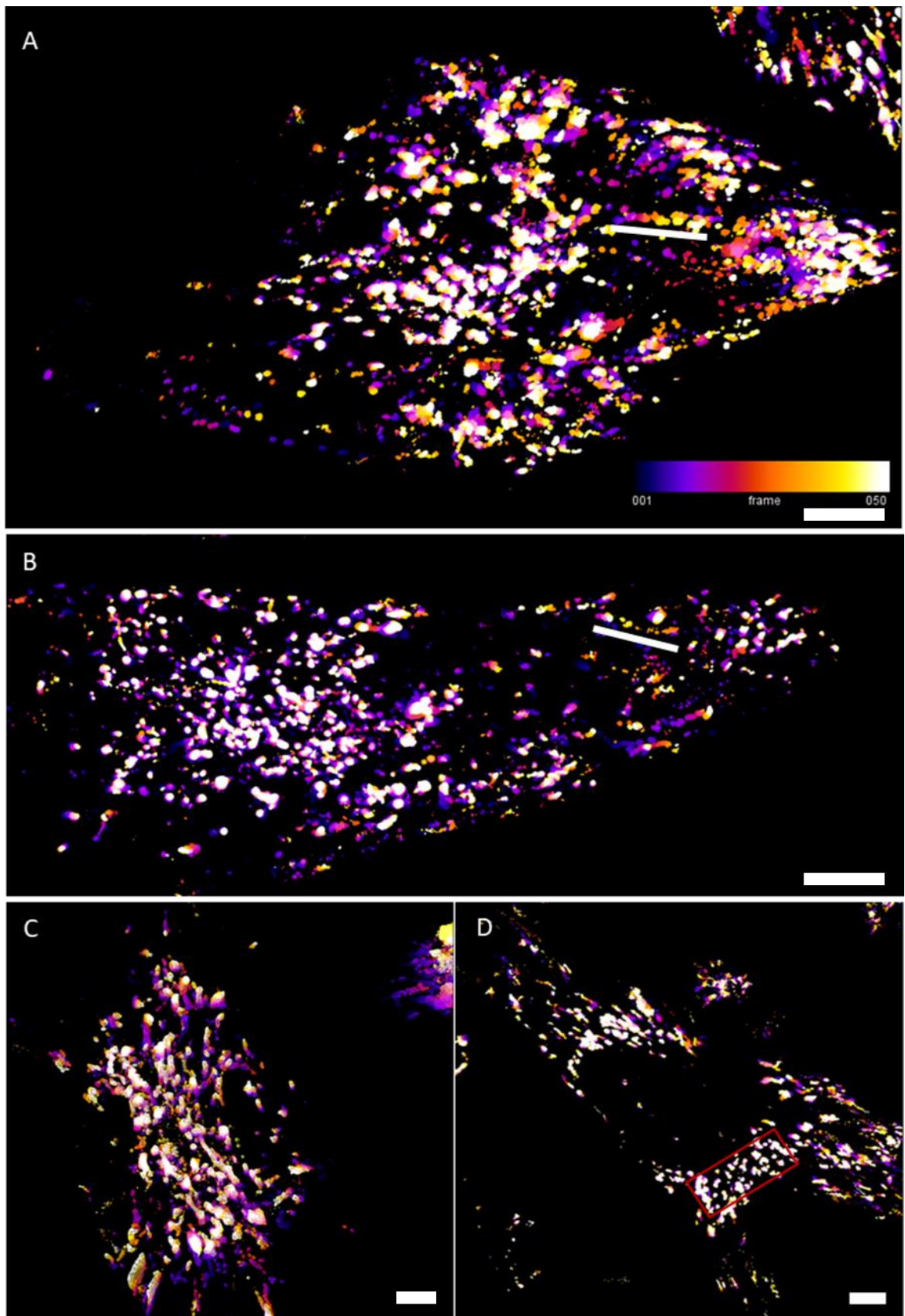
Figure 5.11. Temporal colour coded hyper-stacks produced on ImageJ for cells displayed in Figure 5.10. Non-transfected (A), WT-PDI-myc (B) and Y393C-PDI-myc (C and D). Each shows vesicle location alongside direction and distance moved across frame 1 (blue) to 50 (white). Scale bar = 10 µm.

Non-transfected Saos-2 cells shown in Figure 5.11 panel A display large numbers of normal sized lysosomes moving up to 7 μm in distance over the 50 seconds, shown by a white line. This is as expected from normally functioning lysosome activity (Pu, 2015). There also appears a general collection of these organelles in the cell centre and apical periphery, with distinct gaps of little to no lysosomes present. Panel B shows a typical WT PDI transfected Saos-2 cell displaying much of the same characteristics as non-transfected cells. Some organelles are observed to move long distances of approximately 5 μm, also highlighted by a white line. As observed in NT cells, there are distinct regions of lysosome absence in the cell. However, Y393C-PDI transfected cells in Panels C and D exhibit contrasting characteristics. Firstly, they show a less polarised spread of lysosomes throughout the cell alongside no areas of vesicle absence, and a general reduction in vesicle movement. This is especially noticeable in panel D where organelles found directly at the nuclear periphery (boxed in red) display no coloured 'tails' between the time frames, hence showing no significant movement.

To confirm these observations, Figure 5.12. shows the distance moved in microns by each lysosome detected by the plugin as scatter plots. Track ID refers to an arbitrary number assigned to locate a unique track during TrackMate analysis. Track ID is plotted against the distance moved by each lysosome in microns from 'track start', the frame which the vesicle appears in, to the 'track stop' frame, whenever the lysosome disappears. This is assigned the term Track Displacement, and presented for non-transfected osteoblasts, WT-PDI-myc and Y393C-PDI-myc in the bar chart shown in Figure 5.12B, with error bars showing standard error around the mean.

For both non-transfected and WT-PDI-myc transfected cells, lysosome movement appears normal. A large number of lysosomes move distances measuring 3 microns or more, as marked by a red threshold line. This contrasts to the Y393C-PDI-myc transfected conditions in which only 6 and 7 lysosomes pass or touch the 3 micron threshold line, shown in panels C and D respectively. A large proportion of panel D tracks show a displacement of less than 1 micron, as shown by the white threshold line. Mean track displacement for these cells is displayed in the graph below in part B, with standard deviation as error bars.

One-way Analysis of Variance (ANOVA) was conducted to determine the significance of variation between wild-type and Y393C-PDI expressing cells. Variation between non-transfected and wild-type PDI transfected cells returned a result of no significance ($p > 0.05$; ns), whereas significance at $p < 0.001$ was calculated for variation between WT-PDI-myc and Y393C-PDI-myc cells (***). Again, this reiterates that wild-type PDI expressing cells display no clear differences in lysosomal characteristics, however Y393C-PDI-myc transfected cells display both lower numbers and motility of lysosomes present.
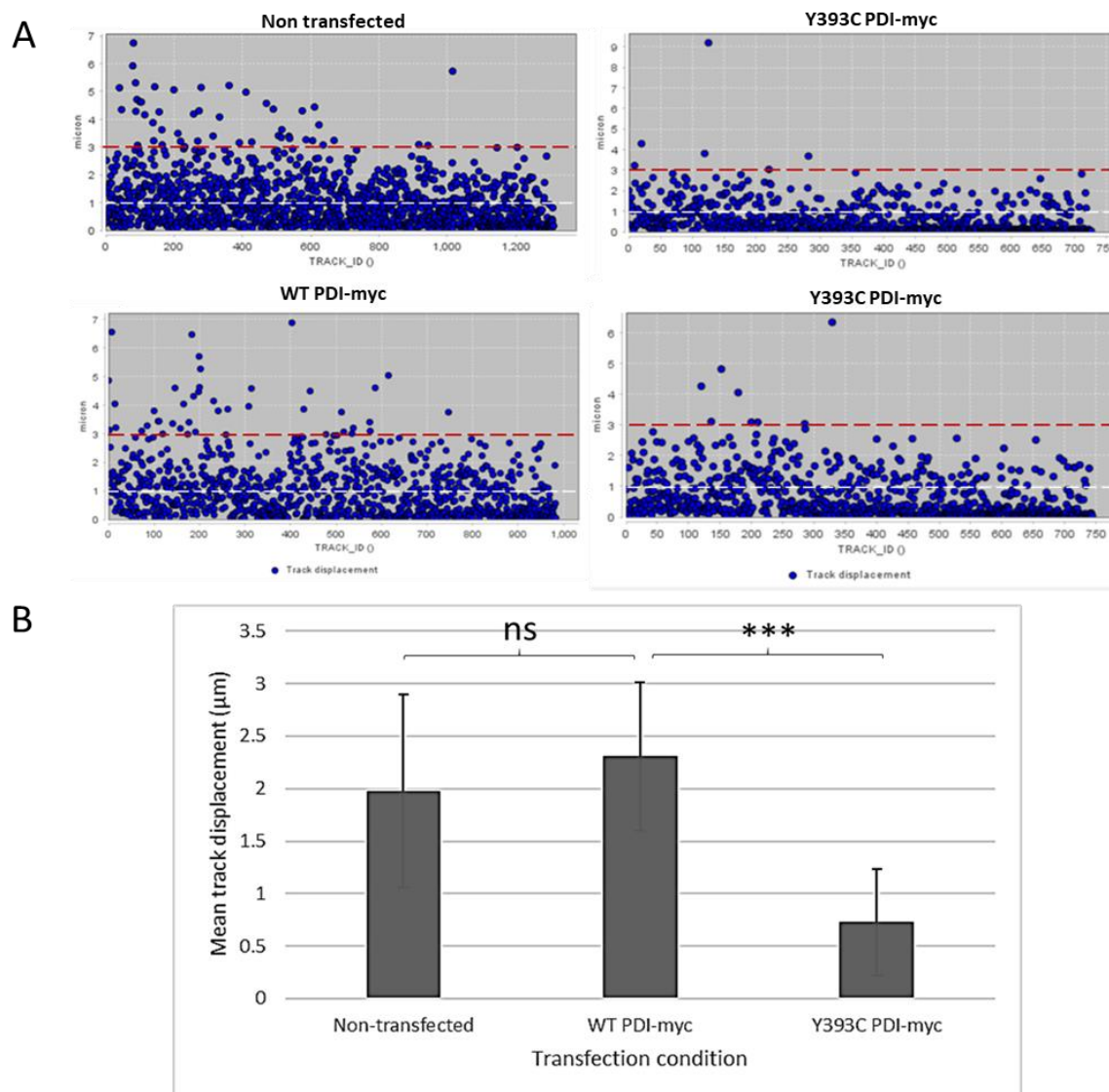
Figure 5.12. Post-acquisition analysis of lysosome motility observed in Figure 5.11. (A) Scatter plots showing Track ID of vesicle against Track displacement (distance travelled by object in microns) calculated from cells shown in Figure 5.11. by TrackMate. (B) Mean track displacement of vesicles recorded from data shown in (A). An average of both cells recorded in C and D provides Y393C-PDI-myc mean. Error bars = standard error around the mean. One-way ANOVA P values = 0.26 (> 0.05) for NT vs WT-PDI-myc; < 0.0001 (< 0.001) for Y393C-PDI-myc.

5.8. Characterising the relationship between Collagen I and lysosomes in Y393C-PDI-myc, WT-PDI-myc and non-transfected Saos-2.

As seen previously in Figure 5.3, the quantity of collagen production is highly variable from cell to cell, however no extracellular deposition has yet been observed by Y393C-PDI-myc cells. To establish if there was any relationship between collagen I and lysosomes, the immunofluorescence in Figure 5.4 was reproduced, staining for Lamp2b instead of PDI. The results of this are shown in Figure 5.13, with examples of vesicular collagen shown in the non-transfected and Y393C-PDI transfected cells. Deposited collagen is shown in the WT-PDI-myc panels, and potentially the bottom panels of Y393C-PDI-myc, although this is inconclusive.

The same larger lysosomes as previously shown in Figures 5.4 and 5.6 are observed in Y393C-PDI-myc transfected cells in Figure 5.13. Areas of positive and negative colocalisation can be observed as yellow or green signal respectively. Distinct areas of green signal observed in predominantly NT and WT-PDI-myc cells suggest non LAMP2b associated collagen. The large lysosomal structures observed in Y393C-PDI-myc conditions throughout this chapter are replicated, and tend to colocalise with collagen I, as can be observed in the channel merge images.
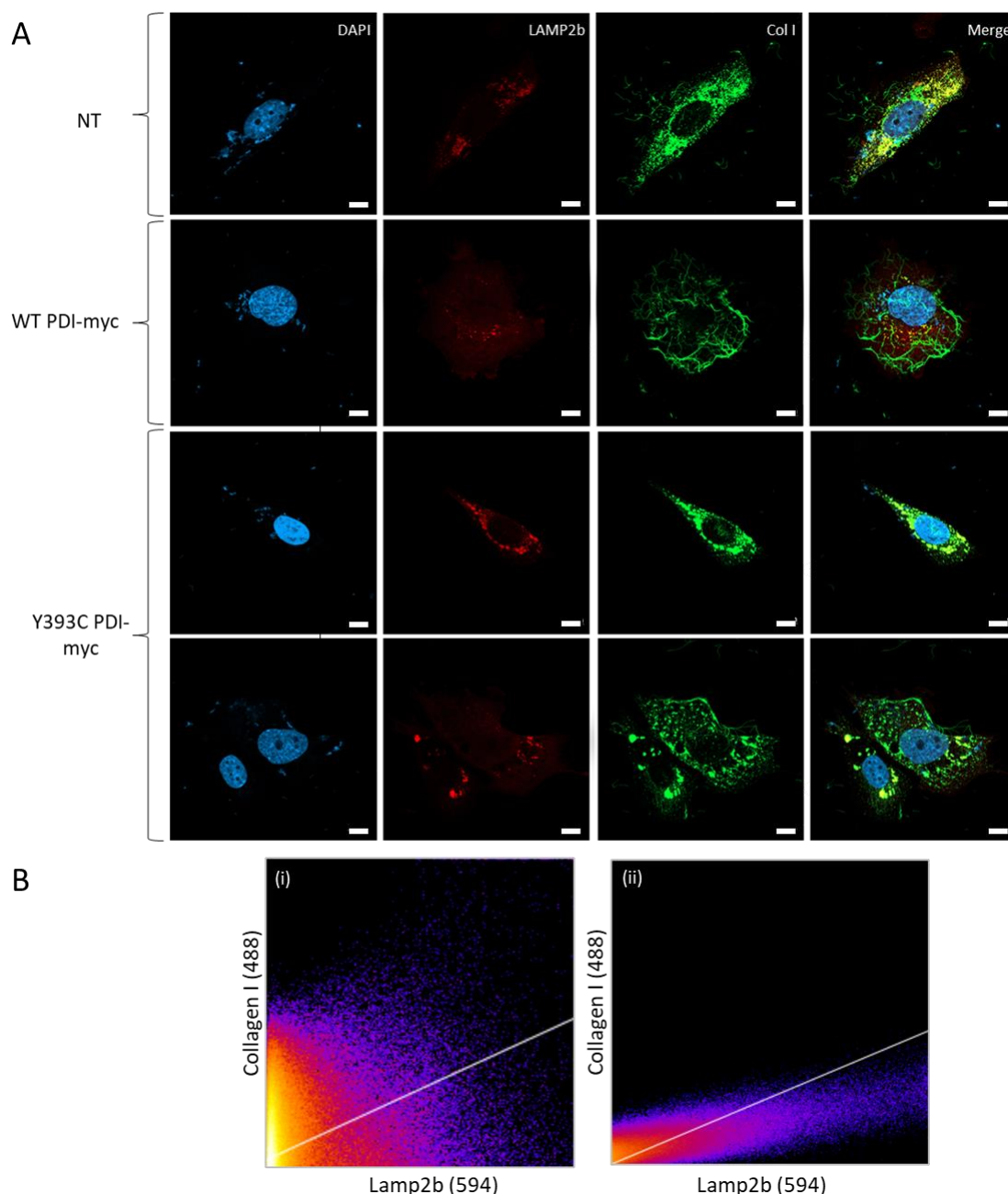
Figure 5.13. Characterising collagen I production and deposition in both wild-type and Y393C-PDI expressing Saos-2. (A) Non-transfected, WT-PDI-myc, and Y393C-PDI-myc transfected Saos-2 cells fixed and stained for LAMP2b (594) and collagen I (488). (B) 2D intensity histograms showing signal overlap in each channel generated by Coloc2 analysis for non-transfected and Y393C-PDI-myc cells. Scale bar = 10 μm.

89

Colocalisation analysis was performed on LAMP2b and Collagen I signal from cells shown in Figure 5.13. after it was hypothesised these large Lamp2b objects may contain misfolded collagen. Figure 5.13B displays the results of this analysis as 2D intensity histograms for the non-transfected, and Y393C-PDI-myc cells shown in part A. This analysis negates the possibility of background or bleed through 'pseudo-colocalisation' between each channel, displaying only true colocalisation of LAMP2b and Collagen I signal. It was deemed unnecessary to test colocalisation on cells showing primarily deposited collagen since, as this is now secreted, it would not colocalise with lysosomal markers. The 2D intensity histograms show signal intensity for both channels, with warmer (white, yellow) colours resembling high intensity and cooler (blue) resembling low intensity pixels. As displayed by warmer colours nearest to the Y intercept, there appears to be some amount of colocalisation of relatively high signal in both cells, as reflected in the respective merged images shown in Part A.

However, the narrower histogram in the channel intensity histogram shown for the Y393C-PDI-myc transfected cell infers a much stronger trend of colocalisation. This is further confirmed by the Pearson's R-value for both cells which is calculated by Coloc2 to be 0.63 for non-transfected, and 0.84 for the Y393C-PDI expressing cell. This once again provides quantitative evidence for stronger colocalisation of collagen and lysosomes in Y393C expressing cells, and less areas where both signals are present but not colocalised.

5.9. Conclusion

In this chapter, the intracellular localisation of the CCS1 mutant Y393C PDI was characterised. Whether this has any untoward impacts on cellular homeostasis and the functions of other intracellular systems, such as lysosomal degradation, vesicle trafficking and collagen production and deposition was then investigated. The discovery that Y393C-PDI almost completely colocalises with WT PDI suggests that it is retained appropriately in the ER and most does not mis-localise. This suggests that despite this 'gain of dysfunction' mutation, PDI still remains in the ER showing it has not been designated for degradation, therefore is still able to pass as functional.

Transfected cells also appear to upregulate the production of endogenous PDI. However, since this is not specific to Y393C-PDI expressing cells, this may have

some links to the transfection procedure, however this appears less drastic in WT-PDI-myc cells than in Y393C-PDI-myc. This transfection and apparent upregulation of translation could contribute to cellular and ER stress, therefore any comparisons made between ER stress and viability include the positive control transfection. As described in Chapter 2, both HT1080 and Saos-2 cells were treated with transfection reagent as part of the negative (non-transfected) control to remove any effects of the chemical agent on cell viability.

The highly tubular ER and decreased viability observed in Y393C-PDI transfected cells suggests the onset of ER stress, as has previously been reported by Rauch (2015). During cell culture and preparation for immunofluorescence, the numbers of Y393C cells successfully adhered, fixed and stained were visibly lower than their non-transfected and WT-PDI-myc counterparts. Alongside this, atypical PDI/ER immunofluorescent stains are observed, including some vesicular structures of unknown origin. These are also observed in CCS fibroblasts by Rauch et al. (2015), and not present in control cells. These could perhaps be linked to the erroneous activity of Y393C-PDI, and a product of PDI in complex with structures it conventionally should not interact with. Another explanation may be Y393C-PDI's collection by proteolytic lysosomes, or evidence of its ER-Golgi transport vesicles during the process of its production. Both these observed characteristics suggest some difference in cellular processing and/or ER stress responses to either collagen I misfolding, or the mutated PDI itself.

Unresolved ER stress may indicate the UPR is proving ineffective, therefore resulting in recruitment of lysosomal-mediated autophagy to clear either PDI or collagen I. Data to support the involvement of lysosomes in this process is shown throughout this chapter. If neither system cannot fully clear the aggregates in sufficient time, then ER stress remains unresolved, which may be reflected in the consistent tubular ER observed in Y393C-PDI expressing cells. The ratio of tubular to sheet-like ER also relates to the organelle's secretory functions alongside induction of stress. Further experiments should be taken to confirm if stress is more prevalent in CCS, and determine if the collagen secretory pathway is affected. Alongside the PDI stain, downstream markers of ER stress such as Binding immunoglobulin Protein (BiP) and C/EBP Homologous Protein (CHOP) may help to indicate whether this ER morphology is a result of proteotoxic stress (Oslowski, 2011).

The induction of ERAD after ER stress has been shown to reduce the number of lysosomes in trophoblast cells, also disrupting cytoskeletal translocation of these organelles to the plasma membrane, and inhibiting exocytosis of the lysosomal contents (Nakashima, 2019). Therefore, characterisation of the lysosomal system in both Y393C and wild-type PDI expressing HT1080 and Saos-2 cells was vital to investigate the effects of the Y393C-PDI mutation. These experiments reflect the lysosomal behaviours observed by Nakashima (2019) and showed not only a decrease in lysosomal number, but an increase in size and linked decrease in mobility around the cell.

Normal globular lysosome vesicle size for HT1080 cells is around 410 nm (0.41 µm), and osteoblast lysosome size appears between 0.2 – 1 µm, as highlighted by LysoTracker™ red and Lamp1 staining in the relevant literature (Iwayama, 2019). However, depending on waste production and subcellular homeostasis, this is known to vary greatly (Lüllmann-Rauch, 2005). Lysosomal number is assumed to be proportional to the amount of activity required by these organelles; how much cytosolic 'waste' is present that requires clearance. The number and size of lysosomes present could also be proportional to the generally larger size of the osteoblasts (Freitas, 1999). Therefore, the known variation in lysosomal size must be, and has been, accounted for when assessing lysosomal size in CCS1 cells compared to wild-type.

When establishing the effects of each condition on these organelles, any Lamp2b positive objects above 0.2 µm in size across all images and time-lapses were considered lysosomes by ImageJ plugin TrackMate. This selection is in concordance with the classic punctate immunofluorescent staining expected from the literature (Sarafian, 1998). This was deemed to remove background signal and provide a viable threshold level of which to measure firstly the existence of these organelles, and then any differences in size and morphology. This includes whether there is aggregation of multiple organelles by not imposing an upper limit of size. This may explain the large 3 µm objects observed in Y393C-PDI-myc HT1080s, and similarly larger lysosomes in Saos-2, observed in both fixed and live cell imaging, hence why these measures were taken. More quantitative and qualitative evidence is needed to confirm these findings, which could be obtained from biological and technical experimental repeats, or staining for other lysosomal markers, such as

Lamp2a or Lamp1 which may more accurately reflect the effects of Cole Carpenter syndrome on these organelles (Nakashima, 2019).

Whilst the transfection efficiency of the cells cannot be experimentally confirmed in live cell imaging, this data does show that an increased size and decreased count of lysosomes in a cell correlates strongly with a decrease in movement, with significance. This is also supported by the relevant literature which shows lysosome mobility is a combination of simple diffusion and active transport moving the lysosome along the microtubule cytoskeleton (Bálint, 2013). Therefore, their size correlates inversely with their motility as larger lysosomes are more difficult to move. This has been suggested as a size dependant 'drag force' on these organelles, again limiting their movement and thus functional capacity inside the cell, however this theory is still controversial (Martinez, 2007). From this data, a decrease in lysosomal motility can be inferred to be the case in Y393C-PDI cells which display these larger lysosomes.

More deposition of collagen I is observed in wild-type PDI conditions, with none observed in Y393C-PDI-myc transfected osteoblasts, possibly resulting from the aggregated misfolded protein being retained in the ER. Furthermore, possible collagen retention inside lysosomes is observed in the Y393C-PDI-myc conditions, as the abnormally large vesicle structures appear to colocalise with collagen. Colocalisation regression lines of 2D intensity histograms produced by ImageJ all intercept close to zero, showing no issues with offset or background thresholding. This gradient should be close to 1, however for collagen-Lamp2b colocalisation data it remains mostly below this value at approximately 0.5 for all conditions. According to the ImageJ user guide, this may be owing to the fact there is only sparse data in one channel or there are multiple colocalising populations of signals. This is likely to be a combination of the two; the LAMP2b immunofluorescence often picks up fewer lysosomes when compared to LysoTracker Red™ as shown in live cell imaging, and collagen I is seen to colocalise independently at multiple areas within the cell with the LAMP2b lysosomal marker, possibly resulting in this intensity variation.

These LAMP2b positive objects appear to contain collagen I in both wild-type and Y393C-PDI expressing cells. However, as inferred by the 2D intensity histograms, the latter mutant cells appear to have a stronger colocalisation of Collagen I to

lysosomes. This suggests misfolded collagen by Y393C-PDI is perhaps not fully retained in the ER, and the lysosomal system is attempting to clear these aggregates, contributing to their swollen size and decreased movement. There is also significant atypical collagen staining outside these organelles, potentially that of aggregated protein still retained in the ER. This lack of misfolded protein degradation and aggregation inside and outside lysosomes is likely to induce ER stress within the cell, therefore contributing to the CCS1 phenotype.

6. ASSESSING CELL VIABILITY BETWEEN WILD-TYPE AND Y393C-PDI CONDITIONS AND THEIR RESPONSES TO COMPETITIVE ENZYME INHIBITION

Introduction:

Y393C-PDI transfected cells typically appear to show increased signs of stress, which can lead to changes in intracellular homeostasis and increased cell death. Therefore, the viability of transfected Y393C-PDI cells in comparison to WT PDI was assessed in work presented in this Chapter.

To establish if Y393C-PDI does increase cell death, microplate-based cell viability experiments were devised, the results of which are shown in this chapter. If any changes in viability are influenced by the addition of PDI inhibitors, this may provide further understanding of the molecular mechanisms of Cole Carpenter syndrome. Small molecule inhibitors (SMIs) are engineered molecules targeting specific residues within a particular protein, thus inhibiting its activity. Their usage as cancer therapeutics is becoming increasingly common, as they provide a deeper understanding into pathways underpinning their target's function within the cell (Khera, 2017).

One of these PDI inhibitors is 16F16, which contains a chloroacetyl group that covalently modifies free cysteine thiols, targeting the two active site residues C397 and C400 of PDIA1 and PDIA3 (Hoffstrom, 2010). This prevents the formation of disulphide bonds within the target protein, thus causing irreversible inhibition. Furthermore, the family of propynoic acid carbamoyl methyl amides (PACMAs) use what is believed to be the same inhibitory mechanism (Xu, 2012), the most active of this family being PACMA 31. This SMI has been shown to successfully inhibit PDI activity *in vitro* and shows promise as a cancer treatment *in vivo*.

6.1. Y393C-PDI-myc Saos-2 cells have a significantly lower viability compared to WT-PDI-myc transfected and non-transfected cells.

NT, WT-PDI-myc and Y393C-PDI-myc transfected Saos-2 were assessed for viability using an Orangu™ assay, as outlined in Chapter 2.2.5. Viability was calculated using the mean absorbance recorded over the three biological repeats in

95

each well row (1 - 5) as depicted in Figure 6.1. Absorbance is positively correlated with cell viability in this assay. The chemical structures of the irreversible PDI inhibitors 16F16 and PACMA 31 used in this chapter are shown in Figure 6.1B, with the disulphide inducing 'active' regions circled: chloroacetyl and propynoic acid moieties for 16F16 and PACMA 31 respectively. These regions block PDI's active site, therefore inhibiting its chaperone and oxidoreductase functions.

16F16　　　　　　　**PACMA31**
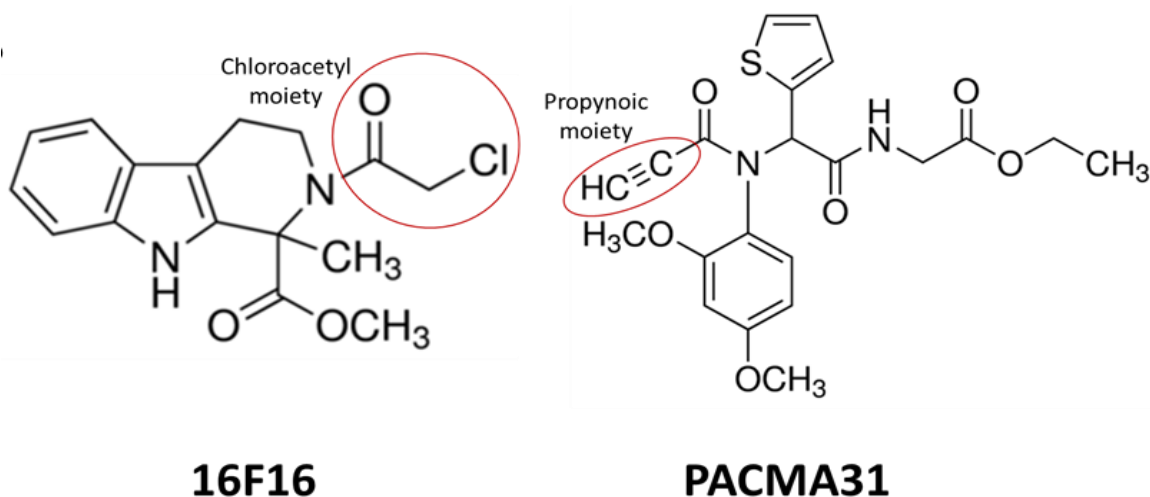
Figure 6.1. Chemical structures of the two PDI inhibitors used, with 'active' regions inducing inhibition of PDI's active site circled.

Figure 6.2 shows average cell viability for Y393C-PDI expressing cells and both negative and positive controls, in the absence of PDI inhibition.
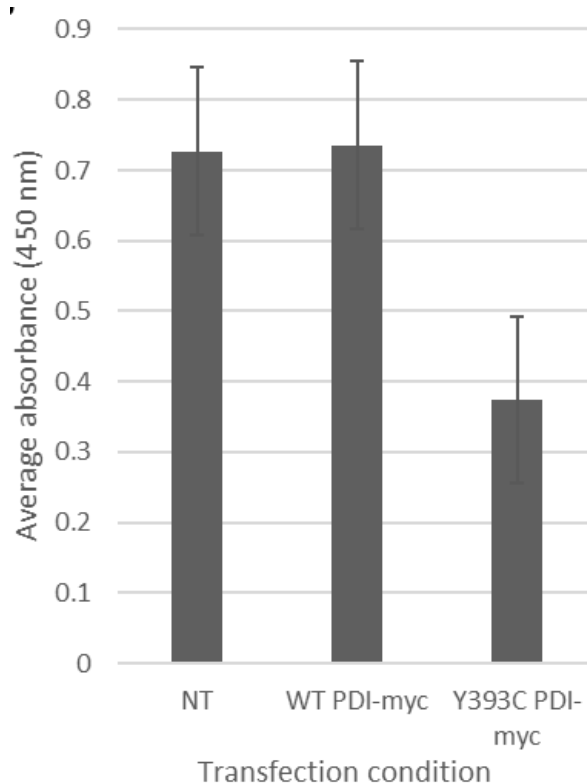
Figure 6.2. Y393C-PDI expressing cells have a lower average viability than wildtype transfected and non-transfected controls. Bar chart showing mean absorbance recorded in across all wells of untreated non-transfected, WT-PDI-myc, Y393C-PDI-myc by an Orangu™ assay for viability. Standard deviation around the mean (NT = 0.453; WT-PDI-myc = 0.052; Y393C-PDI-myc = 0.039) shown by error bars.

Figure 6.2 shows a significant decrease in cell viability for Y393C-PDI-myc transfected Saos-2 cells compared to both wild-type PDI conditions. As expected, there is no significant difference recorded between both non-transfected and wild-type PDI transfected cells. This demonstrates there are no significant detrimental effects of the transfection procedure on cell viability, concurrent with previous observations. An average absorbance of 0.3743 OD_{450} was recorded for Y393C-PDI-myc transfected cells, alongside 0.6271 OD_{450} and 0.6250 OD_{450} for NT and WT-PDI-myc conditions respectively. This data therefore suggests that there is an approximately 50% decrease in viability of cells transfected with Y393C-PDI-myc.

6.2. Y393C-PDI cells appear less affected by SMIs when compared to wild-type

To establish whether PDI inhibitors influence Y393C-PDI cell survival, viability experiments were performed using the microplate set up shown in Figure 6.1A, in the presence of PDI inhibitors shown in Figure 6.1B. These were used at increasing titrations of 0, 4, 6, 8 and 10 µM concentration and were added in triplicate to well rows 1 - 5 respectively, as shown in Figure 6.1A. As previously, average absorbance was taken across the three wells. The results of these experiments are shown in Figure 6.3. At 0 µM, there is a clear decrease in viability between wild-type PDI and Y393C-PDI cells, irrespective of inhibitor addition. This untreated condition acts as a technical repeat of Figure 6.1.

With increasing concentrations of both inhibitors, average viability decreases for both NT and WT-PDI-myc transfected cells. Both conditions follow a similar trend, as shown in Figure 6.3. Between 0 – 4 µM of 16F16 there is no change in wild-type viability, however from 4 – 10 µM there is a steady decrease to a final OD_{450} of 0.44 in non-transfected cells, and 0.46 in WT-PDI-myc. Conversely, treatment with PACMA 31 shows a larger decrease in viability between 0 – 4 µM, and a similarly steady decrease with subsequent increasing inhibitor concentrations.

Thus, there appears no significant difference between NT and WT conditions for each inhibitor concentration, inferred by overlapping standard deviation error bars for all wild-type PDI conditions. This is confirmed by a two-way analysis of Variance (ANOVA) the results of which are shown in supplementary data Table 9.3. A subsequent Bonferroni post-hoc test was conducted on the ANOVA results between non-transfected and WT-PDI-myc transfected cells, and Y393C-PDI-myc as shown

in Table 6.1 and 6.2, displaying the results for 16F16 and PACMA 31 inhibition respectively.
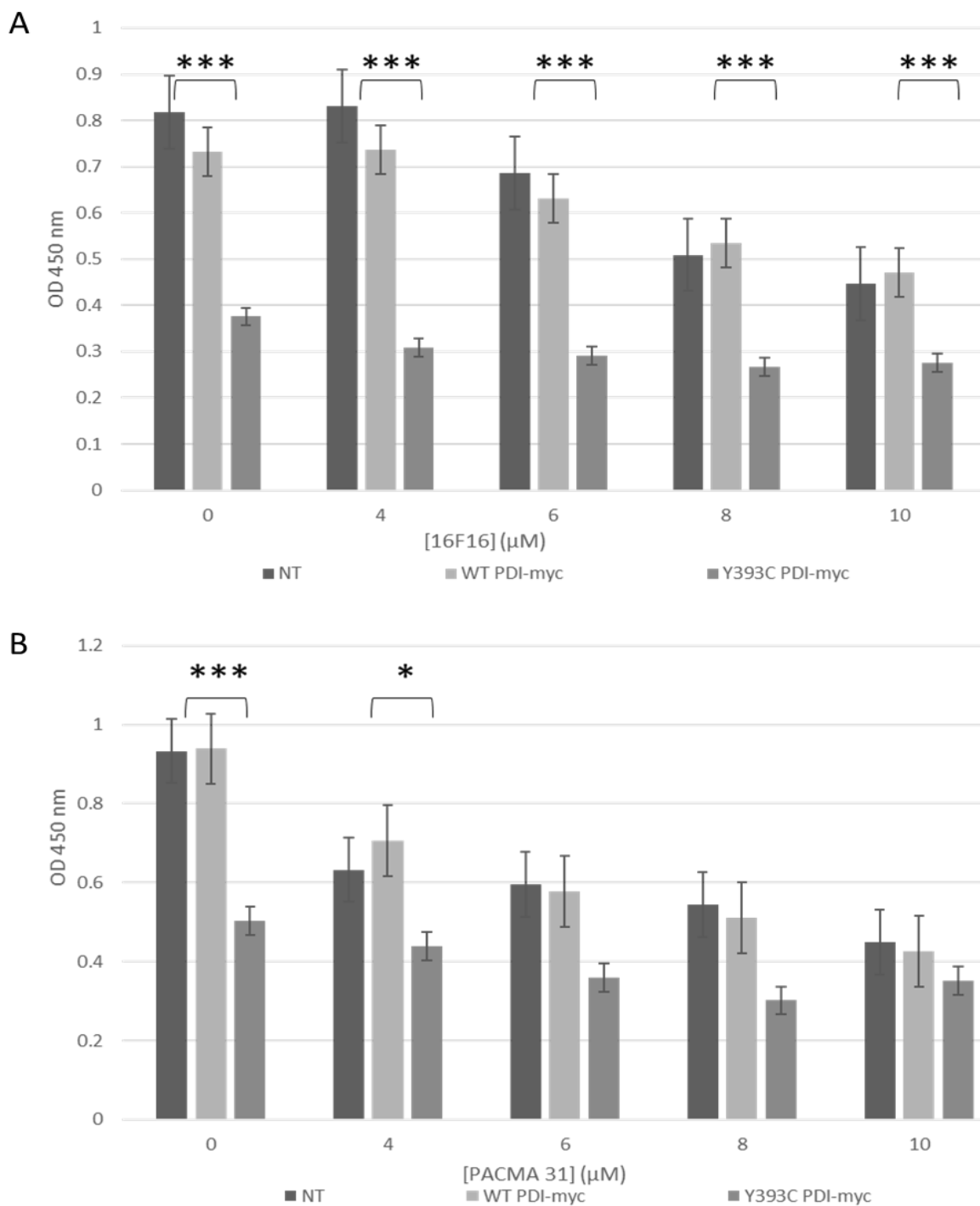
Figure 6.3. PDI inhibitors appear to be less effective against Y393C-PDI expressing cells than wild-type controls. Bar charts showing effects of 16F16-mediated (A) and PACMA 31-mediated (B) PDI inhibition on cell viability of NT, WT-PDI-myc and Y393C-PDI-myc transfected cells. Error bars show standard deviation around the mean. Two-way ANOVA significance for (P < 0.001) (***) and P > 0.05 (*) shown above. No significance detected between both NT and WT-PDI-myc transfected conditions.

Tables 6.1 and 6.2 show significant variation (p < 0.001) between both wild-type conditions and Y393C-PDI-myc transfected cells in the presence of 16F16 inhibition across all concentrations, and the lower concentrations (0 - 4 µM) of PACMA 31 as displayed on Figure 6.3A and in Tables 6.1 and 6.2.

Table 6.1. Results of statistical analysis against wild-type PDI conditions and Y393C-PDI-myc cells, in the presence of 16F16-mediated inhibition (Two-way ANOVA, Bonferroni post-hoc tests).

	Inhibitor concentration (µM)	t	P value	Significance
NT vs **Y393C**	0	13.04	P < 0.001	***
	4	14.33	P < 0.001	***
	6	10.81	P < 0.001	***
	8	6.634	P < 0.001	***
	10	4.724	P < 0.001	***
WT vs **Y393C**	0	10.71	P < 0.001	***
	4	11.71	P < 0.001	***
	6	9.302	P < 0.001	***
	8	7.347	P < 0.001	***
	10	5.364	P < 0.001	***

Table 6.2. Results of statistical analysis against wild-type PDI conditions and Y393C-PDI-myc cells, in the presence of PACMA 31-mediated inhibition (Two-way ANOVA, Bonferroni post-hoc tests).

	Inhibitor concentration (µM)	t	P value	Significance
NT vs **Y393C**	0	3.314	P < 0.05	*
	4	1.933	P > 0.05	ns
	6	2.733	P > 0.05	ns
	8	2.138	P > 0.05	ns
	10	0.576	P > 0.05	ns
WT vs **Y393C**	0	4.378	P < 0.001	***
	4	2.816	P < 0.05	*
	6	2.411	P > 0.05	ns
	8	2.231	P > 0.05	ns
	10	0.8591	P > 0.05	ns

Interestingly, Y393C-PDI-myc transfected cells respond differently to SMI inhibition than their wild-type counterparts, with a less drastic decrease in viability with increased inhibitor concentration, as displayed by Figure 6.3. They also show marginally different responses in the presence of each inhibitor. Data in Table 6.1 show strong variation (*** significance) between both wild-type PDI conditions and Y393C-PDI cell viability in the presence of 16F16. However, while treatment with PACMA 31 appears reflect the wild-type decreasing trend marginally more, there is no significant difference recorded between 6 – 10 µM for all conditions ($P > 0.05$), showing a viability 'plateau'. This is also reflected in the bar charts in Figure 6.3, which display this slight viability decrease for Y393C-PDI transfected wells treated with increasing concentrations PACMA 31. This is aside from the final concentration of 10 µM of inhibitor, in which there is a slight increase from 8 µM. Viability observed for 16F16 treated Y393C-PDI-myc cells appears unchanged when inhibitor is added, irrespective of increasing concentrations, as displayed by overlapping standard deviations shown by error bars.

This demonstrates that Y393C-PDI cells treated with PACMA 31 at 6 – 10 µM concentrations appear to display a statistically similar viability to wild-type. This also suggests that the effect of 16F16, if any, is not changed by changes in inhibitor concentration. This provides further evidence for the hypothesis that both inhibitors have a reduced impact on PDI inhibition in Y393C-PDI-myc cells, therefore resulting in less of a decrease in viability than expected from the wild-type.

6.3. Conclusion

The cell viability data in this chapter show that the expression of Y393C-PDI decreases cell viabiity when compared to wild-type PDI counterparts. Levels of viability can be reproduced significantly with the average of 15 wells considered; it is inferred that only the Y393C-PDI mutation influences viability, and not the transfection procedure itself. This suggests the Y393C mutation may effectively behave like a PDI inhibitor and compromise the protein's essential roles in the cell, leading to a reduction in cell viability.

Inhibition of PDI with 16F16 and PACMA 31 have significant effects on the viability of Saos-2 cells. Firstly, treatment with both inhibitors appears to generally increase cell death of wild-type PDI expressing cells, at a similar level. The addition of PACMA 31 results in a gradual decrease in absorbance from approximately 0.9

OD_{450} at 0 μM of inhibitor to 0.45 OD_{450} at 10 μM. This is also reflected in 16F16 treated cells. Inhibitor treated Y393C-PDI-myc cells display differing viability to wild-type, with slightly different responses between both inhibitors. In general, viability does not decrease significantly between concentrations, as was observed in wild-type PDI cells.

16F16 appears to have no significant impact on Y393C-PDI cell viability after 4 μM, which could be explained in two ways. Firstly, any changes in viability may be too small to be detected by the assay at such a low absorbance of 0.3 OD_{450}. However, the Orangu™ assay claims to have increased sensitivity compared to other common competitors (MTT, XTT, MTS), and should detect absorbance below this reading. Another potential explanation could that transfection efficiency is ~50% and all successfully transfected cells have died at this point. The nature of this result could be confirmed by the repetition of this experiment with stably transfected Y393C-PDI expressing cell lines. A more interesting theory may be that the Y393C-PDI inhibition is blocked in some way by the mutation, resulting in the inhibitors being unable to impede Y393C-PDI function, thus displaying little change in viability, regardless of inhibitor concentration.

The addition of PACMA 31 also shows less inhibition over the working concentrations in Y393C-PDI expressing cells: Y393C-PDI cells have a smaller decrease in OD_{450} between 0 - 10 μM of inhibitor than that of wild-type PDI conditions. There is also no statistical significance between each transfection condition at the same concentration after 6 μM. Therefore, this data infers that PACMA 31 has less effect on Y393C cells, resulting in a lack of inhibition which is not reflected in wild-type. Both inhibitors induce bonding between cysteine residues of PDI's active site, therefore the tyrosine to cysteine mutation implicated in CCS1 may disrupt the formation of these bonds, providing a potential explanation for these results.

Despite Table 6.1. showing significant differences between both wild-type conditions and Y393C-PDI in 16F16 treated cells, the t-test values follow the same trend as for PACMA 31; that of a lesser decrease in viability despite increasing concentration, as reflected on the graph. Given more repetition, this may result in the same trend of non-significant viability differences between wild-type and Y393C-PDI at higher inhibitor concentrations. This is as expected as both SMIs utilise the same inhibitory mechanism, therefore this is an interesting avenue to pursue.

7. INITIAL CHARACTERISATION OF PRIMARY COLE CARPENTER PATIENT FIBROBLASTS

Introduction:

The work in previous chapters has been undertaken with transiently transfected immortalised osteoblast and fibrosarcoma cell lines. However, cell lines may not maintain the same characteristics of their primary tissue counterparts through 'phenotypic drift' away from their supposed characteristics (Pan, 2009). This can result in atypical gene expression when cultured *in vitro,* that are not expressed in primary cells from the same tissue. Therefore, CCS fibroblasts derived from a patient containing the mutation were used to establish a platform for the analysis of Y393C-PDI function in the cell. The experiments presented in this chapter comprise monitoring fibroblast growth, imaging of fibroblasts with phase contrast microscopy, and immunofluorescence to understand PDI expression patterns.

7.1. Light microscopy of CCS patient derived fibroblasts shows varied growth patterns compared to control.

As expected, patient derived cell growth was slower than that of control fibroblasts. Figure 7.1 shows cells after 20 days of growth in a humidified incubator, with media changes every 24 hours for the first 10 days and then 48 hours for the next 10 days.

Control cells shown in Figure 7.1A reached approximately 80% confluency during this culture period, and demonstrated typical fibroblast growth; with most cells growing in the same orientation as their neighbours, as highlighted by the boxed section in panel A, then magnified in panel B. The cells also appear between 10 – 20 μm in width, with most displaying elongated cell bodies over 100 μm in length, calculated from the scale bars shown.

103
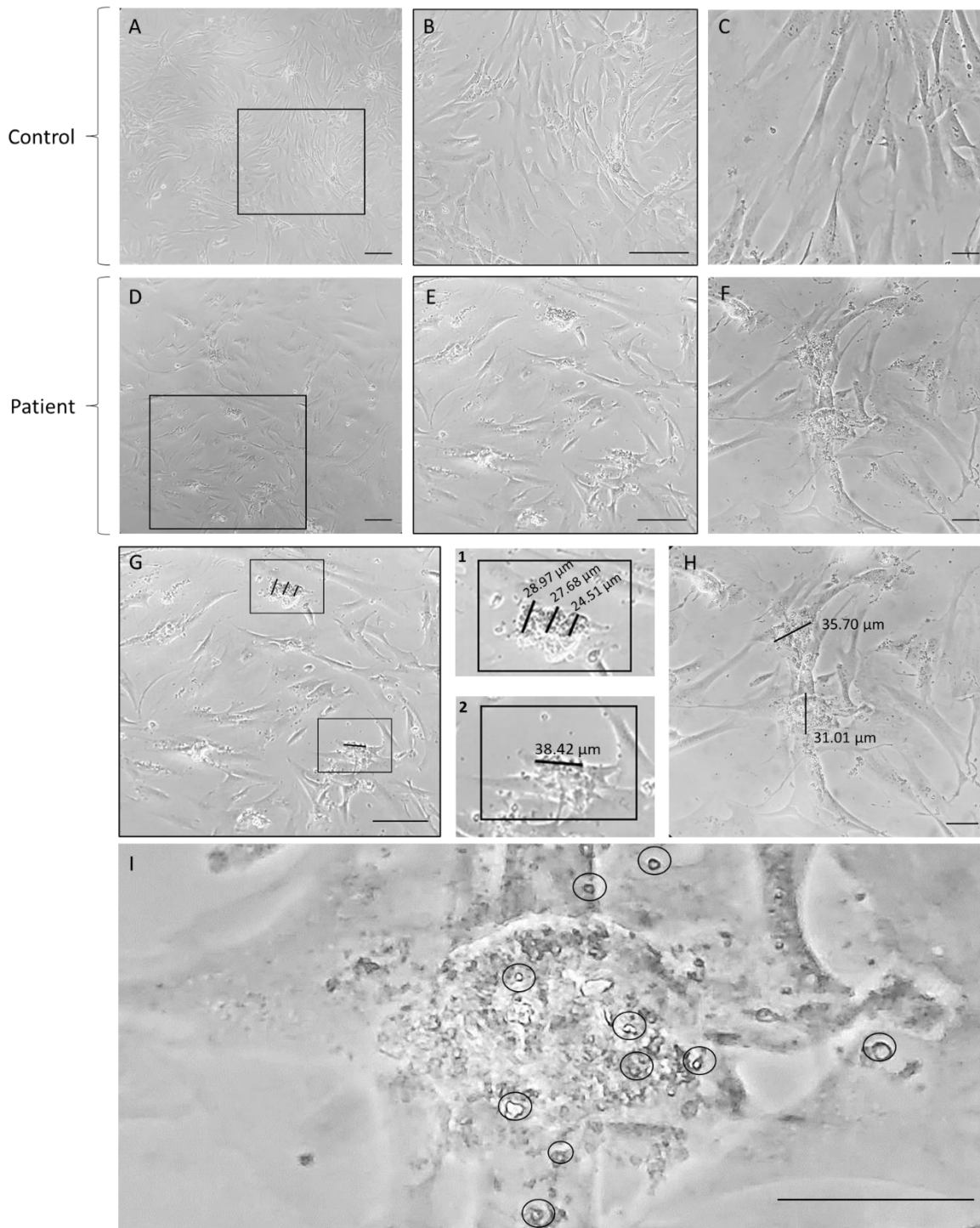
Figure 7.1. Phase contrast microscopy showing growth of control fibroblasts (panels A – C) and patient derived fibroblasts (panels D – F) whilst in culture. Panels B and E show magnified sections boxed in panels A and D respectively. Scale bars = 100 μm (A, B, D, E); 20 μm (C, F). Large extracellular objects observed in Panels E and F shown and measured in Panels G (1 and 2) and H. Scale bars equal 100 μm (G) and 20 μm (H). Panel I shows a magnification of the 31.01 μm object shown in H, with smaller constituents circled. Scale bar = 20 μm.

In contrast, fibroblasts derived from the patient display different growth patterns, as shown in Figure 7.1. There appears to be a larger variation in size between cells, and no evidence of directional growth like that of the controls, which may be a result

104

of the cells not reaching full confluency. Some extracellular granular masses were visible, as shown in Panels F - I which are not observed in the control culture.

Panels G, H and I shows these extracellular masses at a higher magnification. Panel G shows cells observed in panel E, of which two masses were chosen, magnified and measured in adjacent panels 1 and 2. There is some variation in object size as displayed by numbered panels and H, with a total mean diameter of 31.05 µm. Each large object appears to consist of smaller, broadly round granules measuring between 1.8 and 0.6 µm in size, as shown by 10 randomly chosen granules in Panel I circled. Each circled 'granule' was measured using ImageJ, giving a total mean diameter of 1.06 µm and a standard deviation of 0.36.

7.2. Immunofluorescence of CCS patient cells is concurrent with that of Y393C-PDI transfected cells
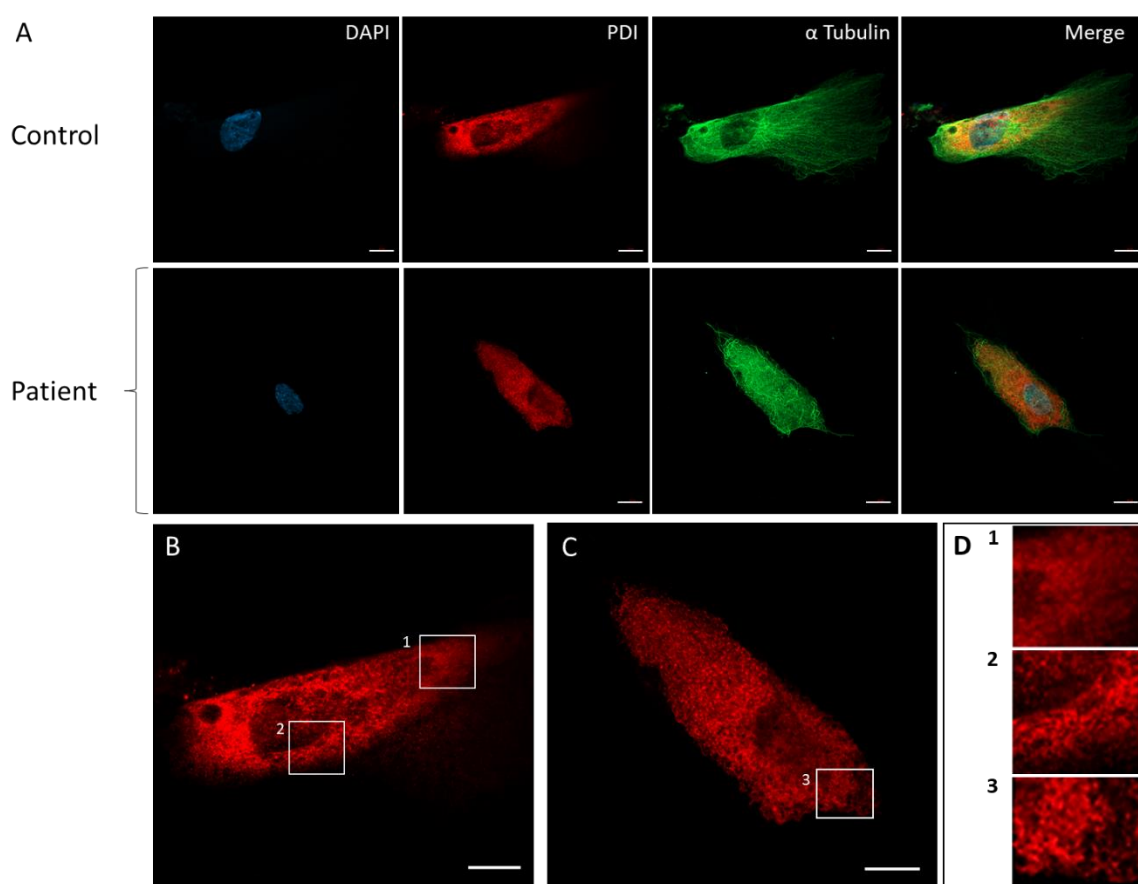
Figure 7.2. The tubular ER morphology observed in transfected cell lines is mirrored in patient-derived fibroblasts. (A) Immunofluorescence showing control and patient derived primary fibroblasts fixed, permeabilised and stained for PDI (594) and α tubulin (488). The PDI expression in control and patient cells is magnified in (B) and (C) respectively. (D) shows a comparison of ER morphologies observed in the previous panels, boxed (1 = sheet; 2 = tubular; 3 = tubular). Scale bar = 10 µm.

105

To detect the expression of PDI, patient and control cells were fixed, permeabilised and subjected to immunofluorescence, as shown in Figure 7.2 and Figure 7.3. As has been observed in previous chapters, transfected Y393C-PDI cells exhibit a more tubular ER, which is reflected in the distribution of PDI. Figure 7.2B and C show the ER from control and patient cells respectively, magnified to further observe the ultrastructure. Sections of both tubular and sheetlike ER are apparent in the control cell, which are boxed and further magnified in numbered panels D1 and D2. This is concordant with the ER morphologies previously observed in Chapter 3, showing areas of tubular and sheet-like ER within the same cell. The comparable patient cell shows a consistently tubular ER, as has been observed in Y393C-PDI expressing cell lines in this thesis.

The cells were co-stained with α tubulin which shows mostly polymerised microtubule structures in both cell types, which are distinct from the ER. This is concurrent with the previous observations of Y393C-PDI transfected cell lines. The patient derived cell displays a less directional and more disperse microtubule phenotype than the control, with filaments appearing curled and non-polarised.

To assess the relationship between collagen and lysosomes in CCS and control cells, collagen I and Lamp2b were stained in both cell types using immunofluorescence, shown in Figure 7.3. As seen previously in this thesis, cells expressing Y393C-PDI display fewer lysosomes, with some appearing abnormally large when compared to a wild-type control. Control cells containing wild-type PDI show the widely distributed, punctate staining expected from Lamp2b and demonstrate normal lysosome distribution throughout the cytoplasm. The merged channel images clearly show little colour overlap, therefore no colocalisation between lysosomes and collagen I.

However patient derived fibroblasts appear to demonstrate some colocalisation between Lamp2b and collagen I, as demonstrated in the yellow overlap areas of the bottom right panel. As observed previously, these organelles appear less abundant, but much larger than the typical lysosomes displayed in the control cells above.
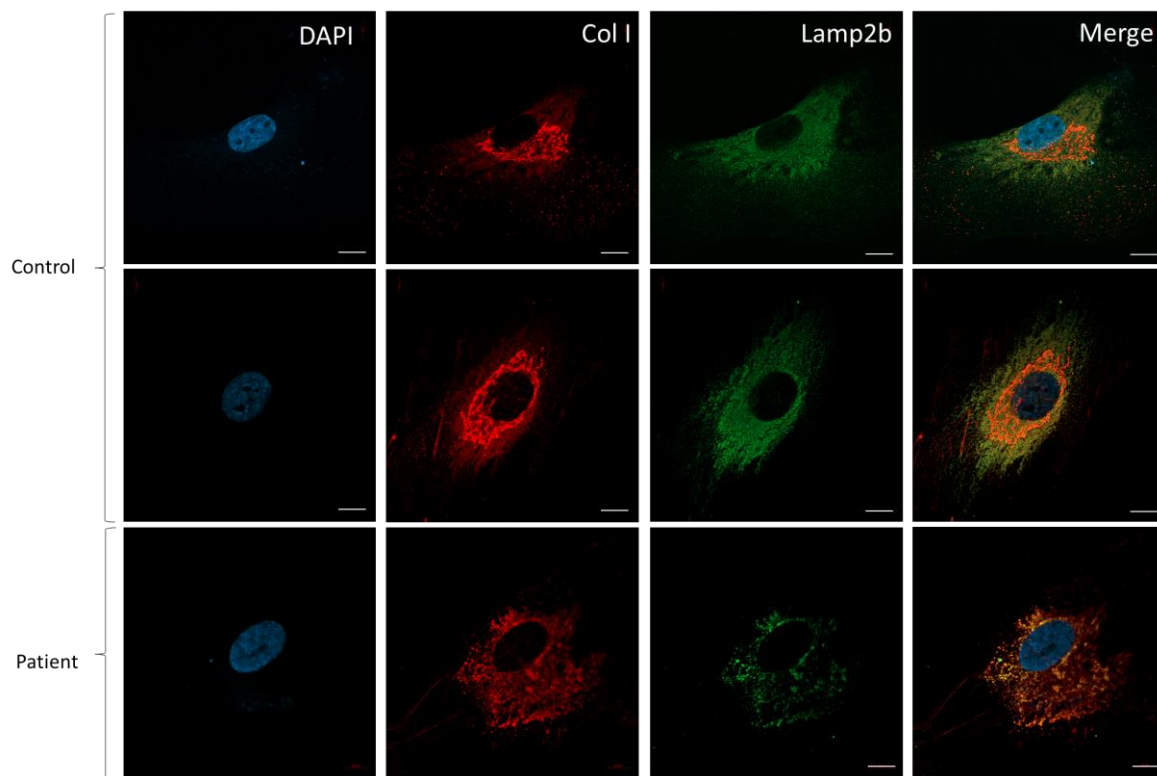
Figure 7.3. Control and patient derived fibroblasts co-stained with Collagen I (594) and Lamp2b (488) show abnormal colocalisation in patient derived cells. Scale bar = 10 µm.

To properly characterise the relationship between collagen production and lysosome morphology in patient-derived fibroblasts, further analysis for lysosomal size and location in respect to collagen was performed. Green (488) and red (594) channels were merged for cells shown in Figure 7.3, and 3D object mapping performed using ImageJ, the results of which are shown in Figure 7.4.

The control fibroblast in Figure 7.4A shows normally sized lysosomes which mostly appear distinct from collagen, as shown in the adjacent panel 1, circled. The associated surface maps for each channel are shown in panels 2 and 3, showing no clear relationship between lysosomes and collagen I distribution.

The corresponding patient cell is shown in Figure 7.4B, with magnified sections shown in panels 1 and 2. This shows abnormal distribution of both collagen and lysosomes, with the latter organelles appearing abnormally large, as seen in Y393C-PDI expressing cells in previous chapters. In general, there appears more colocalisation of collagen to lysosomes in the patient cell than the control, shown by the yellow objects circled in panel 1 and 2. However, there remains some lysosomes

distinct from collagen I which appear in green and are again circled in the magnified numbered panels in Figure 7.4 A1, B1 and B2, in both the control and patient cell.
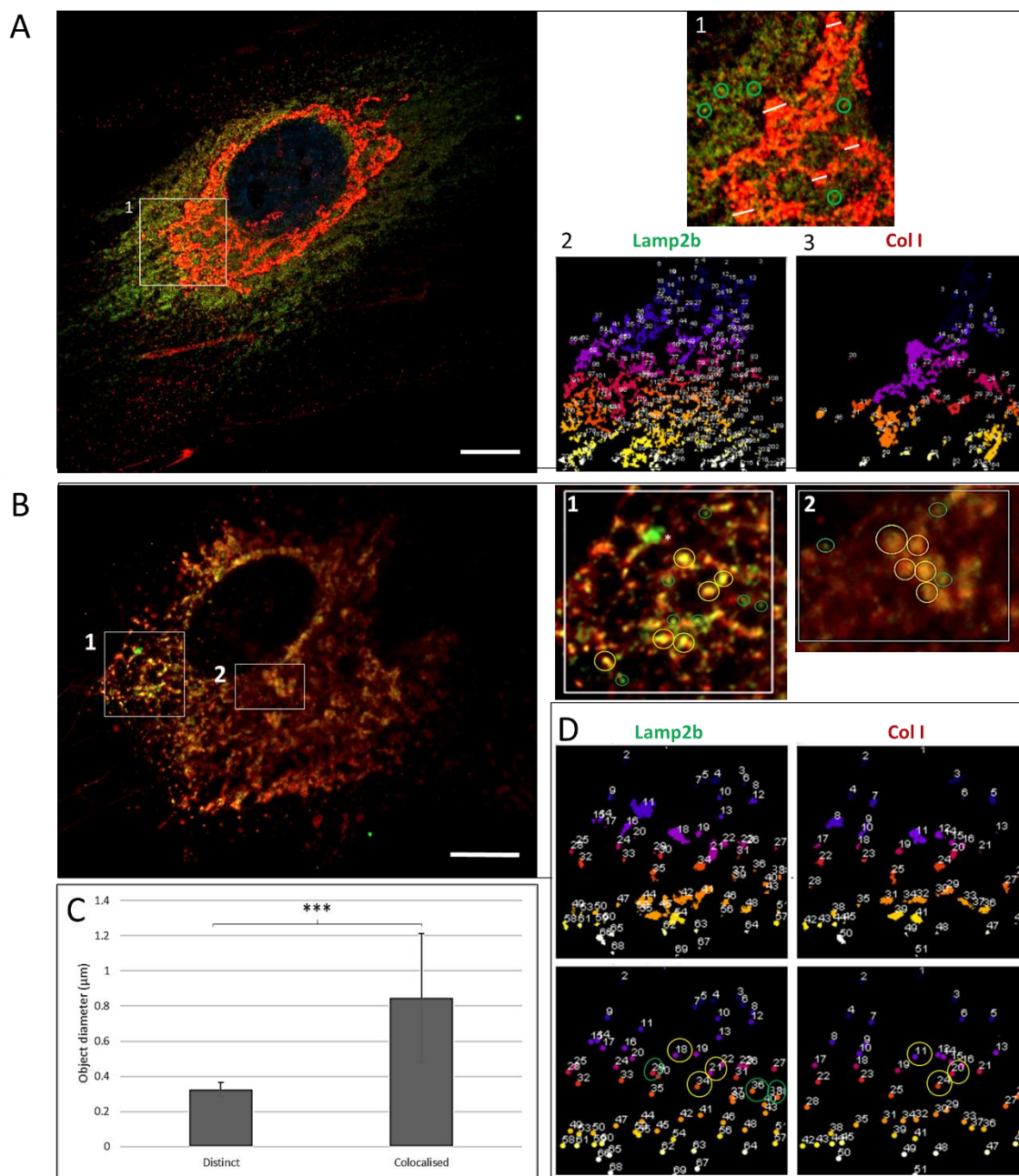
Figure 7.4. Post-acquisition analysis of lysosome distribution and colocalisation to collagen I from cells shown in Figure 7.3. Magnified collagen I and Lamp2b channel merges from (A) control and (B) patient cells as shown previously. Further magnified sections showing Lamp2b and collagen I structures in Panels A1 (control) and B1-2 (patient). A2-3 show surface maps for Lamp2b and collagen I signal respectively. (C) Bar graph showing mean object diameter of green (distinct) and yellow (colocalised) objects circled in panel B1 with standard deviation, and students T test significance level (***). (D) Top panels show 3D object surface maps for CCS1 Lamp2b and Collagen channels. Location maps shown below, with colocalised (yellow) and distinct (green) objects circled.

To compare lysosome size and colocalisation to collagen in CCS1 fibroblasts, 10 measurements across numbered panel B1 were taken for each 'distinct' (green) and 'colocalised' (yellow) object's diameter. The mean and standard deviations are shown as a bar chart in Figure 7.4C. This clearly highlights a significant difference between non-collagen associated lysosomes, and the colocalised lysosome sizes, with mean diameters of 0.32 μm and 0.84 μm respectively. Significance was further confirmed using a student's T-test which gave a t-statistic of 4.76 (p = 0.0002), showing statistical significance between these object sizes.

The colocalisation of these objects was further confirmed using the ImageJ 3D object mapping analysis. 69 Lamp2b and 51 Collagen I objects between 200 and 800 nm were detected in each channel shown in panel D. As expected, some of these objects appeared in both channel maps, with three examples labelled 18, 21, 34 and 11, 21, 24 respectively and circled in yellow on the location maps. Smaller objects are only detected in the Lamp2b (488) channel, with three examples circled in green and labelled 29, 36 and 38.

To establish if these large objects share the same surfaces, 3D surface maps generated for the channels are included above. This again reiterates the overlapping localisation in both channels for the large collagen I lysosomes. Both these observations are consistent with data presented in previously in Chapter 5; that lysosome morphology and distribution appears to be affected by the Cole Carpenter PDI Y393C mutation, and the abnormally large organelles show colocalisation to collagen I.

7.3. Conclusion

As expected from patient derived fibroblasts, and observed in Figure 7.1, their growth and doubling time was much slower than their control counterparts, achieving a lower overall confluency within their population despite growth media changes occurring at the same time as the control. They also showed a greater variation in cell volume and size, as displayed by the lower magnification images included in Figure 7.1. This may be a result of lower confluency, as the reduction in cell-cell communication and contact may have prevented them displaying the normal fibroblast formations observed in the controls. These characteristic fibroblast growth patterns include the unidirectionality of neighbouring control cells as seen in Figure 7.1 panel A, and the magnified section of panel B. Communication and

coordination between cells results in the characteristic 'whorl' formation present in the centre of panel A, which is typical of normally functioning fibroblasts (Helson, 1985). This growth pattern was not observed in any patient derived fibroblasts during the culture period.

Whilst the unidirectionality and 'whorl' formation tends to not occur in sub-confluent cells, another possibility is that the Cole Carpenter pathology may be inhibiting cell communication, causing a lack of cell-cell adherence and a rounder shape (Cai, 2012). This rounded phenotype is also reflected in cells undergoing apoptotic or necrotic cell death, which data in Chapter 6 suggests is abnormally high in Cole Carpenter cells. The patient fibroblasts appear to grow independently from each other and display large variation in size and area, suggesting cellular stress. The largest difference between patient and control cells as observed in Figure 7.1 is the existence of the extracellular, granular masses observed in the patient cells. These were distinctly larger than any cellular debris appearing in the control condition, suggesting a link to the Cole Carpenter phenotype of the patient derived cells. These objects seemed to be localised either on top of or next to existing cells. They also appeared between 20 and 40 μm in diameter, larger than the diameter of the neighbouring cells.

These granular masses appear to resemble apoptotic bodies and membrane blebbing when compared to the relevant literature (Bennet, 1995). Apoptotic bodies are small, membranous microvesicles produced by cells due to membrane blebbing upon programmed cell death. These tend to measure within the range of 0.8 - 5 μm but can vary in size and density (Crescitelli, 2013).

These microvesicles may arise from the larger masses, since their size fits with the individual 'blebs' observed. The higher magnification image in panel B further supports this point with one mass measuring 31 μm in size. However, the smaller constituents measure consistently between 1.8 and 0.6 μm, with a mean diameter of 1.06 μm of the 10 objects chosen in Figure 7.1 panel I. This is consistent with the size of apoptotic bodies as described in the literature, (Crescitelli, 2013; Akers, 2013). A decrease in cell viability, and thus a possible increase in apoptosis or necrosis have previously been observed in Y393C-PDI cells; the granules may be a visual indication of this process occurring in true Cole Carpenter cells.

Using immunofluorescence to stain for apoptotic markers, such as annexin V or intracellular caspases, would help determine whether CCS cells are undergoing apoptosis at a higher rate than control cells. Flow cytometry of early apoptosis markers such as annexin V compared to late pathway DNA fractionation (shown by positive signal peaks before cell cycle stage G1) would confirm apoptosis and retain these masses in the sample, which fixation may not (Koopman, 1994; Demidenko, 2008; Wlodkovic, 2009). The absence of these at the known timepoints in apoptotic cell death may suggest the necrotic cell death pathway has been taken instead (Kryso, 2008).

The lysosome and collagen I immunofluorescence of Cole Carpenter cells allow comparison of the intracellular processes occurring between both patient cells and Y393C-PDI transfected cells, alongside patient and control fibroblasts. This shows consistency in a gross stressed morphology in both patient and mutant transfected cells. Lamp2b lysosomal distribution appears consistent with the observations in Chapter 5, with large 'swollen' organelles appearing to colocalise with Collagen I, a finding not observed in control cells. This is further supported by the 3D object location and surface maps observed in Figure 7.4. These show smaller, more conventional lysosomes appear to be distinct from collagen I, in the green (488) channel. However, the atypically large and swollen organelles appear detected as the same object in both red (594) and green (488) channels as shown by the ImageJ surface maps, again inferring the colocalisation of lysosomes to Collagen I in Cole Carpenter cells. Another possibility explaining the colocalisation of collagen and Lamp2b in these large objects is this cell has undertaken a cell death pathway, which is suggested to be increased in CCS cells from Chapter 6 viability assays. These large objects could therefore represent the membrane blebbing process. Re-staining for e-cadherin or n-cadherin, or a fibroblast surface protein (1B10) would establish whether the cell membrane is still intact, thus confirm if these are true lysosomes, or a product of the apoptotic pathway (Goodpaster, 2008).

Unfortunately, no collagen I deposition was observed in control or Cole Carpenter cells, possibly due to ascorbate insufficiency. Future experiments to analyse the deposition of collagen with ascorbate supplementation over time, combined with the use of PDI inhibitors, will therefore be informative (Chan, 1990). Taken together, the data presented in this chapter align with the results observed in transfected Saos-2 osteoblasts and HT1080 fibrosarcoma cells. This also suggests that the intracellular

111

effects of Cole Carpenter syndrome investigated in this thesis holds across both fibroblast and osteoblast cell types.

8. DISCUSSION

The work in this thesis has characterised the molecular basis of Cole Carpenter syndrome in both transiently transfected fibrosarcoma and osteoblast-like cell lines, alongside patient derived primary fibroblasts. Immunoprecipitation and western blotting described in Chapter 4 were used to explore interactions involving the Y393C mutated PDI, and preliminary LC-MS/MS analysis has paved the way for identifying the nature of some potential interacting partners. Fixed and live cell imaging as shown in Chapter 5 shows the localisation of Y393C-PDI in the ER, and highlights possible downstream impacts of the mutation on both collagen and other intracellular systems and organelles.

8.1. Characterising the intracellular interactions of Y393C-PDI.

8.1.1. ER stress in Y393C PDI expressing cells

As presented in Figure 4.2, a single nucleotide polymorphism in P4HB results in the gain of a reactive cysteine residue at position 393. This residue is close by but not directly part of the catalytic CGHC motif of PDI's active site. It is possible this results in the formation of a disulphide bond between the mutated residue and that of Cys397 or Cys400, disrupting PDI's activity. Furthermore, the CCS1 mutation is suggested to result in a dysfunctional PDI as opposed to a non-functional PDI, meaning the chaperone activity of Y393C-PDI is not completely inhibited. This proposed inhibitory mechanism is similar to that of SMIs PACMA 31 and 16F16 which target the active site cysteines (Hoffman, 2010) and impair the redox activity of PDI. Y393C-PDI may still form a complex with the P4HA, however its capacity to catalyse the hydroxylation of proline residues is likely to be affected by the mutation. This provides support to the misfolded collagen hypothesis, resulting in the onset of ER stress, as proposed throughout this thesis, and first mentioned in Chapter 1.1.1.

Abnormally high ER stress has been confirmed in Cole Carpenter patient cells through the upregulation of ER resident heat shock protein and molecular chaperone HSP47 (Rauch, 2015; Ishida, 2011). In future work, confirming the upregulation of HSP47 in cells expressing transfected Y393C-PDI would provide useful quantitative confirmation that Y393C-PDI transfected cells exhibited the observed characteristics of primary patient cells. Testing for other markers known to be upregulated by the UPR such as Xbp-1, phosphorylated PERK, ATF6 or

113

calreticulin via western blot or qPCR would also provide insight into the UPR activity in Y393C-PDI cells, and which arms of this pathway show signs of compromise (Kouroku, 2007; Korfei, 2008; Fhlathartaigh, 2013).

Recent developments in the field have suggested that an increase in a tubular ER indicates the onset of ER stress (Lee, 2020; Mateus, 2018; Zheng, 2018). The cell biology and microscopy approaches taken in this thesis imply a more prevalent tubular ER in Y393C-PDI transfected cells, which may be indicative of a stress response. HT1080 cells showing the tubular and sheet-like ER states as shown in Figure 3.2A and B provide a baseline comparison as to the appearance of these structures by immunofluorescence. ER stress is usually caused by accumulation or aggregation of unfolded or misfolded proteins and would therefore result in proteotoxicity and the CCS phenotype.

Furthermore, immunofluorescence in both this thesis and the relevant literature shows a more vesicular pattern of Y393C-PDI in the ER, as observed by Rauch (2015), and replicated in Figure 5.1. This may point to the retention of PDI in ER-Golgi vesicles, as previously observed by Araujo (2017) or perhaps aggregation of large PDI complexes in ER compartments. The former condition would be confirmed by co-immunofluorescence for ER-Golgi vesicle proteins e.g., COPII. The latter suggestion may be related to the unconventionally large and stable PDI complexes observed in Chapter 4.

8.1.2. Y393C occurs in the essential a' domain and may result in multiple levels of improper PDI activity.

Improper activation of PDI, or abnormal intermolecular disulphides between other proteins, may result in the establishment of reduction resistant, high molecular weight PDI complexes. These are explored in PDI co-immunoprecipitation and western blotting experiments in Chapter 4.

PDI is activated from its extended monomeric form into stable dimers or larger oligomers by Zn^{2+}, resulting in the disulphide bridging of a or a' catalytically active cysteines to b' non-catalytically active residues (Soloyov, 2004). This allows it to function as a subunit of the C-P4H collagen chaperone complex (Koivunen, 2005). Therefore, the extra cysteine at position 393 in the a' domain may disrupt PDI activity through the placement of unconventional intramolecular disulphide bonds. This may

114

result in firstly active site inhibition, or secondly the assembly of unconventional PDI complexes via intermolecular bonds with other proteins. The latter scenario is equally as likely, owing to the solvent accessibility of the residue highlighted by the proximity of water molecules in Figure 4.2. This may explain the source of some of the large, reduction resistant complexes in Y393C-PDI transfected cells, as seen later in Chapter 4.

Experimental evidence shows that amino acid substitutions in PDI's b' peptide binding domain do not inhibit C-P4H assembly onto the procollagen constituent chains, however, mutations in the catalytically active a and a' domains do (Koivunen, 2005). The latter domain (a') contains residue 393 and is the recurring mutation in CCS. This further implies that this C-P4H assembly process has been disrupted by the mutation, resulting in unconventional interactions with other proteins that typically should not be complexing with PDI.

This gain of a cysteine residue disrupting PDI may impair its proper assembly into the C-P4H complex or result in improper protein folding activity. Alongside the impacts of a dysfunctional C-P4H complex, this disruption may therefore result in improperly or incompletely folded collagen aggregation in the ER, activating the UPR and resulting in the downstream effects observed in these cells. This abnormal activity is also highlighted in the abnormal inhibition responses exhibited by Y393C-PDI in Chapter 6.

8.2. Investigating the response of Y393C-PDI-myc cells to PDI inhibitors

8.2.1. PACMA 31 and 16F16 inhibition

Improper or impaired activity of PDI often leads to cellular apoptosis, due to its fundamental protein folding roles. This has made inhibiting PDI an effective target for cancer therapy using the actions of SMIs, like those used in Chapter 6 (Xu, 2012). PACMA 31 and 16F16 inhibit PDI activity by covalently interacting with the thiol groups of the Cys397 and Cys400 residues of the a' domain residing active site. This disrupts the formation of the intramolecular disulphide bonds between these residues and inhibits the activity of wild-type oxidised PDI, alongside altering the protein's secondary structure (Xiong, 2020; Xu, 2012). However, as shown by viability bar graphs and associated statistical analysis in Chapter 6, the inhibition of

Y393C-PDI results in little average cell viability change across all inhibitor concentrations, whereas wild-type PDI inhibition shows increased cell death as expected from the literature (Liu, 2015). This lack of change may imply unsuccessful PDI inhibition in these cells, to some extent. It may be that the proximity of Cys393 to the conventional reactive cysteines of PDI's active site impacts their function, and replicates the binding of an inhibitor, at least partially: Y393C-PDI may structurally resemble 16F16-modified wild-type PDI. This is one explanation for the unchanging cell viability of Y393C-PDI expressing cells irrespective of inhibitor concentrations, as observed in Chapter 6. Due to the lower initial viability of Y393C-PDI expressing cells, the situation may be more complex, therefore further repetition is required to confirm this.

This apparent self-inhibition supports the hypothesis that the accessibility or binding capacity of PDI to the C-P4H complex may be impacted by this mutation. This has major implications for PDI's role as part of this complex as the Y393C mutation may result in the complex being unable to form or forming incorrectly. The latter situation is more likely, as the procollagen triple helix produced by CCS1 osteoblasts is hypothesised to be misfolded, not completely unfolded, therefore suggesting there is some chaperoning activity of the C-P4H complex retained. Klappa et al. (2000) observed a strong correlation between effective C-P4H component assembly and client peptide binding; if a mutated PDI failed to form a functional C-P4H tetramer, this tended to result in unsuccessful client binding. This highlights the importance of PDI as both an independent enzyme and part of the C-P4H complex and suggests the Y393C mutation may have substantial consequences on the rest of this chaperoning complex. There is a possibility that one of the stable, high molecular weight complexes observed in Chapter 4 may pertain to this chaperone complex.

It must be remembered that these transfected cells are not wild-type PDI knockouts and express endogenous wild-type PDI alongside the transfected Y393C mutant. If the addition of inhibitor had no effect on Y393C-PDI, an overall decrease in cell viability would be observed, due to the catalytic activity of wild-type PDI being inhibited. This may explain the result of PACMA 31 inhibition where viability still decreases, but not at the extent of the wild-type PDI expressing cells.

When treated with 16F16, it appears that a characteristic of Y393C-PDI transfected cells offsets this decrease in viability, therefore resulting in a viability

plateau, as seen by the broadly unchanging viability of 16F16 treated Y393C-PDI-myc Saos-2. Since the mutation is the only changing variable between control and Y393C mutant, it is inferred this may be the cause of the offset. Treatment with 16F16 is known to have other off-target effects: it can inhibit Erp57/PDIA3, an ER chaperone essential for the proper folding of glycoproteins (Jessop, 2007; Xu, 2014; Kaneya, 2021). Conversely, these off-target effects may result in other chaperones being upregulated to compensate for PDI inhibition. This could potentially 'rescue' the activity of Y393C-PDI, resulting in a viability increase sufficient to offset the expected decrease. Xu (2012) also report the mechanism of action for 16F16 has not been fully confirmed yet, therefore perhaps 16F16 inhibition of the Cys397 and Cys400 active site differs slightly from that of PACMA31. This may allow successful assembly of PDI into the C-P4H complex or rescue the proper folding of collagen. Further repetition with these and other inhibitors is therefore required.

Statistical analysis by a two-way ANOVA and Bonferroni post-hoc test was conducted to further quantify significance of these viability changes. Data tables for this are included in Chapter 6 and in Supplementary Materials. In all inhibitor-dependant viability data n = 3, therefore more repetition is needed to confirm statistical significance, preferably with a stably expressing Y393C-PDI cell line, or patient derived primary cells. Repetition would also confirm if the differences observed between inhibitors are truly significant, since the trend in statistical t-values for 16F16 suggests a similar pattern to the pattern of PACMA 31 treatment.

This is preliminary evidence suggesting the potential partial restoration of correct PDI function in Y393C-PDI by 16F16 inhibition. However, as acknowledged above, more evidence is required to prove this, alongside more repetition required to determine whether this is also observed in PACMA 31 treatment, which is also known to target the same active site. Testing cell viability with other known PDI inhibitors, such as 1,3,5-triazine (RB-11-ca) and Phenylarsine oxide (PAO) would also be an interesting avenue to pursue. Both inhibitors are also assumed to target the active site cysteines of PDI, therefore reproducing the experiments with these molecules may help establish if Y393C-PDI is affected by other inhibitors which target the active site (Xu, 2014). However, whilst these may offer more evidence in support of the observed viability changes in Chapter 6, this data should be taken with caution: both these inhibitors demonstrate lower specificities to PDI than the

PACMA 31 and 16F16, therefore effects on viability may be a result of PDI-independent targeting (Xu, 2014).

8.2.2. The role of the PDI a' domain

PDI's activities within the ER are not limited to collagen folding, therefore there may be indirect, downstream effects on other proteins classed as its clients. PDI's oxidation, reduction and isomerisation allow disulphide bond formation and subsequent reshuffling on its target client (Schwaller, 2003). The catalytic a and a' domains of PDI mediate disulphide bond formation, whereas the b and b' domains dictate substrate binding. It has also been shown that the a and a' domains can function independently as simple oxidoreductases (Darby, 1998), a role which may also be affected by the Y393C mutation. Despite having distinct 'peptide-binding' and 'catalytically active' domains, larger peptides above 10 - 15 residues require all PDI sub-domains for proper client binding (Klappa, 1998). Therefore, when chaperoning large substrates such as the two pro-α1(I) chains and one pro-α2(I) which make up collagen I, the full and uninhibited a' domain is important for PDI's function.

Klappa (2000) reported that structural changes in the a' domain, such as the Y393C mutation, indirectly affect peptide binding to the non-catalytic b and b' domains. They also showed selective removal of the a' domain can restore binding activity. If future work could apply this to CCS, it may hold promise for the development of therapies to restore proper PDI activity, and treat Cole Carpenter syndrome, alongside other related disorders.

8.3. Y393C and WT PDI localisation within the cell

The immunofluorescence in Chapter 5 shows co-localisation of transfected Y393C-PDI-myc to wild-type PDI, displaying proper ER retention. This is as expected by the uninterrupted PDI C-terminal KDEL ER localisation sequence in the constitutively active constructs (Bottomley, 2001). This normal localisation of Y393C PDI to the ER is reflected in patient derived fibroblasts, and highlights the problem caused by this mutation. If endogenously expressed Y393C PDI is functioning incorrectly, translation should be ceased, or it should be degraded post-translationally by ER associated degradation (ERAD) or ER-to-lysosome associated degradation (ERLAD) (Fregno, 2019). This appears to not be the case, as Y393C-

PDI is still active in CCS1 patient cells. This is highlighted by the quantity of collagen production, and to some extent, secretion, being unaffected (Cole and Carpenter, 1987).

Y393C PDI transfected cells also appear to upregulate the production of endogenous PDI, as highlighted in the channel intensity histograms shown in Chapter 5. This is more apparent in Y393C-PDI transfected cells, but also WT-PDI-myc to an extent, suggesting this may be either linked to general increased protein production by the cell, or a result of the lipid-based transfection procedure upregulating chaperones as part of the stress induced UPR (Fiszer-Kierzkowska, 2011). Establishment of stable Y393C-PDI expressing cell lines to solve this issue would be an essential next stage for this project.

8.4 The onset of ER stress should activate the UPR

This lack of Y393C-PDI degradation may be a result of the hypothesised gain of dysfunction rather than loss of function caused by Y393C. This may imply PDI's chaperone and/or oxidoreductase roles may be maintained to an extent. On the other hand, this may point towards a defective UPR. Further experimentation is needed to establish if this system is compromised, such as western blotting or qPCR for the presence of UPR markers, as mentioned in Section 8.1.1.

If Y393C-PDI is detected to be functioning incorrectly, the cell should respond. This should occur through the UPR responding to stress caused by Y393C-PDI itself or the accumulation of its misfolded clients, or the induction of other degradation pathways. This may result in the attenuation of translation, proteasomal/lysosomal ERAD, or the upregulation of another compensatory chaperone to take its place (Hetz, 2018; Ishida, 2011), as displayed in the UPR pathway schematic of Figure 1.4.

Innate issues with resolving ER stress in CCS1 cells may explain the observed intracellular collagen accumulation, abnormal behaviour of lysosomes, and decreased viability of both Y393C-PDI-myc and patient cells. These issues may result in a failure to rescue misfolded collagen via the conventional UPR. As shown in Figure 1.4, the PERK arm of the ER stress response results in the transient attenuation of translation until ER stress can be resolved. This is an integral system relying on a complex cascade of protein interactions to resolve ER stress and

restore cellular homeostasis and is partially dependant on the proper functioning of PDI. Oxidised PDI activates this arm of the UPR through its oxidoreductase activity which may be impaired in the Y393C mutant (Kranz, 2017). This is highlighted in Figure 1.5. showing the redox cycle of PDI which results in the subsequent activation of PERK. Therefore, if the unconventional, high molecular weight complexes containing Y393C-PDI observed in Chapter 4 trap PDI, this activation may not occur. This would leave translation unaffected, despite the presence of ER stress, and result in a defective UPR.

The observation of increased and unresolved ER stress by Rauch (2015) may potentially lead to a decrease in cell viability, as was observed in Chapter 6. The cell's failure to clear dysfunctional collagen I via the UPR may result in downstream effects on other protein degradation systems such as lysosomal autophagy, as investigated in this project.

8.5. Upregulating the UPR may help or hinder collagen misfolding.

8.5.1. PDI and the UPR

PDI's redox activation cycle is modulated by ERp57, yet it can also itself oxidise ERp57, alongside others such as ERp47 and P5 (Araki et al., 2013; Oka et al., 2015). Of the approximately 20 human PDIs, a number including ERp47 and P5 are disulphide isomerase chaperones which can be upregulated by the PERK arm of the UPR (Hettinghouse, 2018). Therefore, alongside its other role as a collagen chaperone in the C-P4H complex, PDI and its electron donor Ero1α act as an essential regulatory hub for the redox states of other ER resident chaperones (Araki, 2013). This role may be affected by Y393C, thus indirectly contribute to the CCS1 phenotypes observed in this thesis.
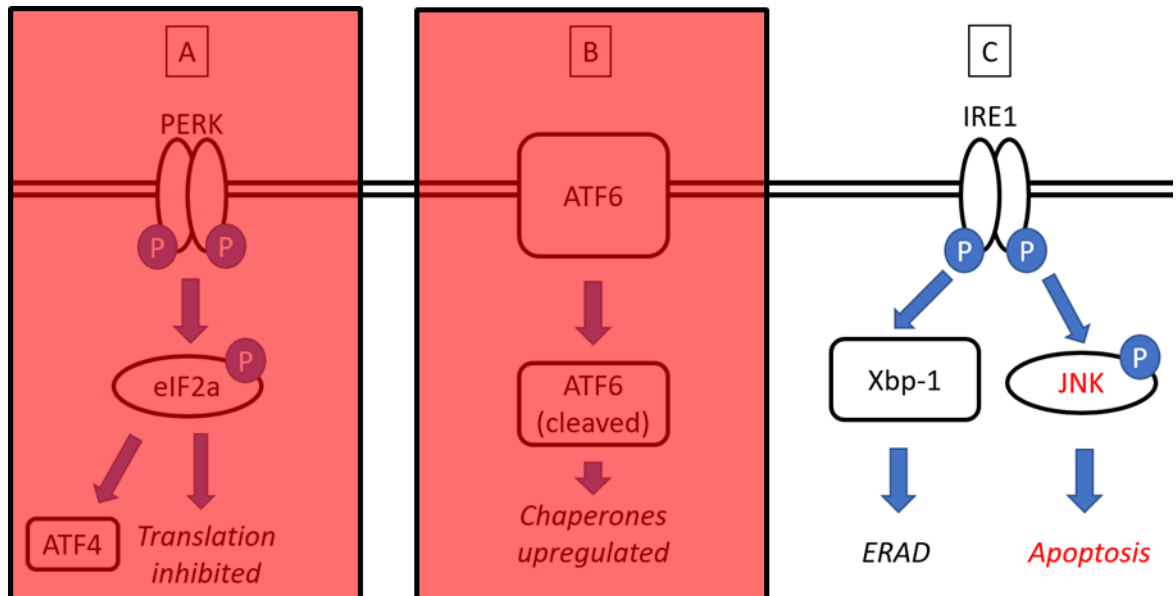
Figure 8.1. Modified Figure 1.4 showing PDI has crucial roles in the activation and execution of pathways A and B of the UPR. The Y393C-PDI mutation could therefore compromise the progression of these pathways.

Given the HSP47 upregulation shown by Rauch (2015), alongside the tubular ER observed in transfected cells in Chapter 5 and patient fibroblasts in Chapter 7, it is suggested that the UPR should be upregulated in these cells. However, if activation of the PERK arm (Figure 8.1, labelled A) is affected by the Y393C-PDI mutation, then this leaves only ATF6-mediated chaperone upregulation, and IRE1 to activate ERAD through the transcription factor Xbp-1, or apoptosis.

Cleaved ATF6 results in the upregulation of ER chaperones such as calnexin, calreticulin and ERp57/PDIA3 alongside PDI (Zhao, 2019). However, in Cole Carpenter cells, the upregulation of Y393C-PDI to assist with the folding of aggregated collagen would not rescue the homeostasis of the ER, but instead propagate the issue. It has also been shown that other chaperones are unable to compensate for PDI activity in procollagen folding (Rutkevich, 2010). This includes the collagen specific chaperone HSP47, meaning PDI-dependant chaperoning of the triple helix is likely to not occur. It has been suggested that instead of compensatory collagen folding mechanisms, HSP47 and PDI compete for collagen I binding, but have distinct roles in the triple helix biosynthesis (Hosokawa, 2000). Using immunofluorescence to visualise the cellular localisation of the upregulated HSP47 and Y393C-PDI and their substrate collagen would provide interesting follow up data, and perhaps determine if HSP47 binding to collagen increases in the presence of Y393C-PDI.

8.5.2. Failure to rescue unfolded procollagen or resolve the ER stress is likely to result in apoptosis

The upregulation of mis-functioning PDI, or non-compensatory chaperones such as HSP47 therefore could prevent the ATF6-mediated chaperone upregulation from rescuing the misfolded collagen (Figure 8.1, labelled B). This would leave only the final IRE1 pathway (C) to resolve ER stress. IRE1 activation can occur by HSP47 by displacing BiP, which maintains IRE1 in its inactive form. This then results in the subsequent dimerization of IRE1, activating the transcription factor spliced X-box protein 1 (Xbp-1) to promote ER associated protein degradation (Acosta-Alvear, 2007). The upregulation of HSP47 observed by Rauch (2015) implies this pathway is, to some extent, followed in CCS1 cells.

However, these IRE1 homodimers also contain domains which can signal the activation of the JNK protein kinases pathway to apoptosis, if ER stress is unresolved for a sufficient time (Lee, 2011). Given the possibility that two of the above pathways may be compromised due to the erroneous activity of Y393C-PDI, this time threshold may be met, therefore the cell undergoes apoptosis. This would lead to the significant decrease in cell viability observed in Chapter 6.

8.6. Intracellular production of collagen by Y393C-PDI osteoblasts.

Collagen production, secretion and deposition are linked, and highly complex cellular processes. As observed in Chapter 5.2, the intracellular distribution and quantity of collagen production appears normal between both wildtype and Y393C-PDI expressing osteoblasts. This reiterates the observation earlier described by Cole and Carpenter, suggesting variation in collagen production is unaffected by the Y393C mutation (Cole and Carpenter, 1987). This would be further confirmed quantitatively by western blotting for collagen I, since determining variation in protein production using immunofluorescence must be taken cautiously, due to horizontal antibody crosslinking and the single plane view.

After being secreted into the extracellular space by osteoblasts, collagens assemble into higher-order polymers termed collagen fibrils during the process of bone mineralisation (Buckley, 2012). These fibrils are thin structures of roughly 20 – 300 nm in diameter (Silver, 1992; Bancelin, 2014), and can form large matrix structures as shown in Figure 5.3. Deposition of collagen was observed in both non transfected

and wild-type transfected osteoblasts, whilst none was observed in Y393C-PDI transfected cells. This suggests that misfolded collagen may be retained in the ER of Saos-2 cells, with the intent to be degraded (Izawa, 2012). Quantification of collagen by an enzyme-linked immunosorbent assay (ELISA) or similar assay over a time course would be required to properly investigate whether deposition is significantly affected in CCS1.

8.6.2. Collagen secretion does not necessarily equate to deposition.

Interestingly, Balasubramanian (2018) reported secretion of collagen was observed in CCS fibroblasts, however at lower levels than that of control cells. This may suggest that the deposition process is not completely impaired in patient fibroblasts, and nod towards osteoblasts having increased reliance on PDI for procollagen folding than fibroblasts, resulting in the bone-specific severity of CCS. On the other hand, this observation may relate to misfolding-associated protein secretion, rather than deposition, to dispose of aberrant proteins in the absence of sufficient degradation post-UPR. This process was observed to protect proteostasis during proteosome dysfunction by Lee (2016) and may be a downstream effect of an impaired UPR.

Interestingly, in experiments presented in this thesis, slightly more deposition was observed across fields of view by wild-type PDI transfected cells. This is potentially due to the additional translation of collagen in wild-type PDI-myc transfected cells, increasing collagen folding yield (Todd, 1996), therefore resulting in increased exocytosis and deposition of the produced protein.

8.7. Collagen in Cole Carpenter cells appears to colocalise with abnormally behaving lysosomes.

8.7.1. Collagen I co-localises with lysosomes in Y393C PDI transfected osteoblasts, and patient derived fibroblasts

Lysosomes are small, cytosolic organelles between 50 - 500 nm in size (Alberts, 1984), and influence the quality control for newly synthesised procollagen molecules through a process known as 'autophagy', thereby influencing ER homeostasis (Settembre, 2018). Autophagy is an intracellular waste degradation system coordinated by the lysosomes to remove potential causes of cellular and ER stress,

one of which is misfolded proteins. The process consists of several sequential steps including sequestration of the material concerned, transport to lysosomes, degradation, and utilization or exocytosis of degradation products (Mizushima, 2007). In addition, the transcription of collagen genes has been discovered to be modulated depending on lysosomal autophagy (Settembre, 2018). This suggests translation may in part be regulated through this system, and the activity of mammalian Target Of Rapamycin Complex 1 (mTORC1). This further highlights the lysosomes as key players in the regulation of collagen production and subsequent secretion, supporting ER quality control systems with their own. Therefore, it is to be expected that an aggregation of unfolded or misfolded protein may have downstream effects on the functioning of this system, especially if the ER mediated UPR is partially compromised.

Data shown in Chapters 4 and 6 show other differences between Collagen I distribution in control and Y393C-PDI cells, with the latter appearing to show increased colocalisation of collagen I to abnormally large lysosomes, as stained for by Lamp2b. These differences are also observed between patient and control fibroblasts as shown by immunofluorescence in Chapter 7, and suggests collagen I which leaves the ER is picked up by lysosomes, likely as a result of improper folding. These lysosomes also appear abnormally 'swollen', which may indicate large volumes of internalised misfolded collagen. This swollen lysosome phenomenon is also reflected in other ER-stress related disorders, such as iPSC neurons displaying an enlarged and impaired lysosomal compartment as a result of a common Parkinson's disease mutation (Fernandes, 2016), alongside classical lysosomal storage disorders (Johnson, 2013).

8.7.2. Abnormally large lysosomes may exhibit loss of motility and autophagic function.

Data presented in this thesis show apparent changes in lysosome size, number and inferred motility in Y393C-PDI cells. This suggests atypical activity of this system, and a failure to fully remove or degrade misfolded collagen in Cole Carpenter cells, at the rate required to resolve ER stress (de Araujio, 2020). The 'swollen' size of these structures may be a result of large volumes of protein to be cleared, and the subsequent overwhelming of the system, resulting in a loss of motility (Martinez, 2007). This negative relationship between size and motility is inferred by live cell

imaging in Chapter 5, supporting the notion of cytosolic 'drag force' exerted on these organelles. This force has been suggested to influence both their diffusion and microtubule mediated active transport translocation (Martinez, 2007). This enlarged lysosomal phenotype, coupled with a decrease in lysosomal movement, may result in the inefficient clearance of misfolded, intracellular collagen in Cole Carpenter cells.

As stated above, lysosome size matters (de Araujio, 2020), but also the number of these organelles in a cell can indicate the disruption of intracellular homeostasis and the onset of ER stress. Interestingly, cellular and ER stress has been known to both increase and decrease lysosome frequency in different tissues. This potentially results from differing demands on the waste clearance by these organelles in conjunction with ER stress (Nakashima, 2019; Mahanty, 2019).

In pathologies where the lysosomes are not directly affected, one would expect lysosome frequency to increase due to onset of cellular stress. However, when lysosome biogenesis or function has itself been compromised, their numbers would be expected to decrease. In Cole Carpenter cells their numbers appear to decrease, demonstrated by both anti-Lamp2b and LysoTracker™ markers. While there is no evidence of compromising lysosomal mutations in Cole Carpenter disease, misfolded collagen aggregation may result in increased waste clearance demand that cannot be met by the osteoblasts. The consequential increase in ER stress has already been shown to decrease lysosome numbers in other bone cells (Nakashima, 2019). The proteotoxicity brought upon by misfolded collagen may result in larger, yet fewer lysosomes budding off the trans-Golgi network which are less motile throughout the cytoplasm. There also appears some atypical collagen I immunofluorescent staining occurring outside these organelles, again suggesting functional capacity overload, resulting in ineffective protein clearance, thus further propagating ER stress.

8.7.3. The microtubule cytoskeleton appears unaffected by the Y393C mutation

The microtubule cytoskeleton is integral to the effective trafficking of lysosomes and their role in autophagy (Webb, 2004). However, microtubules did not appear affected in Y393C-PDI cells, as highlighted in Chapter 5. Any changes are assumed to be a result of the delicate nature of the tubule presenting variation when prepared

125

using different fixative methods. Paraformaldehyde fixation resulted in a seemingly complete network breakdown, however when cells were fixed with 'Fixative B', as shown in Chapter 5, this variation was removed. Literature suggests that formaldehyde fixation does not preserve microtubules at the ultrastructural level as effectively as other methods of preparation (Forer, 1976), therefore explaining this result.

To summarise, collagen colocalisation to lysosomes in osteoblasts provides initial evidence to underpin two aspects of the Cole Carpenter phenotype. Firstly, the bone-specific severity of CCS may arise from a greater importance of PDI in bone Collagen I folding, and secondly the downstream effects of ER stress on the lysosomes may propagate the problems of the disease.

8.8. The Cole Carpenter phenotype may arise from an osteon-specific reliance on collagen I to maintain structural integrity.

It is known that other organs aside from bone are mildly affected in Cole Carpenter syndrome, the most notable being that of the cartilaginous vocal cords, resulting in patients having a high-pitched, nasally voice (Balasubramanian, 2019, personal correspondence). This bone-specific severity brings into question the differences between collagen production and distribution in the formation of bone tissues, compared to those of the rest of the body.

Collagen type I is arranged in the classic triple helices shown in Figure 1.6 (Berillis, 2013). These helices are first staggered axially into collagen fibrils, which are then bundled together to form the collagen fibres (Shoulders and Raines. 2009). To generate bone in a healthy individual, the mineralization of new osteoid occurs in continuation of the existing ECM upon which the newly synthesized Collagen I is deposited by the osteoblasts (Murshed, 2018). As such, quality control of the initial collagen triple helix formation is integral to ensuring these higher order structures form properly. It has been hypothesised that the Cole Carpenter phenotype occurs from incorrectly formed collagenous ECM, rather than complete inhibition of collagen secretion (Balasubramanian, 2018). Therefore, the misfolded collagen I fibres produced by Y393C-PDI expressing cells may form dysfunctional or non-functional ECM, compromising the structural integrity of the bone. A decellularization procedure on a CCS patient tissue sample, or that of primary cells cultured in a 3D scaffold would confirm the quality of deposited ECM, and whether
126

secretion observed by Balasubramanian is true collagen deposition, or removal of the misfolded procollagen.

Collagen's differing roles in structural integrity within tissues may suggest another reason behind the predominantly bone specific CCS phenotype. Deposited collagen fibres form the structural and mechanical scaffold of bone, alongside skin, tendons, cornea, blood vessel walls and other connective tissues and represent more than 90% of the organic matrix of bone (Makareeva, 2014; Miller, 1984). As bone tissue relies on rigidity and stiffness more than these other tissues, the structural role of Collagen I may be more important in building and maintaining the skeleton. It is known that additional maturation of collagen in bone is known to occur, contributing to structural stability (Viguet-Carrin, 2006). Therefore, it is to be expected that mutations affecting collagen formation may have more serious consequences in bone than elsewhere in the body, as illustrated by other types of osteogenesis imperfecta. This is particularly apparent in Ehlers–Danlos syndromes, which affect the structural integrity of connective tissue and display skin specific phenotypes (Karsdal, 2019; Steinmann, 2002). Furthermore, collagen I is often found alongside collagen III, which are both major components of superficial and deep layers of the *lamina propria* tissue of the vocal cords (Tateya, 2006). This possibly explains the vocal phenotype observed in the Cole Carpenter patient by Balasubramanian.

Essentially, it can be assumed all tissues of the patient's body are affected by the misfolding of collagen, as highlighted in other cartilaginous tissues. As observed in other OI's, the effects of misfolded collagen appear more severe in bone, potentially due to increased reliance on PDI as a collagen chaperone, and collagen itself as a structural protein (Forlino, 2016). The combination of these factors therefore may result in the severely brittle bone of CCS and explain why there are fewer implications on skin or hair tissue.

8.9. Transfected PDI-Y393C cells as a model for primary patient phenotypes.

Replicating the Cole Carpenter phenotype required the design of both wild-type and Y393C mutant PDI tagged constructs, as seen in Chapter 4. These were then transiently transfected into immortalised cell lines HT1080 and Saos-2 to reproduce the effects of the PDI mutation. Comparison between immunofluorescence of

patient cells as shown in Chapter 7 and the Y393C-PDI transfected cells shows the characteristics of PDI, Lamp2b and α tubulin are reproduced in both primary and immortalised cells.

There were some differences in lysosomal activity observed between HT1080 fibroblasts and Saos-2 osteoblasts, inferring different responses to the Y393C-PDI mutation in the relevant tissues. This may be explained by the vast variation in lysosomal distribution and morphology in wild-type cells from different tissues (de Araujio, 2020; Nabavi, 2008). It has been postulated that osteoblast lysosomes have key roles in the mineralisation of bone and the secretion of calcium phosphate to form osteoid, therefore this additional function may result in an increase in organelle frequency within these cells (Iwayama, 2019). This was observed by a much higher lysosome count in wild-type Saos-2 than HT1080 cells in immunofluorescence displayed in Chapter 5 of this thesis, alongside live cell imaging of the organelles using LysoTracker-Red^{TM}.

The responses of these cell lines to Y393C-PDI expression were taken cautiously, since cell lines often lose characteristics present in their primary cell counterparts. This can occur due to phenotypic drift through immortalisation and excessive passaging, the latter of which was mitigated as much as possible to reduce possible detrimental effects. Whilst the efficiency of collagen deposition in patient fibroblasts is still to be confirmed, the existence of abundant cytoplasmic vesicles in Figure 7.3. suggests the quantity of collagen production is unaffected, as observed by Rauch (2015). This is evidence to show the expected phenotype of the primary patient cells from the literature is replicated in this culture.

8.10. Primary patient fibroblast growth patterns provide future avenues for investigation into the CCS phenotype

Transiently transfected wild-type and Y393C-PDI-myc cells were compared to primary fibroblasts derived from both a Cole Carpenter patient and an associated positive control. As described in Chapter 7, both cultures were maintained under identical conditions, with media changes at regular intervals. Alongside establishing the cells in culture and minimising cellular stress due to extraneous factors, this enabled accurate comparison between control and CCS cells.

In general, patient fibroblasts had tubular ER characteristics that may be indicative of ER stress. The lysosomes of the patient cells also appeared swollen and deformed, and colocalised with the production of collagen I in the cell. This is consistent with data shown in Chapter 5, and further shows that the transfected osteoblast-like Saos-2 are a useful model cell line to study the biology of CCS.

Some interesting observations came from phase contrast imaging of the cells in culture, in which large, extracellular masses were observed compared to control cells. These appeared 'granular' in composition, and whilst the total structure measured between 20 - 40 μm across, the smaller granules appear to have a mean diameter of 1.6 μm. This size is concordant with apoptotic bodies and microvesicles as described in the relevant literature (Crescitelli, 2013; Akers, 2013), suggesting these masses are clumps of apoptotic cells or debris.

Small levels of apoptosis are expected to be seen in all cells in culture, especially non-immortalised, primary cells (Kamp, 2005). However, the number of these bodies observed in the Cole Carpenter patient culture exceeded those observed in the control fibroblasts. Again, this is consistent with the cell viability data presented in Chapter 6, and implies the apoptotic pathway is followed in Cole Carpenter cells more frequently than control cells. This may also explain the characteristic short stature of the Cole Carpenter patient; Mancilla et al. (1998) report that activating mutations in fibroblast growth factor receptor 3 (FGFR3) result in mass apoptosis of cells. This has also been linked to the onset of several skeletal dysplasias (Rousseau, 1994; Bonaventure, 1996). This subsequent apoptosis may reflect the granular masses observed in the phase contrast images of Chapter 7, and therefore result in the short stature and brittle bone phenotype of CCS.

Observation of cell death in cultured patient osteoblasts would infer apoptotic pathways are upregulated in osteoid producing bone cells, alongside the presence of apoptotic markers in fixed or live cell imaging which would confirm this theory. These could include staining for early-stage apoptotic marker cleaved caspase 3 (cl3) or performing a late-stage apoptotic marker assay for Terminal deoxynucleotidyl transferase dUTP nick end labelling (TUNEL). If these experiments showed an increase in apoptosis, it would offer considerable support to the hypothesis that increased osteoblast cell death may result in the brittle bone phenotype observed in the patient.

129

8.11. Future Investigations

Y393C PDI could be tested *in vivo* using a gene complementation approach in model organisms, or the production of wild-type PDI knockout osteoblasts expressing the Y393C mutant (Miura, 2008; Zhang, 2002). *In vitro* studies may further determine the chaperoning ability of Y393C-PDI e.g., using a denatured polypeptide substrate (Jaenicke, 1993; Hiller, 2021). This would establish the effects of Y393C-PDI on the quality control mechanisms of the ER, and whether it is able to bind collagen when not in the presence of potential interacting partners, some of which may hinder this ability. Furthermore, some molecular chaperone activities are redundant, allowing other proteins to function in place of mutated, dysfunctional chaperones. However, no single chaperone is able to fully compensate for PDI's roles in oxidative protein folding (Rutkevich, 2010).

Chemical chaperones could potentially be developed as a therapy for Cole Carpenter syndrome, resolving both ER stress and the downstream implications on the rest of the cell to varying degrees of effectiveness. A synthetic chemical chaperone as a nontoxic competitive inhibitor has been shown to correct the phenotype of the lysosomal storage disorder Fabry's disease (Yam, 2005). This disease arises from a mutant, yet catalytically active chaperone alpha-galactosidase A, which misfunctions and causes the aggregation of its substrate, which may mirror PDI and its role in Cole Carpenter syndrome. The responses of Y393C-PDI to the SMI treatments shown in Chapter 6 may suggest a similar treatment is possible for CCS, especially if further repetition shows a 'rescue' of PDI function. If so, this may provide an alternative to the currently used bisphosphonate therapy, and with sufficient future work, pertain to a viable cure of this disease.

Another potential approach could utilise gene therapy, which would deliver a functional form of PDI to the affected cells via a viral vector; this has been used successfully to treat other OI related disorders (Niyibizi, 2004). This would act as the essential 'compensatory chaperone', ensuring collagen is properly folded which would reduce and resolve ER stress. This would therefore prevent the imbalanced collagen production and resorption resulting in the brittle bone phenotype of CCS. Gene therapy approaches, using adeno-associated virus (AAV) vectors as above, have already proven to have outstanding beneficial effects in several ER chaperone

related diseases, such as neurodegenerative conditions, eye disorders, and metabolic diseases (Valenzuela, 2018).

When developing future therapies for CCS, further studies are essential to solve the complex relationships of PDI in health and disease. The redox activity of PDI facilitates internalization of some pathogens, alongside the influx of reactive oxygen species (ROS) in cells (Ramachandran, 2001). Furthermore, post-translationally modified version has been shown to promote protein aggregation commonly associated with neurodegenerative diseases (Cai, 1994). Taken alongside the evidence shown in this thesis, this highlights the complexity of PDI and its critical roles in physiology and pathology, a number of which may be affected in, or contribute to the phenotype of Cole Carpenter disease.
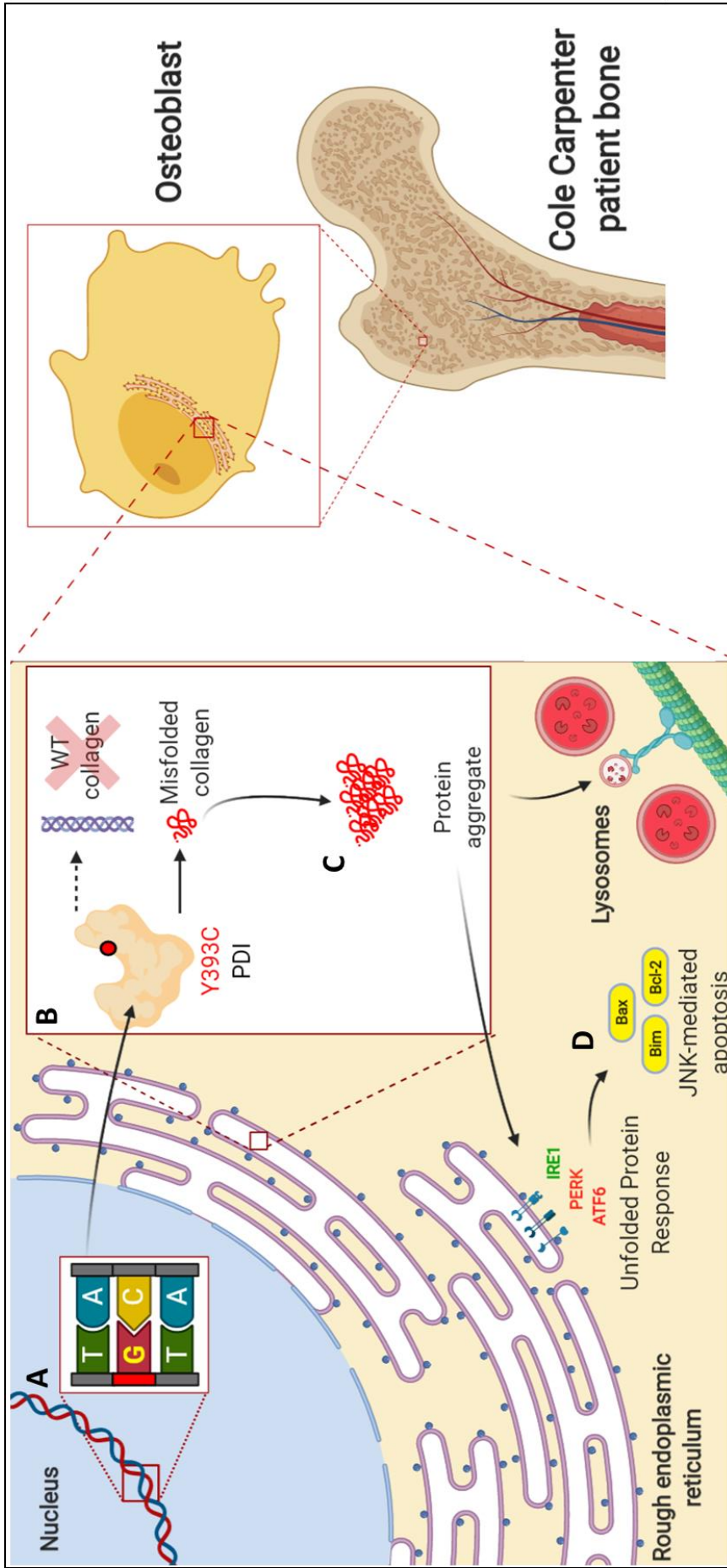
Figure 8.2. A proposed model of the molecular interactions which underpin Cole Carpenter syndrome. (A) A single nucleotide polymorphism (1178A>G) causes a Y393C mutation in ER resident chaperone PDI in Cole Carpenter patient. **(B)** The gain of a reactive cysteine causes Y393C-PDI to incorrectly fold the procollagen triple helix which is retained in the ER. Continued translation of procollagen chains causes aggregation within ER lumen. **(C)** Neither UPR or lysosomal-mediated autophagy can sufficiently clear the aggregates and fail to resolve the resultant ER stress. **(D)** The cell aims towards apoptosis.

8.12. Concluding remarks

Work undertaken in this project has allowed a preliminary model of the molecular mechanisms underpinning Cole Carpenter syndrome to be developed, as shown in Figure 8.2. This model proposes that Cole Carpenter syndrome is likely a result of disrupted activation of PDI through self-inhibition or abnormal disulphide interactions with other proteins in the ER. This would prevent oligomerisation into the wider C-P4H complex and result in the improper or incomplete folding of the collagen triple helix. Aggregation of this defective protein in the ER is likely to disrupt the delicate microenvironment of the ER and result in ER stress. Upregulating chaperones to resolve ER stress through the activated unfolded protein response (UPR) may result in more dysfunctional Y393C-PDI produced, which would not resolve the collagen misfolding problem. Furthermore, it is unlikely any other ER chaperones would be able to compensate for PDI's activity, due to its essential and varied functions within the activation/suppression of key players in the UPR, and its separate functions as an oxidoreductase. Other branches of the UPR may attempt to rescue the phenotype, alongside the lysosome-mediated autophagy protein degradation. The latter pathway may be able to compartmentalise some of the misfolded collagen, yet appears to be quickly overwhelmed, resulting in the continued progression of ER stress, and deformed, swollen lysosomes which are mostly stationary. This combination of factors may therefore result in an inability to clear misfolded collagen, and the subsequent failure to resolve ER stress. These osteoblasts then may direct themselves for apoptosis. Mass cell death would result in a disproportionately large amount of bone osteoid resorption by osteoclasts, compared to its production by osteoblasts. This imbalance may then result in the critically severe brittle bone phenotype of Cole Carpenter syndrome.

9. SUPPLEMENTARY MATERIALS

9.1. Statistical analysis

Table 9.1. Summary results of two-way ANOVA on effects of transfection condition and 16F16 inhibitor concentration on cell viability.

Source of Variation	% of total variation	P value
Interaction	7.74	< 0.0001
Transfection condition	66.14	< 0.0001
Inhibitor concentration	22.77	< 0.0001

Source of Variation	P value summary	Significant?
Interaction	***	Yes
Transfection condition	***	Yes
Inhibitor concentration	***	Yes

Source of Variation	Df	Sum-of-squares	Mean square	F
Interaction	8	0.1388	0.01734	8.689
Transfection condition	2	1.185	0.5927	296.9
Inhibitor concentration	4	0.4082	0.102	51.12
Residual	30	0.05988	0.001996	

Table 9.2. Summary results of two-way ANOVA on effects of transfection condition and PACMA 31 inhibitor concentration on cell viability.

Source of Variation	% of total variation	P value
Interaction	4.33	0.4611
Transfection condition	20.33	< 0.0001
Inhibitor Concentration	58.97	< 0.0001

Source of Variation	P value summary	Significant?
Interaction	ns	No
Transfection condition	***	Yes
Inhibitor concentration	***	Yes

Source of Variation	Df	Sum-of-squares	Mean square	F
Interaction	8	0.05558	0.006948	0.9932
Transfection condition	2	0.2608	0.1304	18.64
Inhibitor concentration	4	0.7562	0.189	27.02
Residual	30	0.2099	0.006995	

Table 9.3. Results of statistical analysis against NT and WT PDI transfected cells for each inhibitor (Two-way ANOVA, Bonferroni post-hoc tests).

	Inhibitor concentration (μM)	Difference	t	P value	Significance
16F16	0	-0.085	2.33	P > 0.05	ns
	4	-0.09533	2.613	P > 0.05	ns
	6	-0.055	1.508	P > 0.05	ns
	8	0.026	0.7127	P > 0.05	ns
	10	0.02333	0.6396	P > 0.05	ns
PACMA 31	0	0.07267	1.064	P > 0.05	ns
	4	0.06033	0.8835	P > 0.05	ns
	6	-0.022	0.3222	P > 0.05	ns
	8	0.006333	0.09274	P > 0.05	ns
	10	0.01933	0.2831	P > 0.05	ns

10 BIBLIOGRAPHY

Acosta-Alvear, D., Zhou, Y., Blasi, A., Tsikitis, M., Lents, N. H., Arias, C., ... & Dynlacht, B. D. (2007). XBP1 controls diverse cell type-and condition-specific transcriptional regulatory networks. *Molecular cell*, *27*(1), 53-66.

Alanen, H. I., Salo, K. E. H., Pekkala, M., Siekkinen, H. M., Pirneskoski, A., & Ruddock, L. W. (2003). Defining the domain boundaries of the human protein disulphide isomerases. *Antioxidants and Redox Signalling*, *5*(4), 367-374.

Alberts, B., Bray, D., Hopkin, K., Johnson, A. D., Lewis, J., Raff, M., ... & Walter, P. (2015). *Essential cell biology*. Garland Science.

Amor, D. J., Savarirayan, R., Schneider, A. S., & Bankier, A. (2000). New case of Cole-Carpenter syndrome. *American journal of medical genetics*, *92*(4), 273-277.

Appenzeller-Herzog, C., Riemer, J., Zito, E., Chin, K. T., Ron, D., Spiess, M., & Ellgaard, L. (2010). Disulphide production by Ero1α–PDI relay is rapid and effectively regulated. *The EMBO journal*, *29*(19), 3318-3329.

Araki, K., Iemura, S. I., Kamiya, Y., Ron, D., Kato, K., Natsume, T., & Nagata, K. (2013). Ero1-α and PDI's constitute a hierarchical electron transfer network of endoplasmic reticulum oxidoreductases. *Journal of Cell Biology*, *202*(6), 861-874.

Atkin, J. D., Farg, M. A., Walker, A. K., mclean, C., Tomas, D., & Horne, M. K. (2008). Endoplasmic reticulum stress and induction of the unfolded protein response in human sporadic amyotrophic lateral sclerosis. *Neurobiology of syndrome*, *30*(3), 400-407.

Balasubramanian, M., Padidela, R., Pollitt, R. C., Bishop, N. J., Mughal, M. Z., Offiah, A. C., ... & Stephens, D. J. (2018). P4HB recurrent missense mutation causing Cole Carpenter syndrome. *Journal of medical genetics*, *55*(3), 158-165.

Bálint, Š., Vilanova, I. V., Álvarez, Á. S., & Lakadamyali, M. (2013). Correlative live-cell and superresolution microscopy reveals cargo transport dynamics at microtubule intersections. *Proceedings of the National Academy of Sciences*, *110*(9), 3375-3380.

Bancelin, S., Aimé, C., Gusachenko, I., Kowalczuk, L., Latour, G., Coradin, T., & Schanne-Klein, M. C. (2014). Determination of collagen fibril size via absolute measurements of second-harmonic generation signals. *Nature communications*, *5*(1), 1-8.

Baumann, S., & Hennet, T. (2016). Collagen accumulation in osteosarcoma cells lacking GLT25D1 collagen galactosyltransferase. *Journal of Biological Chemistry*, *291*(35), 18514-18524.

Bekendam, R. H., Bendapudi, P. K., Lin, L., Nag, P. P., Pu, J., Kennedy, D. R., ... & Flaumenhaft, R. (2016). A substrate-driven allosteric switch that enhances PDI catalytic activity. *Nature communications*, *7*(1), 1-11.

Benham, A. M. (2012). The protein disulphide isomerase family: key players in health and syndrome. Antioxidants & redox signaling, 16(8), 781-789.

Benham, A. M., Cabibbo, A., Fassio, A., Bulleid, N., Sitia, R., & Braakman, I. (2000). The CXXCXXC motif determines the folding, structure and stability of human Ero1-Lα. *The EMBO journal*, *19*(17), 4493-4502.

Bennett, M. R., Evan, G. I., & Schwartz, S. M. (1995). Apoptosis of rat vascular smooth muscle cells is regulated by p53-dependent and-independent pathways. *Circulation Research*, *77*(2), 266-273.

Berillis, P. (2013). The role of collagen in the aorta's structure. *The Open Circulation and Vascular Journal*, *6*(1).

Blackstone, C., & Prinz, W. A. (2016). Endoplasmic Reticulum: Keeping in shape. *Elife*, *5*, e20468.

Blair, H. C., Larrouture, Q. C., Li, Y., Lin, H., Beer-Stoltz, D., Liu, L., Tuan, R. S., Robinson, L. J., Schlesinger, P. H., & Nelson, D. J. (2017). Osteoblast Differentiation and Bone Matrix Formation In Vivo and In Vitro. *Tissue engineering. Part B, Reviews*, *23*(3), 268–280.

Bonaventure, J., Rousseau, F., Legeai-Mallet, L., Merrer, M. L., Munnich, A., & Maroteaux, P. (1996). Common mutations in the gene encoding fibroblast growth factor receptor 3 account for achondroplasia, hypochondroplasia and thanatophoric dysplasia. *Acta Pædiatrica*, *85*, 33-38.

Bottomley, M. J., Batten, M. R., Lumb, R. A., & Bulleid, N. J. (2001). Quality control in the endoplasmic reticulum: PDI mediates the ER retention of unassembled procollagen C-propeptides. *Current Biology*, *11*(14), 1114-1118.

Brandizzi, F., Hanton, S., DaSilva, L. L. P., Boevink, P., Evans, D., Oparka, K., ... & Hawes, C. (2003). ER quality control can lead to retrograde transport from the ER lumen to the cytosol and the nucleoplasm in plants. *The Plant Journal*, *34*(3), 269-281.

Burns, J. A., Butler, J. C., Moran, J., & Whitesides, G. M. (1991). Selective reduction of disulphides by tris (2-carboxyethyl) phosphine. *The Journal of Organic Chemistry*, *56*(8), 2648-2650.

Cacciottolo, M., Nogalska, A., D'Agostino, C., Engel, W. K., & Askanas, V. (2013). Chaperone-mediated autophagy components are upregulated in sporadic inclusion-body myositis muscle fibres. *Neuropathology and applied neurobiology*, *39*(7), 750-761.

Cai, H., Wang, C. C., and Tsou, C. L. (1994). Chaperone-like activity of protein disulphide isomerase in the refolding of a protein with no disulphide bonds. *J. Biol. Chem.* 269, 24550–24552.

Cai, J., Tang, H., Xu, L., Wang, X., Yang, C., Ruan, S., ... & Wang, Z. (2012). Fibroblasts in omentum activated by tumor cells promote ovarian cancer growth, adhesion and invasiveness. *Carcinogenesis*, *33*(1), 20-29.

Canty, E. G., & Kadler, K. E. (2005). Procollagen trafficking, processing and fibrillogenesis. *Journal of cell science*, *118*(7), 1341-1353.

Cassella, J. P., Barber, P., Catterall, A. C., & Ali, S. Y. (1994). A morphometric analysis of osteoid collagen fibril diameter in osteogenesis imperfecta. Bone, 15(3), 329-334.

Chan, D., Lamande, S. R., Cole, W. G., & Bateman, J. F. (1990). Regulation of procollagen synthesis and processing during ascorbate-induced extracellular matrix accumulation in vitro. *Biochemical journal*, *269*(1), 175-181.

Chen, S., & Zhang, D. (2015). Friend or foe: Endoplasmic reticulum protein 29 (ERp29) in epithelial cancer. *FEBS open bio*, *5*, 91-98.

Chiu, H. W., Tseng, Y. C., Hsu, Y. H., Lin, Y. F., Foo, N. P., Guo, H. R., & Wang, Y. J. (2015). Arsenic trioxide induces programmed cell death through stimulation of ER stress and inhibition of the ubiquitin–proteasome system in human sarcoma cells. *Cancer letters*, *356*(2), 762-772.

Ciarallo, A., Barralet, J., Tanzer, M., & Kremer, R. (2006). An approach to compare the quality of cancellous bone from the femoral necks of healthy and osteoporotic patients through compression testing and microcomputed tomography imaging. *Mcgill Journal of Medicine: MJM*, *9*(2), 102.

Cole, E. D., & Carpenter, T. O. (1987). Bone fragility, craniosynostosis, ocular proptosis, hydrocephalus, and distinctive facial features: a newly recognized type of osteogenesis imperfecta. *The Journal of pediatrics*, *110*(1), 76-80.

Collot, M., Louvard, D., & Singer, S. J. (1984). Lysosomes are associated with microtubules and not with intermediate filaments in cultured fibroblasts. *Proceedings of the National Academy of Sciences*, *81*(3), 788-792.

Cox, J. S., Shamu, C. E., & Walter, P. (1993). Transcriptional induction of genes encoding endoplasmic reticulum resident proteins requires a transmembrane protein kinase. *Cell*, *73*(6), 1197-1206.

Crescitelli, R., Lässer, C., Szabó, T. G., Kittel, A., Eldh, M., Dianzani, I., ... & Lötvall, J. (2013). Distinct RNA profiles in subpopulations of extracellular vesicles: apoptotic bodies, microvesicles and exosomes. *Journal of extracellular vesicles*, *2*(1), 20677.

Darby, N. J., & Creighton, T. E. (1995). Functional properties of the individual thioredoxin-like domains of protein disulfide isomerase. *Biochemistry*, *34*(37), 11725-11735.

Darby, N. J., Penka, E., & Vincentelli, R. (1998). The multi-domain structure of protein disulphide isomerase is essential for high catalytic efficiency. *Journal of molecular biology*, *276*(1), 239-247.

Davis, R., Schooley, K., Rasmussen, B., Thomas, J., & Reddy, P. (2000). Effect of PDI overexpression on recombinant protein secretion in CHO cells. *Biotechnology progress, 16*(5), 736-743.

de Araujo, M. E., Liebscher, G., Hess, M. W., & Huber, L. A. (2020). Lysosomal size matters. *Traffic, 21*(1), 60-75.

De Leonibus, C., Cinque, L., & Settembre, C. (2019). Emerging lysosomal pathways for quality control at the endoplasmic reticulum. *FEBS letters, 593*(17), 2319-2329.

Demidenko, Z. N., Kalurupalle, S., Hanko, C., Lim, C. U., Broude, E., & Blagosklonny, M. V. (2008). Mechanism of G1-like arrest by low concentrations of paclitaxel: next cell cycle p53-dependent arrest with sub G1 DNA content mediated by prolonged mitosis. *Oncogene*, *27*(32), 4402-4410.

Dhanasekaran, D. N., & Reddy, E. P. (2017). JNK-signaling: a multiplexing hub in programmed cell death. *Genes & cancer*, *8*(9-10), 682.

Dice, J. F. (2007). Chaperone-mediated autophagy. *Autophagy*, *3*(4), 295-299.

Eppley, B. L., Kalsbeck, J. E., & Sadove, A. M. (1994). Cranial reconstruction in osteogenesis imperfecta. *The Journal of craniofacial surgery, 5*(3), 180-184.

Fassio, A., & Sitia, R. (2002). Formation, isomerisation and reduction of disulphide bonds during protein quality control in the endoplasmic reticulum. *Histochemistry and cell biology*, *117*(2), 151-157.

Fernandes, H. J., Hartfield, E. M., Christian, H. C., Emmanoulidou, E., Zheng, Y., Booth, H., ... & Wade-Martins, R. (2016). ER stress and autophagic perturbations lead to elevated extracellular α-synuclein in GBA-N370S Parkinson's iPSC-derived dopamine neurons. *Stem cell reports*, *6*(3), 342-356.

Fhlathartaigh, M. N., McMahon, J., Reynolds, R., Connolly, D., Higgins, E., Counihan, T., & FitzGerald, U. (2013). Calreticulin and other components of endoplasmic reticulum stress in rat and human inflammatory demyelination. *Acta neuropathologica communications*, *1*(1), 1-15.

Fiszer-Kierzkowska, A., Vydra, N., Wysocka-Wycisk, A., Kronekova, Z., Jarząb, M., Lisowska, K. M., & Krawczyk, Z. (2011). Liposome-based DNA carriers may induce cellular stress response and change gene expression pattern in transfected cells. *BMC molecular biology*, *12*(1), 1-9.

Fleisch, H., Reszka, A., Rodan, G., & Rogers, M. (2002). Bisphosphonates: mechanisms of action. *In Principles of bone biology* (pp. 1361-XLIII). Academic Press.

Forer, A., Kalnins, V. I., & Zimmerman, A. M. (1976). Spindle birefringence of isolated mitotic apparatus: further evidence for two birefringent spindle components. *Journal of cell science*, *22*(1), 115-131.

Forlino, A., & Marini, J. C. (2016). Osteogenesis imperfecta. *The Lancet*, *387*(10028), 1657-1671.

Fourriere, L., Jimenez, A. J., Perez, F., & Boncompain, G. (2020). The role of microtubules in secretory protein transport. *Journal of cell science*, *133*(2).

Frand, A. R., Cuozzo, J. W., & Kaiser, C. A. (2000). Pathways for protein disulphide bond formation. *Trends in cell biology*, *10*(5), 203-210.

Freedman, R. B., Ganea, P. J., Hawkins, H. C., Hlodan, R., mclaughlin, S. H., & Parry, J. W. (1998). Experimental and theoretical analyses of the domain architecture of mammalian protein disulphide-isomerase. *Biological chemistry, 379*(3), 321-328.

Freedman, R. B., Hirst, T. R., & Tuite, M. F. (1994). Protein disulphide isomerase: building bridges in protein folding. *Trends in biochemical sciences*, *19*(8), 331-336.

Fregno, I., & Molinari, M. (2019). Proteasomal and lysosomal clearance of faulty secretory proteins: ER-associated degradation (ERAD) and ER-to-lysosome-associated degradation (ERLAD) pathways. *Critical reviews in biochemistry and molecular biology*, *54*(2), 153-163.

Freitas, R. A. (1999). *Nanomedicine, volume I: basic capabilities*. 210-219. Georgetown, TX: Landes Bioscience.

Frydman, J. (2001). Folding of newly translated proteins in vivo: the role of molecular chaperones. *Annual review of biochemistry*, *70*(1), 603-647.

Fryns, J. P. (1996). Osteopenia, abnormal dentition, hydrops fetalis and communicating hydrocephalus: unusual early clinical signs in Coffin-Lowry syndrome. *Clinical genetics*, *50*(2), 112-112.

Fujimoto, T., Nakamura, O., Saito, M., Tsuru, A., Matsumoto, M., Kohno, K., ... & Kadokura, H. (2018). Identification of the physiological substrates of PDIp, a pancreas-specific protein-disulphide isomerase family member. *Journal of Biological Chemistry*, *293*(48), 18421-18433.

Fujiwara, T., Ye, S., Castro-Gomes, T., Winchell, C. G., Andrews, N. W., Voth, D. E., ... & Zhao, H. (2016). PLEKHM1/DEF8/RAB7 complex regulates lysosome positioning and bone homeostasis. *JCI insight*, *1*(17).

Galligan, J. J., & Petersen, D. R. (2012). The human protein disulphide isomerase gene family. *Human genomics*, *6*(1), 6.

Gjaltema, R. A., & Bank, R. A. (2017). Molecular insights into prolyl and lysyl hydroxylation of fibrillar collagens in health and disease. *Critical reviews in biochemistry and molecular biology*, *52*(1), 74-95.

Goldberger, R. F., Epstein, C. J., & Anfinsen, C. B. (1963). Acceleration of reactivation of reduced bovine pancreatic ribonuclease by a microsomal system from rat liver. *Journal of Biological Chemistry*, *238*(2), 628-635.

Goodpaster, T., Legesse-Miller, A., Hameed, M. R., Aisner, S. C., Randolph-Habecker, J., & Coller, H. A. (2008). An immunohistochemical method for identifying fibroblasts in formalin-fixed, paraffin-embedded tissue. *Journal of Histochemistry & Cytochemistry*, *56*(4), 347-358.

Hall, John (2011). *Textbook of Medical Physiology (12th ed.).* Philadelphia: Elsevier. 957–960

Heinegård, D., & Oldberg, Å. (1989). Structure and biology of cartilage and bone matrix noncollagenous macromolecules. *The FASEB Journal*, *3*(9), 2042-2051.

Helson, L., & Helson, C. (1985). Effects of vitamin E on fibroblast fibronectin. *Taylor and Francis.* 221-227

Hettinghouse, A., Liu, R., & Liu, C. J. (2018). Multifunctional molecule ERp57: From cancer to neurodegenerative diseases. *Pharmacology & therapeutics*, *181*, 34-48.

Hetz, C., & Papa, F. R. (2018). The unfolded protein response and cell fate control. *Molecular cell*, *69*(2), 169-181.

Hiller, S. (2021). Molecular chaperones and their denaturing effect on client proteins. *Journal of Biomolecular NMR*, *75*(1), 1-8.

Hoffstrom, B. G., Kaplan, A., Letso, R., Schmid, R. S., Turmel, G. J., Lo, D. C., & Stockwell, B. R. (2010). Inhibitors of protein disulphide isomerase suppress apoptosis induced by misfolded proteins. *Nature chemical biology*, *6*(12), 900-906.

Honjo, Y., Horibe, T., Torisawa, A., Ito, H., Nakanishi, A., Mori, H., ... & Kawakami, K. (2014). Protein disulphide isomerase P5-immunopositive inclusions in patients with Alzheimer's disease. *Journal of Alzheimer's Disease, 38*(3), 601-609.

Hosokawa, N., & Nagata, K. (2000). Procollagen binds to both prolyl 4-hydroxylase/protein disulphide isomerase and HSP47 within the endoplasmic reticulum in the absence of ascorbate. *FEBS letters*, *466*(1), 19-25.

Ishida, Y., & Nagata, K. (2011). HSP47 as a collagen-specific molecular chaperone. *Methods in enzymology*, *499*, 167-182.

Ishiyama, M., Miyazono, Y., Sasamoto, K., Ohkura, Y., & Ueno, K. (1997). A highly water-soluble disulfonated tetrazolium salt as a chromogenic indicator for NADH as well as cell viability. *Talanta*, *44*(7), 1299-1305.

Iwayama, T., Okada, T., Ueda, T., Tomita, K., Matsumoto, S., Takedachi, M., ... & Murakami, S. (2019). Osteoblastic lysosome plays a central role in mineralization. *Science advances*, *5*(7), eaax0672.

Izawa, T., Nagai, H., Endo, T., & Nishikawa, S. I. (2012). Yos9p and Hrd1p mediate ER retention of misfolded proteins for ER-associated degradation. *Molecular biology of the cell*, *23*(7), 1283-1293.

142

Jaenicke, R. (1993). What does protein refolding in vitro tell us about protein folding in the cell?. *Philosophical Transactions of the Royal Society of London. Series B: Biological Sciences*, *339*(1289), 287-295.

Jessop, C. E., Chakravarthi, S., Garbi, N., Hämmerling, G. J., Lovell, S., & Bulleid, N. J. (2007). ERp57 is essential for efficient folding of glycoproteins sharing common structural domains. *The EMBO journal*, *26*(1), 28-40.

Johnson, J. L., Napolitano, G., Monfregola, J., Rocca, C. J., Cherqui, S., & Catz, S. D. (2013). Upregulation of the Rab27a-dependent trafficking and secretory mechanisms improves lysosomal transport, alleviates endoplasmic reticulum stress, and reduces lysosome overload in cystinosis. *Molecular and cellular biology*, *33*(15), 2950-2962.

Kabuta, T., Furuta, A., Aoki, S., Furuta, K., & Wada, K. (2008). Aberrant interaction between Parkinson disease-associated mutant UCH-L1 and the lysosomal receptor for chaperone-mediated autophagy. *Journal of Biological Chemistry*, *283*(35), 23731-23738.

Kamp, H. G., Eisenbrand, G., Schlatter, J., Würth, K., & Janzowski, C. (2005). Ochratoxin A: induction of (oxidative) DNA damage, cytotoxicity and apoptosis in mammalian cell lines and primary cells. *Toxicology*, *206*(3), 413-425.

Kaneya, Y., Takata, H., Wada, R., Kure, S., Ishino, K., Kudo, M., ... & Naito, Z. (2021). Inhibitor for protein disulfide-isomerase family A member 3 enhances the antiproliferative effect of inhibitor for mechanistic target of rapamycin in liver cancer: An in vitro study on combination treatment with everolimus and 16F16. *Oncology Letters*, *21*(1), 1-1.

Karsdal, M. (2019). *Biochemistry of collagens, laminins and elastin: structure, function and biomarkers*. Academic Press.

Keene, D. R., Sakai, L. Y., & Burgeson, R. E. (1991). Human bone contains type III collagen, type VI collagen, and fibrillin: type III collagen is present on specific fibers that may mediate attachment of tendons, ligaments, and periosteum to calcified bone cortex. *Journal of Histochemistry & Cytochemistry*, *39*(1), 59-69.

Kelley, L. A., Mezulis, S., Yates, C. M., Wass, M. N., & Sternberg, M. J. (2015). The Phyre2 web portal for protein modeling, prediction and analysis. *Nature protocols*, *10*(6), 845.

Khera, N., & Rajput, S. (2017). Therapeutic potential of small molecule inhibitors. *Journal of cellular biochemistry*, *118*(5), 959-961.

Khosla, S., Bilezikian, J. P., Dempster, D. W., Lewiecki, E. M., Miller, P. D., Neer, R. M., ... & Potts, J. T. (2012). Benefits and risks of bisphosphonate therapy for osteoporosis. *The Journal of Clinical Endocrinology & Metabolism*, *97*(7), 2272-2282.

Kivirikko, K. I., & Myllyharju, J. (1998). Prolyl 4-hydroxylases and their protein disulphide isomerase subunit. *Matrix Biology*, *16*(7), 357-368.

Klappa, P., Ruddock, L. W., Darby, N. J., & Freedman, R. B. (1998). The b′ domain provides the principal peptide-binding site of protein disulphide isomerase but all domains contribute to binding of misfolded proteins. *The EMBO journal*, *17*(4), 927-

Klionsky, D. J., & Eskelinen, E. L. (2014). The vacuole vs. the lysosome: When size matters. *Autophagy*, *10*(2), 185-187.

Knoblach, B., Keller, B. O., Groenendyk, J., Aldred, S., Zheng, J., Lemire, B. D., ... & Michalak, M. (2003). ERp19 and ERp46, new members of the thioredoxin family of endoplasmic reticulum proteins. *Molecular & Cellular Proteomics*, *2*(10), 1104-1119.

Ko, H. S., Uehara, T., & Nomura, Y. (2002). Role of ubiquilin associated with protein-disulphide isomerase in the endoplasmic reticulum in stress-induced apoptotic cell death. *Journal of Biological Chemistry*, *277*(38), 35386-35392.

Ko, M. K., & Kay, E. P. (2001). Subcellular localization of procollagen I and prolyl 4-hydroxylase in corneal endothelial cells. *Experimental cell research*, *264*(2), 363-371.

Koivunen, P., HELAAKOSKI, T., ANNUNEN, P., VEIJOLA, J., RÄISÄNEN, S., PIHLAJANIEMI, T., & KIVIRIKKO, K. I. (1996). ERp60 does not substitute for protein disulphide isomerase as the β-subunit of prolyl 4-hydroxylase. *Biochemical Journal*, *316*(2), 599-605.

Koivunen, P., Salo, K. E., Myllyharju, J., & Ruddock, L. W. (2005). Three binding sites in protein-disulphide isomerase cooperate in collagen prolyl 4-hydroxylase tetramer assembly. *Journal of Biological Chemistry*, *280*(7), 5227-5235.

Koopman, G., Reutelingsperger, C. P., Kuijten, G. A., Keehnen, R. M., Pals, S. T., & Van Oers, M. H. (1994). Annexin V for flow cytometric detection of phosphatidylserine expression on B cells undergoing apoptosis.

Korfei, M., Ruppert, C., Mahavadi, P., Henneke, I., Markart, P., Koch, M., ... & Guenther, A. (2008). Epithelial endoplasmic reticulum stress and apoptosis in sporadic idiopathic

pulmonary fibrosis. *American journal of respiratory and critical care medicine*, *178*(8), 838-846.

Kouroku, Y., Fujita, E., Tanida, I., Ueno, T., Isoai, A., Kumagai, H., ... & Momoi, T. (2007). ER stress (PERK/eIF2 α phosphorylation) mediates the polyglutamine-induced LC3 conversion, an essential step for autophagy formation. *Cell Death & Differentiation*, *14*(2), 230-239.

Kozlov, G., Määttänen, P., Thomas, D. Y., & Gehring, K. (2010). A structural overview of the PDI family of proteins. *The FEBS journal*, *277*(19), 3924-3936.

Kranz, P., Neumann, F., Wolf, A., Classen, F., Pompsch, M., Ocklenburg, T., ... & Riffkin, H. (2017). PDI is an essential redox-sensitive activator of PERK during the unfolded protein response (UPR). *Cell death & disease*, *8*(8), e2986-e2986.

Krysko, D. V., Berghe, T. V., Parthoens, E., D'Herde, K., & Vandenabeele, P. (2008). Methods for distinguishing apoptotic from necrotic cells and measuring their clearance. *Methods in enzymology*, *442*, 307-341.

Le Guilloux, V., Schmidtke, P., & Tuffery, P. (2009). Fpocket: an open source platform for ligand pocket detection. *BMC bioinformatics*, *10*(1), 1-11.

Lee, H., Park, M. T., Choi, B. H., Oh, E. T., Song, M. J., Lee, J., ... & Park, H. J. (2011). Endoplasmic reticulum stress-induced JNK activation is a critical event leading to mitochondria-mediated cell death caused by β-lapachone treatment. *PloS one*, *6*(6), e21533.

Lee, J. E., Cathey, P. I., Wu, H., Parker, R., & Voeltz, G. K. (2020). Endoplasmic reticulum contact sites regulate the dynamics of membraneless organelles. *Science, 367*(6477).

Lee, J. G., Takahama, S., Zhang, G., Tomarev, S. I., & Ye, Y. (2016). Unconventional secretion of misfolded proteins promotes adaptation to proteasome dysfunction in mammalian cells. *Nature cell biology*, *18*(7), 765-776.

Lee, W., Kim, K. R., Singaravelu, G., Park, B. J., Kim, D. H., Ahnn, J., & Yoo, Y. J. (2006). Alternative chaperone machinery may compensate for calreticulin/calnexin deficiency in Caenorhabditis elegans. *Proteomics*, *6*(4), 1329-1339.

Leijnse, N., Jeon, J. H., Loft, S., Metzler, R., & Oddershede, L. B. (2012). Diffusion inside living human cells. *The European Physical Journal Special Topics*, *204*(1), 75-84.

Limonta, P., Moretti, R. M., Marzagalli, M., Fontana, F., Raimondi, M., & Montagnani Marelli, M. (2019). Role of Endoplasmic Reticulum Stress in the Anticancer Activity of Natural Compounds. *International journal of molecular sciences*, *20*(4), 961. Doi:10.3390/ijms20040961

Lindquist, S. L., & Kelly, J. W. (2011). Chemical and biological approaches for adapting proteostasis to ameliorate protein misfolding and aggregation syndromes–progress and prognosis. *Cold Spring Harbor perspectives in biology*, *3*(12), a004507.

Liu, H., Chen, J., Li, W., Rose, M. E., Shinde, S. N., Balasubramani, M., ... & Hickey, R. W. (2015). Protein disulphide isomerase as a novel target for cyclopentenone prostaglandins: implications for hypoxic ischemic injury. *The FEBS journal*, *282*(10), 2045-2059.

Liu, Y., & Chang, A. (2008). Heat shock response relieves ER stress. *The EMBO journal*, *27*(7), 1049-1059.

Lobito, A. A., Kimberley, F. C., Muppidi, J. R., Komarow, H., Jackson, A. J., Hull, K. M., ... & Siegel, R. M. (2006). Abnormal disulphide-linked oligomerization results in ER retention and altered signaling by TNFR1 mutants in TNFR1-associated periodic fever syndrome (TRAPS). *Blood*, *108*(4), 1320-1327.

Long, M. W., Robinson, J. A., Ashcraft, E. A., & Mann, K. G. (1995). Regulation of human bone marrow-derived osteoprogenitor cells by osteogenic growth factors. *The Journal of clinical investigation*, *95*(2), 881-887.

Lüllmann-Rauch, R. (2005). History and morphology of the lysosome. In *Lysosomes* (pp. 1-16). Springer, Boston, MA.

Lumb, R. A., & Bulleid, N. J. (2002). Is protein disulphide isomerase a redox-dependent molecular chaperone?. *The EMBO Journal*, *21*(24), 6763-6770.

Macario, A. J., & de Macario, E. C. (2007). Chaperonopathies and chaperonotherapy. *FEBS letters*, *581*(19), 3681-3688.

Macario, A. J., Grippo, T. M., & de Macario, E. C. (2005). Genetic disorders involving molecular-chaperone genes: a perspective. *Genetics in Medicine*, *7*(1), 3-12.

Macdermot, K. D., Buckley, B., & Van Someren, V. (1995). Osteopenia, abnormal dentition, hydrops fetalis and communicating hydrocephalus. *Clinical genetics*, *48*(4), 217-220.

Mahanty, S., Dakappa, S. S., Shariff, R., Patel, S., Swamy, M. M., Majumdar, A., & Setty, S. R. G. (2019). Keratinocyte differentiation promotes ER stress-dependent lysosome biogenesis. *Cell death & disease*, *10*(4), 1-17.

Makareeva, E., & Leikin, S. (2014). Collagen structure, folding and function. In *Osteogenesis Imperfecta* (pp. 71-84). Academic Press.

Makareeva, E., Mertz, E. L., Kuznetsova, N. V., Sutter, M. B., DeRidder, A. M., Cabral, W. A., ... & Leikin, S. (2008). Structural heterogeneity of type I collagen triple helix and its role in osteogenesis imperfecta. *Journal of Biological Chemistry*, *283*(8), 4787-4798.

Malhotra, V., & Erlmann, P. (2015). The pathway of collagen secretion. *Annual review of cell and developmental biology*, *31*, 109-124.

Mancilla, E. E., De Luca, F., Uyeda, J. A., Czerwiec, F. S., & Baron, J. (1998). Effects of fibroblast growth factor-2 on longitudinal bone growth. *Endocrinology*, *139*(6), 2900-2904.

Marangon, M., Van Sluyter, S. C., Waters, E. J., & Menz, R. I. (2014). Structure of haze forming proteins in white wines: Vitis vinifera thaumatin-like proteins. *PloS one*, *9*(12), e113757.

Marchi, F., & Leblond, C. P. (1984). Radioautographic characterization of successive compartments along the rough endoplasmic reticulum-Golgi pathway of collagen precursors in foot pad fibroblasts of [3H] proline-injected rats. *The Journal of cell biology*, *98*(5), 1705-1709.

Marotti, G. (1979). Osteocyte orientation in human lamellar bone and its relevance to the morphometry of periosteocytic lacunae. *Metabolic Bone Disease and Related Research*, *1*(4), 325-333.

Martinez, J. E., Vershinin, M. D., Shubeita, G. T., & Gross, S. P. (2007). On the use of in vivo cargo velocity as a biophysical marker. *Biochemical and biophysical research communications*, *353*(3), 835-840.

Marwaha, R. K., Sarkar, B., Katariya, S., & Jayshree, K. (1993). Cole Carpenter syndrome. *Indian journal of pediatrics*, *60*(2), 305-308.

Mateus, D., Marini, E. S., Progida, C., & Bakke, O. (2018). Rab7a modulates ER stress and ER morphology. *Biochimica et Biophysica Acta (BBA)-Molecular Cell Research*, *1865*(5), 781-793.

Mattaj, I. W. (2004). Sorting out the nuclear envelope from the endoplasmic reticulum. *Nature reviews molecular cell biology*, *5*(1), 65-69.

Matteoni, R., & Kreis, T. E. (1987). Translocation and clustering of endosomes and lysosomes depends on microtubules. *The Journal of cell biology*, *105*(3), 1253-1265.

Mayer, M. P., & Bukau, B. (2005). HSP70 chaperones: cellular functions and molecular mechanism. *Cellular and molecular life sciences*, *62*(6), 670-684.

Mazzarella, R. A., Srinivasan, M. Y. T. H. I. L. I., Haugejorden, S. M., & Green, M. (1990). ERp72, an abundant luminal endoplasmic reticulum protein, contains three copies of the active site sequences of protein disulphide isomerase. *Journal of Biological Chemistry*, *265*(2), 1094-1101.

Mcpherson, E., & Clemens, M. (1997). Bruck syndrome (osteogenesis imperfecta with congenital joint contractures): review and report on the first North American case. *American journal of medical genetics*, *70*(1), 28-31.

Mezghrani, A., Fassio, A., Benham, A., Simmen, T., Braakman, I., & Sitia, R. (2001). Manipulation of oxidative protein folding and PDI redox state in mammalian cells. *The EMBO journal*, *20*(22), 6288-6296.

Miller, A. (1984). Collagen: the organic matrix of bone. *Philosophical Transactions of the Royal Society of London. B, Biological Sciences*, *304*(1121), 455-477.

Miura, D., Dobrovolsky, V. N., Kasahara, Y., Katsuura, Y., & Heflich, R. H. (2008). Development of an in vivo gene mutation assay using the endogenous Pig-A gene: I. Flow cytometric detection of CD59-negative peripheral red blood cells and CD48-negative spleen T-cells from the rat. *Environmental and molecular mutagenesis*, *49*(8), 614-621.

Mizushima, N. (2007). Autophagy: process and function. *Genes & development*, *21*(22), 2861-2873.

Moore, P., Bernardi, K. M., & Tsai, B. (2010). The Ero1 α-PDI redox cycle regulates retro-translocation of cholera toxin. *Molecular biology of the cell*, 21(7), 1305-1313.

Mossuto, M. F. (2013). Disulphide bonding in neurodegenerative misfolding diseases. *International journal of cell biology*, *2013*.

Murshed, M. (2018). Mechanism of bone mineralization. *Cold Spring Harbor perspectives in medicine*, *8*(12), a031229.

Myllyharju, J. (2003). Prolyl 4-hydroxylases, the key enzymes of collagen biosynthesis. *Matrix Biology, 22*(1), 15-24.

Nabavi, N., Urukova, Y., Cardelli, M., Aubin, J. E., & Harrison, R. E. (2008). Lysosome dispersion in osteoblasts accommodates enhanced collagen production during differentiation. *Journal of Biological Chemistry, 283*(28), 19678-19690.

Nakashima, A., Cheng, S. B., Kusabiraki, T., Motomura, K., Aoki, A., Ushijima, A., ... & Saito, S. (2019). Endoplasmic reticulum stress disrupts lysosomal homeostasis and induces blockade of autophagic flux in human trophoblasts. *Scientific reports, 9*(1)

Nelson, D. L. and Cox, M. M. (2005) Lehninger's Principles of Biochemistry, 4th Edition, W. H. Freeman and Company, New York.

Nguyen, V. D., Saaranen, M. J., Karala, A. R., Lappi, A. K., Wang, L., Raykhel, I. B., ... & Ruddock, L. W. (2011). Two endoplasmic reticulum PDI peroxidases increase the efficiency of the use of peroxide during disulphide bond formation. *Journal of molecular biology, 406*(3), 503-515.

Niyibizi, C., Wang, S., Mi, Z., & Robbins, P. D. (2004). Gene therapy approaches for osteogenesis imperfecta. *Gene therapy, 11*(4), 408-416.

Oka OB, Yeoh HY, Bulleid NJ (2015) Thiol-disulphide exchange between the PDI family of oxidoreductases negates the requirement for an oxidase or reductase for each enzyme. *Biochem J* 469: 279–288

Ouyang, L., & Yang, F. (2017). Cole–Carpenter syndrome-1 with a de novo heterozygous deletion in the P4HB gene in a Chinese girl: A case report. *Medicine, 96*(52).

Ozdemir, B., Kurtis, B., Tuter, G., Senguven, B., & Yildirim, B. (2016). Osteocalcin and osteonectin expression after double application of platelet-rich plasma in rabbits. *Journal of Istanbul University Faculty of Dentistry, 50*(2), 1.

Pan, C., Kumar, C., Bohl, S., Klingmueller, U., & Mann, M. (2009). Comparative proteomic phenotyping of cell lines and primary cells to assess preservation of cell type-specific functions. *Molecular & Cellular Proteomics, 8*(3), 443-450.

Parkinson, I. H., & Fazzalari, N. L. (2013). Characterisation of trabecular bone structure. *In Skeletal Aging and Osteoporosis* (pp. 31-51). Springer, Berlin, Heidelberg.

Pihlajaniemi, T., Myllylä, R., & Kivirikko, K. I. (1991). Prolyl 4-hydroxylase and its role in collagen synthesis. *Journal of hepatology, 13*, S2-S7.

149

Primm, T. P., & Gilbert, H. F. (2001). Hormone binding by protein disulphide isomerase, a high capacity hormone reservoir of the endoplasmic reticulum. *Journal of Biological Chemistry*, *276*(1), 281-286.

Pu, J., Schindler, C., Jia, R., Jarnik, M., Backlund, P., & Bonifacino, J. S. (2015). BORC, a multisubunit complex that regulates lysosome positioning. *Developmental cell*, *33*(2), 176-188.

Ramachandran, N., Root, P., Jiang, X. M., Hogg, P. J., & Mutus, B. (2001). Mechanism of transfer of NO from extracellular S-nitrosothiols into the cytosol by cell-surface protein disulphide isomerase. *Proceedings of the National Academy of Sciences*, *98*(17), 9539-9544.

Rauch, F., Fahiminiya, S., Majewski, J., Carrot-Zhang, J., Boudko, S., Glorieux, F., ... & Moffatt, P. (2015). Cole Carpenter syndrome is caused by a heterozygous missense mutation in P4HB. *The American Journal of Human Genetics*, *96*(3), 425-431.

Rauch, J. N., & Gestwicki, J. E. (2014). Binding of human nucleotide exchange factors to heat shock protein 70 (HSP70) generates functionally distinct complexes in vitro. *Journal of Biological Chemistry*, *289*(3), 1402-1414.

Rho, J. Y., Zioupos, P., Currey, J. D., & Pharr, G. M. (1999). Variations in the individual thick lamellar properties within osteons by nanoindentation. *Bone*, *25*(3), 295-300.

Rousseau, F., Bonaventure, J., Legeai-Mallet, L., Pelet, A., Rozet, J. M., Maroteaux, P., ... & Munnich, A. (1994). Mutations in the gene encoding fibroblast growth factor receptor-3 in achondroplasia. *Nature*, *371*(6494), 252-254.

Rutkevich, L. A., Cohen-Doyle, M. F., Brockmeier, U., & Williams, D. B. (2010). Functional relationship between protein disulphide isomerase family members during the oxidative folding of human secretory proteins. *Molecular biology of the cell*, *21*(18), 3093-3105.

Samali, A., & Orrenius, S. (1998). Heat shock proteins: regulators of stress response and apoptosis. *Cell stress & chaperones*, *3*(4), 228.

Santos, G. B., Gonzalez-Perilli, L., Mastrogiovanni, M., Aicardo, A., Cerdeira, C. D., Sarafian, V., Jadot, M., Foidart, J. M., Letesson, J. J., Van den Brûle, F., Castronovo, V., ... & Wattiaux-De Coninck, S. (1998). Expression of Lamp-1 and Lamp-2 and their interactions with galectin-3 in human tumor cells. *International journal of cancer*, *75*(1), 105-111.

Sawin, K. E., LeGuellec, K., Philippe, M., & Mitchison, T. J. (1992). Mitotic spindle organization by a plus-end-directed microtubule motor. *Nature*, *359*(6395), 540-543.

Schwaller, M., Wilkinson, B., & Gilbert, H. F. (2003). Reduction-reoxidation cycles contribute to catalysis of disulphide isomerization by protein-disulphide isomerase. *Journal of Biological Chemistry*, *278*(9), 7154-7159.

Settembre, C., Cinque, L., Bartolomeo, R., Di Malta, C., De Leonibus, C., & Forrester, A. (2018). Defective collagen proteostasis and matrix formation in the pathogenesis of lysosomal storage disorders. *Matrix Biology*, *71*, 283-293.

Sharp, D. J., Rogers, G. C., & Scholey, J. M. (2000). Microtubule motors in mitosis. *Nature*, *407*(6800), 41-47.

Shi, S., Kirk, M., & Kahn, A. J. (1996). The role of type I collagen in the regulation of the osteoblast phenotype. *Journal of Bone and Mineral Research*, *11*(8), 1139-1145.

Shibata, Y., Voeltz, G. K., & Rapoport, T. A. (2006). Rough sheets and smooth tubules. *Cell*, *126*(3), 435-439.

Shoulders, M. D., & Raines, R. T. (2009). Collagen structure and stability. *Annual review of biochemistry*, *78*, 929-958.

Silver, F. H., Kato, Y. P., Ohno, M., & Wasserman, A. J. (1992). Analysis of mammalian connective tissue: relationship between hierarchical structures and mechanical properties. *Journal of long-term effects of medical implants*, *2*(2-3), 165-198.

Sims, N. A., & Vrahnas, C. (2014). Regulation of cortical and trabecular bone mass by communication between osteoblasts, osteocytes and osteoclasts. *Archives of biochemistry and biophysics*, *561*, 22-28.

Skoufias, D. A., & Wilson, L. (1992). Mechanism of inhibition of microtubule polymerization by colchicine: inhibitory potencies of unliganded colchicine and tubulin-colchicine complexes. *Biochemistry*, *31*(3), 738-746.

Smith, J. L., McBride, C. M., Nataraj, P. S., Bartos, D. C., January, C. T., & Delisle, B. P. (2011). Trafficking-deficient hERG K+ channels linked to long QT syndrome are regulated by a microtubule-dependent quality control compartment in the ER. *American Journal of Physiology-Cell Physiology*, *301*(1), C75-C85.

Soldà, T., Garbi, N., Hämmerling, G. J., & Molinari, M. (2006). Consequences of ERp57 deletion on oxidative folding of obligate and facultative clients of the calnexin cycle. *Journal of Biological Chemistry*, *281*(10), 6219-6226.

Solovyov, A., & Gilbert, H. F. (2004). Zinc-dependent dimerization of the folding catalyst, protein disulphide isomerase. *Protein science*, *13*(7), 1902-1907.

Solovyov, A., & Gilbert, H. F. (2004). Zinc-dependent dimerization of the folding catalyst, protein disulphide isomerase. *Protein science*, *13*(7), 1902-1907.

Steinmann, B., Royce, P. M., & Superti-Furga, A. (2002). The Ehlers-Danlos syndrome. *Connective tissue and its heritable disorders*, *2*, 431-523.

Stopfer, J., Hurt, H., Magilner, A., & Schneider, A. (1992). A variant type of osteogenesis imperfecta: confirmation of a rare phenotype. *Am J Hum Genet*, *51*, A108.

Tateya, T., Tateya, I., & Bless, D. M. (2006). Collagen subtypes in human vocal folds. *Annals of Otology, Rhinology & Laryngology*, *115*(6), 469-476.

Terasaki, M., Chen, L. B., & Fujiwara, K. (1986). Microtubules and the endoplasmic reticulum are highly interdependent structures. *The Journal of cell biology*, *103*(4), 1557-1568.

Timberlake, A. T., Furey, C. G., Choi, J., Nelson-Williams, C., Loring, E., Galm, A., ... & Lifton, R. P. (2017). De novo mutations in inhibitors of Wnt, BMP, and Ras/ERK signaling pathways in non-syndromic midline craniosynostosis. *Proceedings of the National Academy of Sciences*, *114*(35), E7341-E7347.

Todd, M. J., Lorimer, G. H., & Thirumalai, D. (1996). Chaperonin-facilitated protein folding: optimization of rate and yield by an iterative annealing mechanism. *Proceedings of the National Academy of Sciences*, *93*(9), 4030-4035.

Trostchansky, A., & Brigagão, M. R. P. L. (2017). Nitroxide 4-hydroxy-2, 2′, 6, 6′-tetramethylpiperidine 1-oxyl (Tempol) inhibits the reductase activity of protein disulphide isomerase via covalent binding to the Cys400 residue on CXXC redox motif at the a′ active site. *Chemico-biological interactions*, *272*, 117-124.

Tzaphlidou, Margaret. "Bone architecture: collagen structure and calcium/phosphorus maps." *Journal of biological physics* vol. 34,1-2 (2008): 39-49. doi:10.1007/s10867-008-9115-y

Uehara, T., Nakamura, T., Yao, D., Shi, Z. Q., Gu, Z., Ma, Y., ... & Lipton, S. A. (2006). S-nitrosylated protein-disulphide isomerase links protein misfolding to neurodegeneration. *Nature*, *441*(7092), 513.

Valenzuela, V., Jackson, K. L., Sardi, S. P., & Hetz, C. (2018). Gene therapy strategies to restore ER proteostasis in disease. *Molecular Therapy*, *26*(6), 1404-1413.

van Lith, M., Hartigan, N., Hatch, J., & Benham, A. M. (2005). PDILT, a divergent testis-specific protein disulphide isomerase with a non-classical SXXC motif that engages in disulphide-dependent interactions in the endoplasmic reticulum. *Journal of Biological Chemistry*, *280*(2), 1376-1383.

Viguet-Carrin, S., Garnero, P., & Delmas, P. D. (2006). The role of collagen in bone strength. *Osteoporosis international*, *17*(3), 319-336.

Vinaik, R., Kozlov, G., & Gehring, K. (2013). Structure of the non-catalytic domain of the protein disulphide isomerase-related protein (PDIR) reveals function in protein binding. *PLoS One*, *8*(4), e62021.

Wang, S., Tukachinsky, H., Romano, F. B., & Rapoport, T. A. (2016). Cooperation of the ER-shaping proteins atlastin, lunapark, and reticulons to generate a tubular membrane network. *Elife*, *5*, e18605.

Wass, M. N., Kelley, L. A., & Sternberg, M. J. (2010). 3DLigandSite: predicting ligand-binding sites using similar structures. *Nucleic acids research*, *38*(suppl_2), W469-W473.

Watanabe, S., Amagai, Y., Sannino, S., Tempio, T., Anelli, T., Harayama, M., ... & Inaba, K. (2019). Zinc regulates ERp44-dependent protein quality control in the early secretory pathway. *Nature communications*, *10*(1), 1-16.

Waterman-Storer, C. M., & Salmon, E. D. (1998). Endoplasmic reticulum membrane tubules are distributed by microtubules in living cells using three distinct mechanisms. *Current Biology*, *8*(14), 798-807.

Webb, J. L., Ravikumar, B., & Rubinsztein, D. C. (2004). Microtubule disruption inhibits autophagosome-lysosome fusion: implications for studying the roles of aggresomes in polyglutamine diseases. *The international journal of biochemistry & cell biology*, *36*(12), 2541-2550.

Weiner, S., & Wagner, H. D. (1998). The material bone: structure-mechanical function relations. *Annual review of materials science*, *28*(1), 271-298.

Weiner, S., Traub, W., & Wagner, H. D. (1999). Lamellar bone: structure–function relations. *Journal of structural biology*, *126*(3), 241-255.

Wilkinson, B., & Gilbert, H. F. (2004). Protein disulphide isomerase. *Biochimica et Biophysica Acta (BBA)-Proteins and Proteomics*, *1699*(1-2), 35-44.

Wilson, R., Lees, J. F., & Bulleid, N. J. (1998). Protein disulphide isomerase acts as a molecular chaperone during the assembly of procollagen. *Journal of Biological Chemistry*, *273*(16), 9637-9643.

Winklhofer, K. F., Tatzelt, J., & Haass, C. (2008). The two faces of protein misfolding: gain- and loss-of-function in neurodegenerative syndromes. *The EMBO journal*, *27*(2), 336-349.

Wlodkowic, D., Skommer, J., & Darzynkiewicz, Z. (2009). Flow cytometry-based apoptosis detection. In *Apoptosis* (pp. 19-32). Humana Press, Totowa, NJ.

Xiong, B., Jha, V., Min, J. K., & Cho, J. (2020). Protein disulphide isomerase in cardiovascular disease. *Experimental & molecular medicine*, *52*(3), 390-399.

Xiong, G., Stewart, R. L., Chen, J., Gao, T., Scott, T. L., Samayoa, L. M., ... & Xu, R. (2018). Collagen prolyl 4-hydroxylase 1 is essential for HIF-1α stabilization and TNBC chemoresistance. *Nature communications*, *9*(1), 1-16.

Xu, S., Butkevich, A. N., Yamada, R., Zhou, Y., Debnath, B., Duncan, R., ... & Neamati, N. (2012). Discovery of an orally active small-molecule irreversible inhibitor of protein disulphide isomerase for ovarian cancer treatment. *Proceedings of the National Academy of Sciences*, *109*(40), 16348-16353.

Xu, S., Sankar, S., & Neamati, N. (2014). Protein disulphide isomerase: a promising target for cancer therapy. *Drug discovery today*, *19*(3), 222-240.

Yam, G. H. F., Zuber, C., & Roth, J. (2005). A synthetic chaperone corrects the trafficking defect and disease phenotype in a protein misfolding disorder. *The FASEB Journal*, *19*(1), 12-18.

Yates, C. M., Filippis, I., Kelley, L. A., & Sternberg, M. J. (2014). Suspect: enhanced prediction of single amino acid variant (SAV) phenotype using network features. *Journal of molecular biology*, *426*(14), 2692-2701.

Yordanov, T. E., Hipolito, V. E., Liebscher, G., Vogel, G. F., Stasyk, T., Herrmann, C., ... & Huber, L. A. (2019). Biogenesis of lysosome-related vesicles complex-1 (BORC) regulates

late endosomal/lysosomal size through PIKfyve-dependent phosphatidylinositol-3, 5-bisphosphate. *Traffic*, *20*(9), 674-696.

Zhang, M., Xuan, S., Bouxsein, M. L., Von Stechow, D., Akeno, N., Faugere, M. C., ... & Clemens, T. L. (2002). Osteoblast-specific knockout of the insulin-like growth factor (IGF) receptor gene reveals an essential role of IGF signaling in bone matrix mineralization. *Journal of Biological Chemistry*, *277*(46), 44005-44012.

Zhang, Y., Baig, E., & Williams, D. B. (2006). Functions of ERp57 in the folding and assembly of major histocompatibility complex class I molecules. *Journal of Biological Chemistry*, *281*(21), 14622-14631.

Zhao, D., Yang, J., Han, K., Liu, Q., Wang, H., Liu, Y., ... & Li, Y. (2019). The unfolded protein response induced by Tembusu virus infection. *BMC veterinary research*, *15*(1), 1-13.

Zhao, G., Lu, H., & Li, C. (2015). Proapoptotic activities of protein disulphide isomerase (PDI) and PDIA3 protein, a role of the Bcl-2 protein Bak. *Journal of Biological Chemistry*, *290*(14), 8949-8963.

Zhao, Y. G., & Zhang, H. (2019). Autophagosome maturation: an epic journey from the ER to lysosomes. *Journal of Cell Biology*, *218*(3), 757-770.

Zheng, P., Chen, Q., Tian, X., Qian, N., Chai, P., Liu, B., ... & Chen, J. (2018). DNA damage triggers tubular endoplasmic reticulum extension to promote apoptosis by facilitating ER-mitochondria signaling. *Cell research*, *28*(8), 833-854.